UNIVERSITÉ DU LUXEMBOURG

PhD-FSTM-2020-081
The Faculty of Sciences, Technology and Medicine

DISSERTATION

Defence held on 15/12/2020 in Luxembourg

to obtain the degree of

DOCTEUR DE L'UNIVERSITÉ DU LUXEMBOURG

EN PHYSIQUE

by

Meenu MURALI

Born on 28 May 1991 in Mavelikara, Kerala (India)

PRESSURE SENSING WITH NEMATIC LIQUID CRYSTAL AND CARBON NANOTUBE NETWORKS

Dissertation defence committee

Dr. Giusy SCALIA, dissertation supervisor
ADR, Université du Luxembourg

Dr. Tanja SCHILLING
Professor, Universität Freiburg

Dr. Susanne SIEBENTRITT, Chair
Professor, Université du Luxembourg

Dr. Philippe POULIN
CNRS Research Director DR1, Université de Bordeaux

Dr. Emmanuel DEFAŸ, Vice-Chair
Group Leader, Luxembourg Institute of Science and Technology

Pressure Sensing with Nematic Liquid Crystal and Carbon Nanotube Networks

Meenu Murali

A dissertation submitted in partial fulfilment of the requirements

for the degree of

Doctor of Philosophy in Physics

University of Luxembourg

Faculty of Science, Technology and Medicine

December 2020

I dedicate this thesis to

my parents, Usha and Murali, my sister, Neethu, and my husband, Praveen

for their unconditional love and endless support.

Abstract

The study of colloidal dispersions of nanoparticles in liquid crystals (LCs) is well known. In most of the works, the particles are mixed into the LC to form suspensions with well-dispersed particles. However, when nanoparticles are physically connected to form networks, the overall macroscopic properties of the ensemble are directly linked to the specific properties of the nanoparticles. Carbon nanotubes (CNTs) are excellent electrical conductors possessing extremely high aspect ratio, which results in a very low concentration threshold needed to obtain percolation. Therefore, they form conductive networks with extremely small amounts of CNTs. Another advantage of carbon nanotubes is their capability to transport large current densities without damage by electromigration, maintaining a stable resistance, and having scattering-less paths across several microns. Moreover, the electromechanical properties of CNTs make them an ideal candidate in pressure sensing technology.

The doctoral thesis presented here describes two different approaches to integrate and utilise CNTs in an LC matrix. In the first case, we show that a variety of nanoparticles that are dispersed in LC can be attracted and assembled onto a LC defect line generated in a predetermined location, thereby creating a vertical interconnect of nanoparticles. The second consists of CNT sheets mechanically drawn from a CNT forest and an LC cell is then built on top, and the second consists of a template-based assembly of dispersed CNTs onto defect lines in LCs. In this case, we study the electrical and optical properties of CNT sheets in the presence and absence of liquid crystals based on their DC electrical characterization with distributed electrical contacts. Finally, we discuss how these two approaches can be used to successfully fabricate pressure-sensing devices.

The pressure response in both these sensors is achieved based on the change in resistance of the CNTs, induced by the structural variations under the external applied pressure. Both the pressure sensors developed here are easy to fabricate, cost-effective, and recoverable owing to the elasticity and softness of the LC.

Table of Contents

List of Figures

List of Tables

Chapter 1

Introduction

There is always a growing need to develop new sensors with improved sensing capabilities. Innovative pressure sensors are especially relevant in the realm of touch interfaces [1], healthcare monitoring devices [2][3], and wearable devices such as artificial [4] and electronic [5] skin and flexible displays [6][7]. To be able to use them as touch sensors in displays, it is necessary that these sensors are not only pressure responsive but also transparent, flexible, and thin. In general, pressure sensors can be inductive, capacitive, or resistive depending on how the pressure is monitored. In this thesis, I present two different configurations of resistive pressure sensors based on a combination of carbon nanotubes and liquid crystals.

Carbon nanotubes (CNTs) in combination with liquid crystals (LCs) are an interesting assemblage of anisotropic hard and soft matter. This shape anisotropy of both the CNTs and LC molecules makes them compatible with each other and allows LCs to easily incorporate CNTs into their own configuration. Consequently, LCs can easily disperse and influence the ordering in the dispersed CNTs. Well-aligned macroscopic CNT ensembles can similarly impart their orientational ordering to the LC in which they are embedded.

LCs, owing to their high responsiveness to external stimuli, are conducive to applications in the sensing field. The fluidity of the LC at mesoscopic scales enables the prospect of easily creating large, ordered structures. The softness and elasticity at macroscopic scales further facilitates their role as embedding matrices in recoverable devices. Furthermore, the ability to manipulate their molecular alignment and symmetry could potentially be used to tailor unique properties.

Thanks to their unique electrical [8][9], mechanical [10][11], and electromechanical [12] properties, carbon nanotubes have garnered considerable scientific interest in the field of pressure sensing devices. Commercialization of devices based on these is challenging owing to the difficulty in spatially controlling the individual tubes as well as the inconsistency in electrical properties, which is subject to variations in their diameter and chirality. Hence, devices based on macroscopic CNT assemblies offer a practical route to large-scale applications due to their ease of fabrication and the averaging of the electrical properties.

In nanotechnology, however, one of the main obstacles is to develop macro- or microscopic devices by integrating nanomaterials whilst maintaining their exceptional individual characteristics. After Jiang et al. first demonstrated the spinning of CNT yarns [13], multi-walled carbon nanotube (MWCNT) sheets have attracted much research interest as continuous sheets can be mechanically drawn from spinnable MWCNT arrays through van der Waals forces between the nanotubes [14]. The main idea behind the fabrication of CNTs into yarns, sheets, or composites with other materials is to employ the remarkable properties of carbon nanotubes at a macroscopic scale. Because of their high alignment, transparency, and conductivity, CNT sheets are an attractive candidate for use in heaters [15][16], sensors [17][18], and energy devices [19]. These sheets are suitable for both lightweight structural and functional applications [20]. However, even with the successful development of aligned carbon nanotubes with exceptional mechanical and physical properties, studies on aligned CNT-based devices are currently in their preliminary phases of development.

In this thesis, we mainly explore pressure sensors based on two different LC-CNT configurations. The first is a vertical configuration, referred to as Sensor 1, where tailor-made LC defect lines act as a template to fabricate the vertical interconnect of MWCNTs, which is the pressure-sensing element. The second is a horizontal configuration, referred to as Sensor 2, where well-aligned MWCNT sheets embedded in a LC medium are the pressure-sensing element.

The exceptional properties of CNTs, such as their mechanical strength [21], ballistic transport [22] of electrons with mean-free paths of several microns [23], high thermal

conductivity [24] and large ampacity of up to 10^9 A/cm^2 [25] resulting from the sp^2 hybridization of C–C bonds, make them one of the most promising alternatives to conventional interconnect materials in nano- and microelectronics. Vertically grown carbon nanotubes have the limitation of requiring complex fabrication techniques in addition to the inability to control the CNT quality, density, and type. A promising direction in this field is the innovative technique proposed by Fleury et al. [26] for surface tailoring LC alignment to impose boundary conditions to direct the formation of a defect line, which in turn can guide the self-assembly of particles via nematic interactions. We used similar surface patterning to create the discrete boundary conditions to generate the defect line that acts as a template for our vertical interconnect of multi-walled carbon nanotubes in Sensor 1. The softness of the LC matrix enables reversible deformations of the continuous CNT network, thereby disrupting the electrical conduction when applying pressure.

Carbon nanotubes, owing to their one-dimensional nanostructure, has been proposed as an effective aligning layer and as transparent conductive electrodes for liquid crystal displays (LCDs) [27][28]. Research aimed at using highly aligned CNT sheets as a multifunctional component in flexible liquid crystal display applications has been undertaken to further develop this technology [29]. This motivated us to explore the possibilities of expanding the scope of this system for use as pressure sensors. These sensors could have future prospects for touch sensors in flexible displays. This led to the development of Sensor 2.

1.1 Overview of the structure of the thesis

The remainder of the thesis is structured as follows:

Chapter 2: Background

This chapter reviews the relevant concepts and properties of LCs and CNTs underlying the work in this thesis. Furthermore, in this chapter, an overview of the existing pressure sensors based on CNTs is also discussed.

Chapter 3: Interactions of nano-diameter rod and tubular particles with a defect line in a nematic liquid crystal

In Chapter 3, we introduce the different distortions that can arise owing to the presence of dispersed particles in liquid crystals. We discuss the fabrication technique of surface tailoring applied to host the defect lines in a nematic LC and evaluate its interactions with two homotopically different cylindrical nanoparticles. We use $Mo_6S_2I_8$ nanowires as rod-shaped nanoparticles and single-walled carbon nanotubes and multi-walled carbon nanotubes as tube-shaped nanoparticles. Our studies indicated non-trapping of single-walled carbon nanotubes and comparatively faster trapping of $Mo_6S_2I_8$ nanowires than multi-walled carbon nanotubes onto the LC defect lines.

Chapter 4: Characterization of aligned carbon nanotube sheets in nematic liquid crystals

Chapter 4 elaborates the different steps in fabricating LC cells with CNT sheets drawn from CNT forests. With an aim of subsequently implementing this system in pressure sensing, we carried out the relevant electrical and optical characterization and study the influence of an LC on the CNT sheets. We also monitor the degree of orientational order of carbon nanotubes, via absorption spectroscopy, when they are introduced in liquid crystals.

Chapter 5: Pressure sensing using liquid crystals with carbon nanotubes

Chapter 5 is divided into two main parts, with each part elaborating the fabrication techniques and pressure response measurements of the two aforementioned LC-CNT pressure sensors, the main outcome of this thesis: Sensor 1, which is a vertical interconnect of multi-walled carbon nanotubes in an LC, and Sensor 2, a horizontal configuration of well-aligned multi-walled carbon nanotube sheets embedded in an LC.

Chapter 6: Conclusions and Outlook

Chapter 6 provides a summary of the main results of this work and an outlook towards the future research that could follow.

Chapter 2

Background

Overview of the chapter

This chapter outlines the key concepts involving liquid crystals and carbon nanotubes that lay the foundation for understanding the thesis. This includes the basic introduction to liquid crystals and carbon nanotubes, and the related theoretical concepts.

2.1 Liquid crystals

Liquid crystals (LC) are materials that form phases, known as mesophases or liquid crystalline phases, which are an intermediate state of matter between isotropic liquids and crystalline solids [30]. These phases correspond to a partially ordered liquid in the sense that they can flow like a liquid and yet exhibit anisotropic physical properties, which are impossible in isotropic liquids. LC molecules, also known as mesogens, have ordering properties similar to those of crystalline solids. Some of these phases possess only orientational order, while some possess both orientational as well as positional order [31]. The long-range orientational ordering in liquid crystals is attributed to the highly anisotropic shape of the mesogens, while the thermal motion of the mesogens is accountable for its fluidity.

Liquid crystals were first discovered in 1888 by an Austrian chemist and botanist Friedrich Reinitzer [32], who noticed that an organic material, cholesteryl benzoate, displayed two distinct melting points. At first, the solid melted into a turbid fluid that, at a higher temperature, further melted to a clear isotropic liquid. Although the primary use of liquid crystals currently is in display (LCD) technologies [33][34], the earliest examples of liquid crystal applications were thermometers that used the temperature dependence of the helical pitch of cholesteric LCs [35]. Liquid crystals have also recently been explored as an ideal candidate for sensing applications because of their high responsiveness achieved through harnessing characteristics such as molecular orientation and optical anisotropy [36][37][38][39].

2.1.1 Classes of liquid crystals

Liquid crystals are typically classified as thermotropic or lyotropic liquid crystals. Thermotropic LCs are pure compounds or homogeneous mixtures which form one or more mesophases depending on temperature. Upon heating the material, a mesophase appears at a temperature above the ‘melting point’ (crystalline solid-LC transition temperature) and, upon further heating to above the 'clearing point' (LC-isotropic liquid transition temperature), the material exists as an isotropic liquid. The phase transitions are typically

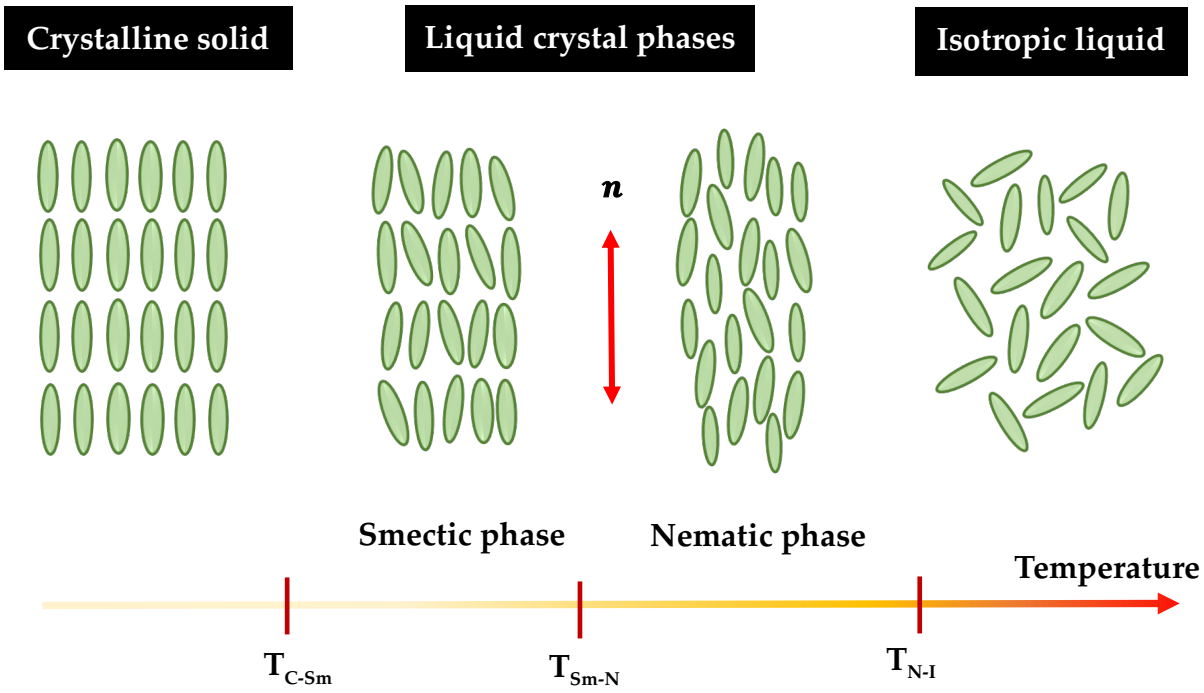

Figure 1: Schematic illustration of the molecular arrangements with temperature changes (increasing from left to right) for thermotropic LCs consisting of rod-shaped mesogens (represented as ellipsoids). Within the LC temperature range, nematic (N) and smectic (Sm) phases can exist. ***n*** denotes the local director field.

repeated in the reverse sequence when the isotropic liquid is cooled down; such mesophases are thermodynamically stable and are called enantiotropic. LC phases that are thermodynamically unstable and appear only upon cooling are called monotropic. Lyotropic LCs, on the other hand, are formed when amphiphilic molecules are dissolved in appropriate concentrations of a suitable solvent. Thus, the stability of the mesogens is concentration-driven and the relative concentration of the solution determines their liquid crystalline properties.

2.1.2 Liquid crystalline phases

Similar to crystalline solids, liquid crystals demonstrate anisotropic properties that are closely related to the shape anisotropy of their constituent molecules [40]. Their molecular structure is such that not all molecular axes are equivalent. Thermotropic LCs are generally

composed of highly anisometric organic molecules that are of moderate size (~2–5 nm) [30]. While it is established in most cases that rod-shaped (also called calamitic) [30] molecules can potentially form liquid crystalline phases, other molecular compounds that are disc-shaped (discotic) [41] or banana-shaped (bow-like or bent-core) [42][43] can also form mesophases. According to the classification of the liquid crystal mesophases proposed in 1922 by Georges Friedel [44] based on the molecular arrangement, thermotropic LCs can be categorized into nematic, smectic and cholesteric phases.

At low temperatures, a typical liquid crystal forms a crystalline solid state that possess both orientational and positional order, in which the mesogens are forced to occupy specific lattice sites and at the same time align their molecular axes in a fixed direction. At high enough temperatures, the material is in the isotropic liquid phase, where the mesogens will be arbitrarily oriented with no long-range orientational or positional order. A common representation of the anisotropic shape of liquid crystal molecules is as ellipsoids, as depicted in Figure 1. Owing to their elongated shape, the molecules will exhibit only orientational order under suitable conditions so that the molecular axes align in a preferred direction to form the nematic phase (derived from the Greek *νήμα* / *néma*, meaning thread, referring to the thread-like defect lines seen with polarizing optical microscopy) [30]. The mesogens are still capable of moving around, but their overall orientation is retained. The average orientation of the mesogens is called the director, $\boldsymbol{n}$. In addition to orientational order, positional order can also occur based on the type and shape of the mesogens and the temperature conditions they encounter. Such phases are called smectic phases (derived from the Latin *smecticus,* soap, as their structure is similar to those in soap films). The orientation is well defined in smectics, and the fluidity is limited to within the layers. Cholesteric or chiral nematic phases, like the nematic phase, possess a long-range orientational order and no positional order, the difference being the periodic twisting of the director throughout the material, as the mesogens tend to orient in a helical manner.

Illustrated in Figure 2 is the molecular structure of the liquid crystal 4-cyano-4'-pentylbiphenyl, first synthesized by George Gray [45] and commonly known as 5CB, which is the most extensively studied thermotropic liquid crystal and the one used in this research.

It is about ~2 nm in length and a room temperature (between 24˚C – 35.5˚C) nematic LC and has a central core attached to a more flexible hydrocarbon chain with two aromatic rings, that are relatively rigid.

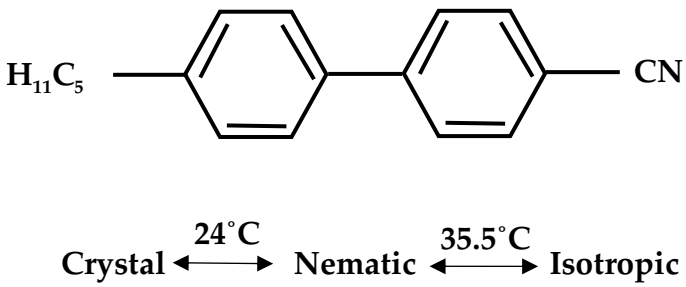

Figure 2: Molecular structure of 5CB liquid crystal

2.1.3 Orientational order parameter

As already seen in Figure 1, the molecules of a nematic LC, because of their anisometric shape, have a long-range orientational order and no positional order. There exists an average direction along which the mesogens tend to align, called the director, $\boldsymbol{n}$ [46], which is a unit pseudovector. Since nematic liquid crystals are uniaxial, (i.e., having rotational symmetry around a longer preferred axis called the principal axis), their properties are same in the $+\boldsymbol{n}$ and $-\boldsymbol{n}$ directions. For rod-shaped LCs, the director is along the long molecular axis, whereas for disc-shaped LCs, the director is along the short axis.

Another parameter that defines how well the LC mesogens are aligned with the director is the nematic orientational order parameter, S, defined based on the average of the second Legendre polynomial [31], given as

$$S = \frac{1}{2}\langle\, 3\cos^2\theta - 1 \,\rangle \tag{1}$$

where θ is the angle between the mesogen long axis and the local director. For isotropic liquids, $S = 0$, which implies a random orientation and for crystalline solids, $S = 1$, which implies that all molecules are perfectly aligned along $\boldsymbol{n}$. Liquid crystals typically have values

$0.3 < S < 0.7$ [46] and S decreases when the temperature is increased [40]. A nematic LC has the centres of the mass of the molecules randomly distributed throughout the material, as shown in Figure 3.

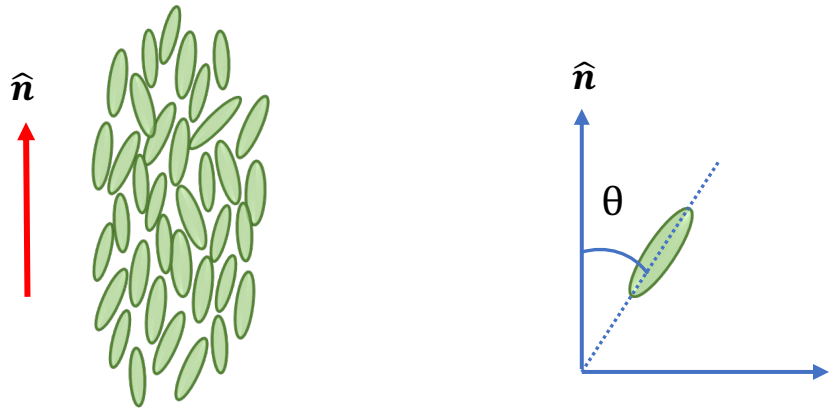

Figure 3: Orientation of nematic LC molecules along the director vector n. The angle θ describes the angle between the molecule and the average orientation.

2.1.4 Alignment of liquid crystals

As nematic liquid crystals are anisotropic, any analysis of their physical properties or electro-optic applications demands unidirectional macroscopic alignment of the director. The orientation of liquid crystals can be manipulated by surface treatments, electrical, or mechanical forces. Macroscopic orientation in a bulk sample can be obtained by simple surface treatments. In nematic LCs, the most commonly used types of alignment are the planar and homeotropic alignments, as illustrated in Figure 4.

In homeotropic alignment, the mesogens are oriented such that the director is perpendicular to the substrates, whereas, for planar alignment, the mesogens and the director consequently align parallel to the substrate surface. Homeotropic alignment can be achieved by coating the substrates with an amphiphilic material, such as surfactants or silanes. Such surfactants are generally soaps, whose polar head group binds to the substrate and the non-polar tail group extends into the liquid crystal material, thereby aligning the mesogens orthogonally to the surface of the substrate. Planar alignment can be obtained in numerous

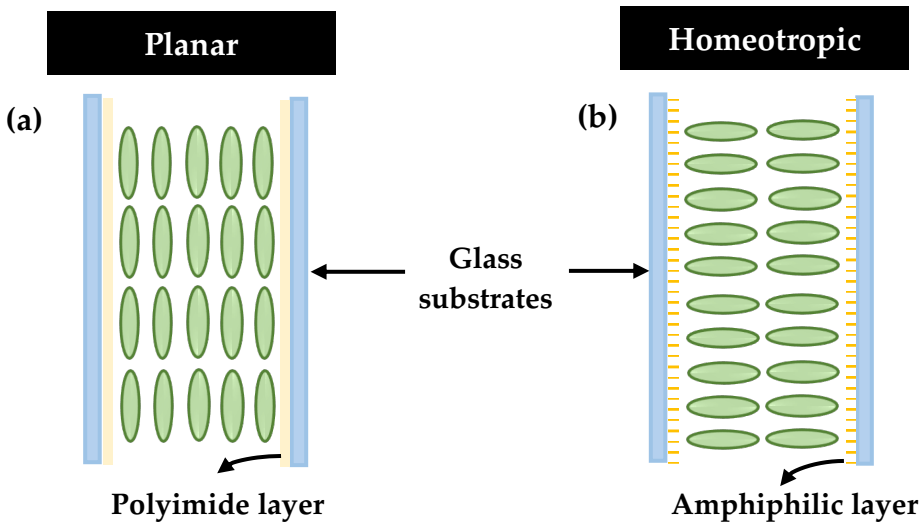

Figure 4: Alignment in nematic liquid crystal cells: (a) Planar alignment (b) Homeotropic alignment

ways. A common technique is to coat the substrates with a polymer, such as polyvinyl alcohol (PVA) or polyimide, and then rub it unidirectionally using a velvet cloth. This generates elongated stress on the polymer, creating microscopic grooves and, consequently promoting the alignment of the long axis of the mesogens along the rubbed path [47].

In our experiments, we are only interested in planar alignment, which is achieved through unidirectional rubbing of polytetrafluoroethylene (PTFE or Teflon) on glass substrates. This technique is relatively straightforward and easy as it simultaneously deposits the polymer and creates the microgrooves for the LC alignment.

2.1.5 Elasticity of liquid crystals

When liquid crystals are exposed to any surface, depending on the surface boundary conditions, the director will orient in a specific direction. In the absence of any boundary conditions, the orientation is degenerate and accordingly, the mesogens have no preferred orientation [30]. Anchoring may be defined as how the orientation of the director of a bulk liquid crystal is dictated by its confining substrates [48]. The equilibrium or unperturbed elastic ground state of a non-chiral nematic has a uniform director field, i.e., $\boldsymbol{n}$ points in a

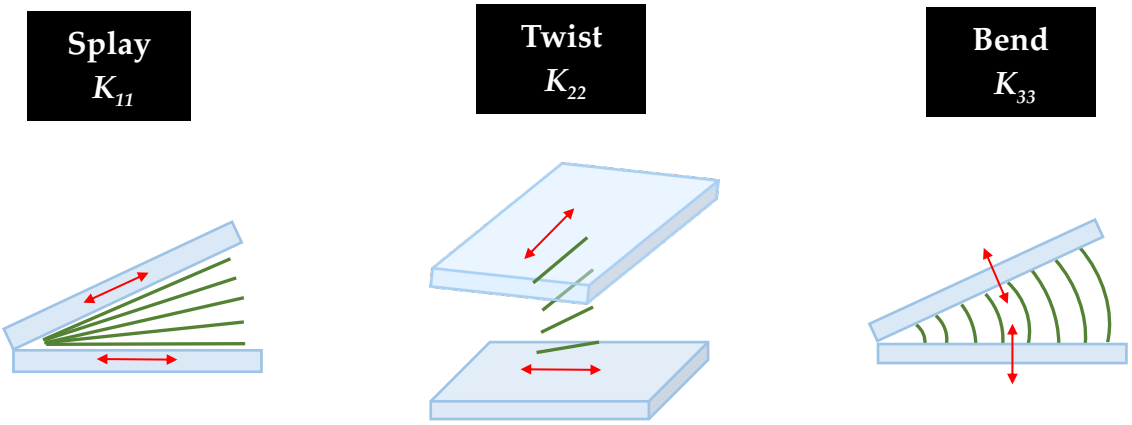

Figure 5: Schematic of the elastic deformations of the nematic LC: splay, twist, and bend. The green lines represent the director deformation, and the red arrows indicate the preferred director orientation.

similar direction throughout the sample. Generally, the surface of a substrate imposes a preferred orientation on the director, called the 'anchoring direction' or 'easy axis'. This is the minimal free energy alignment direction of liquid crystals on a substrate. The easy axis, in the absence of any external force or field, becomes the direction of spontaneous orientation of director at the surface.

Owing to their relatively low viscosity, even small external forces can easily deform nematic liquid crystals. This results in a local reorientation of the director, creating an elastic deformation that further extends the director field distortion to the bulk of the LC due to the long-range ordering. This distortion of the director costs (elastic) energy and the nematic LC attempts to restore the uniform director field through an elastic torque, the strength of which can be derived by differentiating the elastic free energy [49]. There are three fundamental kinds of elastic deformations in nematic liquid crystals: splay, twist, and bend, as depicted in Figure 5. The total elastic free energy contribution due to these deformations can be defined by the Frank – Oseen equation for the free energy density, given as [50][51],

$$\boldsymbol{F_d} = \frac{1}{2} K_{11} (\nabla \cdot \boldsymbol{n})^2 + \frac{1}{2} K_{22} (\boldsymbol{n} \cdot (\nabla \times \boldsymbol{n}))^2 + \frac{1}{2} K_{33} (\boldsymbol{n} \times (\nabla \times \boldsymbol{n}))^2 \quad (2)$$

where K_{11} , K_{22} , and K_{33} are the elastic constants corresponding to splay, twist and bend respectively and describe how 'stiff' the liquid crystal is to the deformations [40]. Their

values are often small, typically on the order of pN, with K_{11} and K_{22} having similar values and K_{33} being twice that value, for the case of 5CB. Furthermore, often these values are approximated into a single elastic constant value, by assuming a 'one-constant approximation': $K_{11} = K_{22} = K_{33} = K$.

2.1.6 Topological defects

Topological defects [52] occur in liquid crystals as a consequence of broken continuous symmetry [53][54]. They can exist as points, lines or walls in the three-dimensional space where there is no average molecular orientation and, hence, where the director $\boldsymbol{n}$ is undefined [54]. Line defects in nematics are also known as disclinations [55]. Distortions that generate defects can be easily created by manipulating the boundary conditions, surface geometry and external fields, and the subsequent defects can be optically imaged using a polarizing optical microscope [56]. When observed between crossed polarizers, we observe Schlieren textures (from German *Schliere*; meaning streak) where regions in which the director is parallel to either polarizer appear dark due to optical extinction. The LC mesogens are randomly oriented at the defect cores as in an isotropic disordered liquid. The central

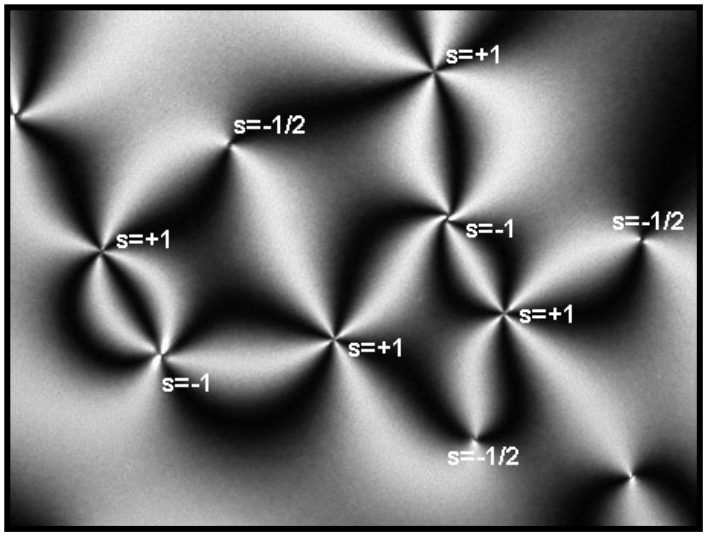

Figure 6: Schlieren texture in a nematic LC observed between crossed polarizers. The four black brushes are associated with the ±1 point defects and the two black brushes with the ±½ line defects. Adapted from [179].

region, or defect cores, thus appears black as the order parameter of the LC within the core is zero.

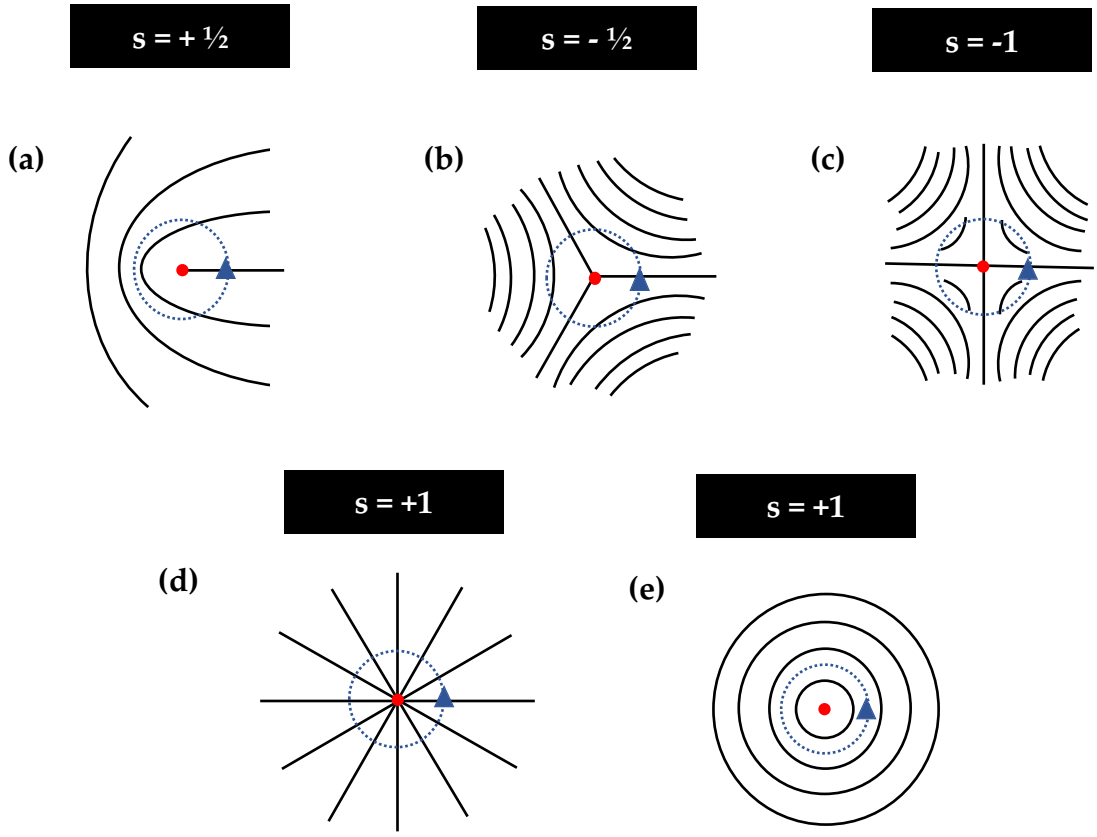

Figure 7: Schematic illustration of the director fields near some of the topological defects that can form in a liquid crystal. The red dot represents the core of the defect and the black lines represent the director field. The parameter s indicates the strength of the topological defect.

Defects are identified by their topological strength *s*, also known as winding number or topological charge, which is the number of multiples of 2π that the director rotates in a complete circuit around the defect core [31]. Figure 7 represents the structure of the director field configurations corresponding to the defects shown in Figure 6. In this thesis, we are mainly interested in the controlled generation of line defects of strength +½, i.e., the ones around which the director rotates by π.

2.1.6.1 Disclinations or defect lines

Nematic line defects were first referred to as 'disinclination' (now disclination) by Frank [50] to indicate discontinuities in the 'inclination' of the LC molecules. Figure 7(a) and (b) represent the director field structure around two commonly observed line defects in a nematic LC. The defect line, indicated by the red spot, is normal to the plane. Here, the director is restricted to the planes normal to the defect line. Such disclinations are called wedge disclinations [50]. There also exists another kind of disclination, known as twist disclinations [57], where the director is restricted to the planes parallel to the defect line [58].

In this thesis, we study wedge disclination lines of strength +½ that are generated in predesigned locations by realizing conflicting orientations on the surfaces that are in contact with the liquid crystal. The director configuration is defined by the anchoring of the LC molecules on the surface of the substrate. This is achieved by smearing the substrates with a polytetrafluoroethylene (PTFE, or Teflon) bar at 200°C in three different rubbing directions to form a defect at a point *P*, as indicated in Figure 8. The substrates will have conflicting planar anchoring on its surface at the intersection of the three rubbing regions, so the LC molecules will not be able to align themselves in any particular direction, resulting

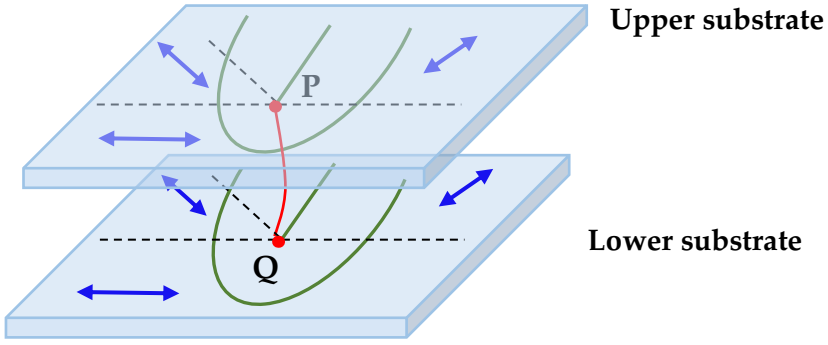

Figure 8: Schematic of the disclination (red line) joining two designated locations and the nematic distortion (green lines) created. The blue arrows indicate the rubbing directions of the Teflon bar on the substrates and the points P and Q represent the point defects (red dots).

in a point defect at *P*. Two substrates with similar surface treatments are placed face-to-face with appropriate spacing such that the PTFE rubbings face each other, and nematic LC is filled in through capillary filling. A defect line of strength +½ is created that extends from the upper to the lower substrate. The core of the disclination (~10 nm diameter [59]) is a fine thread running through the LC material. When observed under a polarizing optical microscope, defects appear as black spots or dark lines limiting the cylindrical core (as in our study), as light is scattered away from the defect boundaries.

While topological defects are undesirable for certain purposes (such as malfunctioning pixels in LC displays that slow down LC switching), they have recently been exploited favourably in LCs, especially by regulating the interactions between the defects and dispersed particles [26][60][61][62]. Particles dispersed in a nematic LC create orientational distortions that interfere with the distortion created by the defect line, resulting in a translational force that drags them towards the defect line. One of the configurations of the pressure sensor that we developed using a vertical interconnect of carbon nanotubes trapped onto a disclination line was inspired by the work of Fleury et al. [26]. Disclinations can attract the dispersed carbon nanotubes in the LC. This attraction is energetically favoured, and results in a vertical interconnect of carbon nanotubes. The details of this will be explained in later chapters.

2.1.7 Optical anisotropy of liquid crystals

Nematic liquid crystals, owing to their optical anisotropy (i.e., properties depend on the direction of light propagation and light polarization), can act as a uniaxial birefringent material with the director defining the optical axis. Light propagating along the optical axis is not refracted while rays along any other directions with polarization at an angle with the optic axis display double refraction or in other words, experience two different refractive indices in directions perpendicular to each other. In a uniaxial nematic LC, $n_{||}$ is the refractive index experienced for light polarized parallel to the director and $n_{\perp}$ for light polarized perpendicular to it. Therefore, light incident at any other angle with a generic polarization direction splits into ordinary and extraordinary wave components traveling with different

velocities; as a result, the phase of the wave is shifted. This leads to a change in the polarization state as the rays recombine while exiting the birefringent LC. This optical phenomenon can be easily observed using a polarizing optical microscope and is referred to as birefringence. Birefringence is quantified by the difference Δn between the indices of refraction of the ordinary (n_o) and extraordinary (n_e) waves [40] $\Delta n = n_o - n_e$. For typical nematic LCs, Δn varies in the range of 0.05 to 0.5 [56].

2.1.7.1 Polarizing optical microscopy

Polarizing optical microscopy (POM) works on the principle of polarization of light, as illustrated in Figure 9, for an unpolarised beam of light incident on two polarizers oriented at an angle 90˚ with each other. When unpolarised light is incident on polarizer 1, the vertical component of the electric field vector of the incident light passes through polarizer 1 (as the polarizing direction here is vertical) and the light beam becomes vertically polarized. This beam, when incident on the polarizer 2, is blocked as it has a horizontal polarizing direction. This orientation of the polarizers is commonly referred as 'crossed polarizers'.

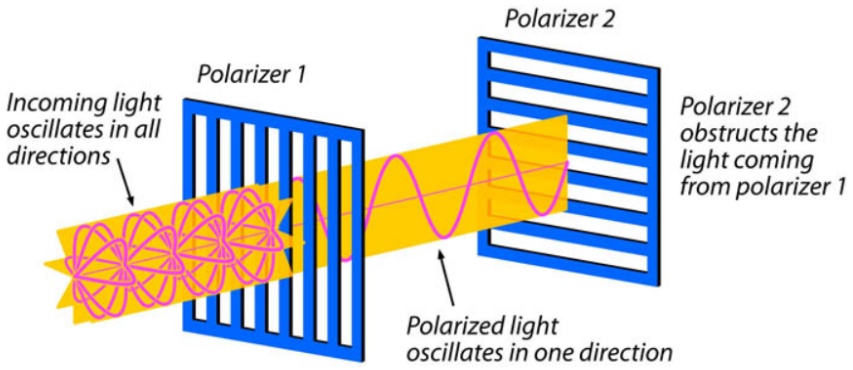

Figure 9: Schematic representation of the concept of polarization of light. Adopted from [180].

POM uses the birefringence of nematic LCs for optical imaging. The principle of POM is as shown in Figure 10(a). We used a Nikon Eclipse LV100ND polarising optical microscope, consisting of different components as illustrated in Figure 10(b), mounted with a digital

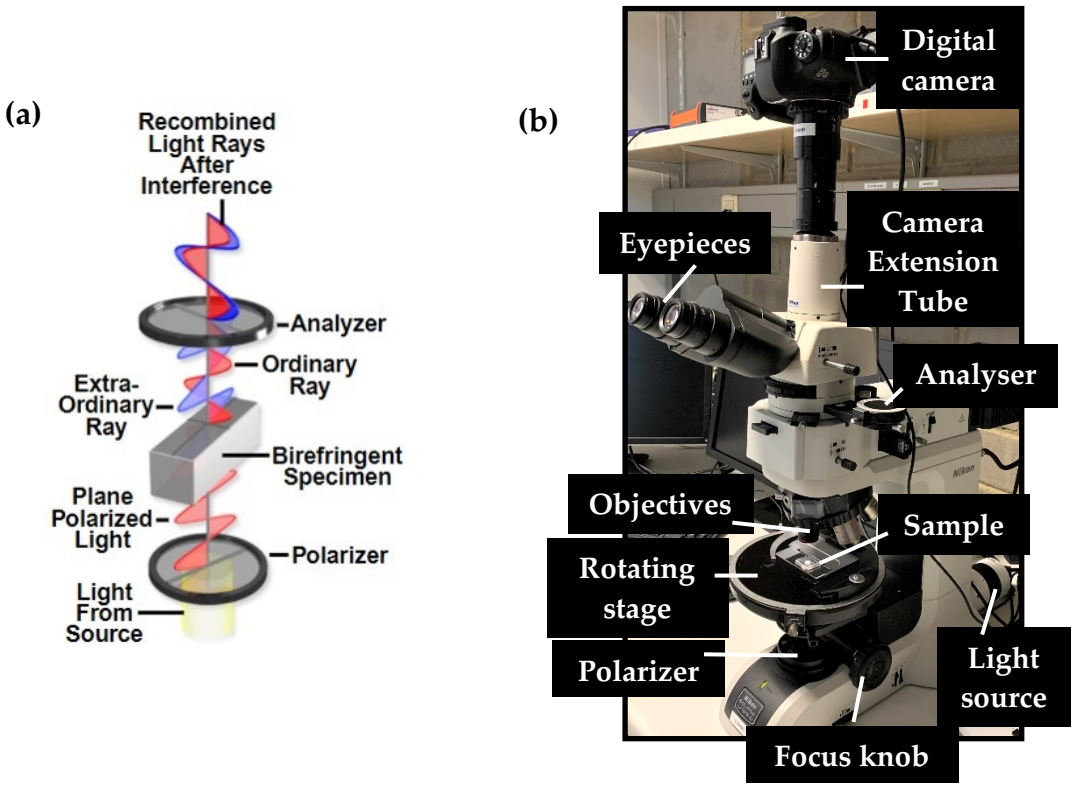

Figure 10: (a) The interaction of light with birefringent LC placed under crossed polarizers. Adopted from [181]. (b) The polarizing optical microscope Nikon Eclipse LV100ND used in our experiments.

camera (Canon EOS 6D) to optically characterize our samples. The type of the liquid crystal and the different LC mesophases can be easily identified from their characteristic POM textures. The sample was placed on a rotatable stage between two crossed linear polarizers (the upper is the analyser and the lower the polarizer). Since the polarizers are at an angle of 90˚ with each other, when there is no LC sample placed in between, light is extinguished, and we observe a dark state. We observe a similar case with an isotropic liquid, as the polarized light passing through the first polarizer is unaffected by the isotropic liquid and no light exits the analyser. On the other hand, when a birefringent LC material is placed between the crossed polarizers, different optical textures can be observed depending on its phase structure and the LC alignment within the sample i.e., when the director is oriented along either of the polarizers, the light is extinguished.

2.2 Carbon nanotubes

Carbon has several allotropes in various dimensional forms, such as zero-dimensional fullerenes, one-dimensional carbon nanotubes (CNTs), two-dimensional graphene and three-dimensional graphite and diamond. Amongst these, CNTs have attracted much attention since their discovery by Sumio Iijima in 1991 [63] owing to their exceptional electrical [8][9] and mechanical properties [10][11]. CNTs are considered as seamless hollow cylindrical tubes of rolled-up graphene sheets with carbon atoms arranged in a honeycomb (hexagonal) structure. Depending on the number of layers of the rolled graphene sheets (graphitic layers), they can be categorized into single-walled carbon nanotubes (SWCNT) and multi-walled carbon nanotubes (MWCNT) [64], as shown in Figure 11. The diameters of CNTs can vary from 0.4 nm to 3 nm for SWCNTs and from 1.4 nm to at least 100 nm diameter and an inter-layer spacing of 0.34 nm for MWCNTs [65][66]. The lengths of the CNTs can vary from 100 nm up to several microns [64].

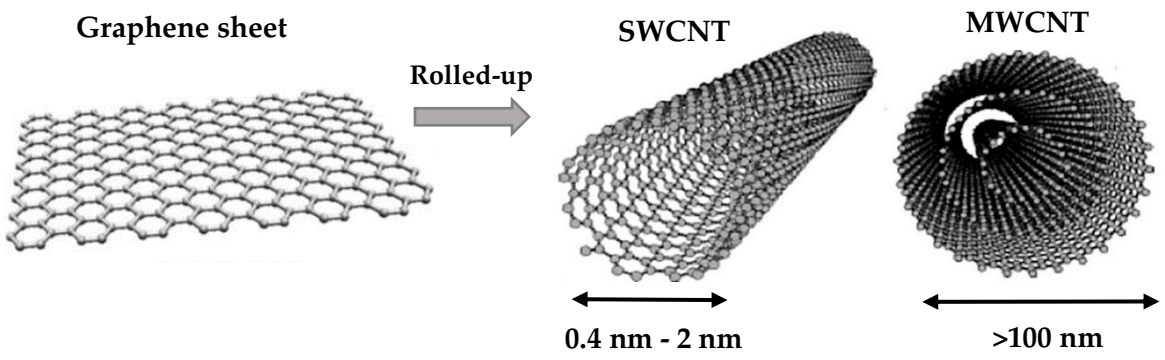

Figure 11: Schematic representation of graphene sheet, single-walled CNT and multi-walled CNT. Adapted from [182][183].

The three commonly used techniques to grow the CNTs are arc-discharge [63], laser ablation [67] and chemical vapour deposition (CVD) [68]. Arc-discharge and laser ablation methods depend on the vaporization of a carbon source at temperatures > 3000˚C. These methods are used for the small-scale production of high quality CNTs. However, since both these methods involve the evaporation of the carbon source, especially at high temperatures, these

are unfavourable for industrial-scale productions. Furthermore, these methods grow highly entangled CNTs that are often mixed with amorphous carbon or metal impurities. This contributes to the need of difficult post-growth purification processes. Chemical vapour deposition, on the other hand, is the only economically viable growth technique for large-scale CNT synthesis as a continuous production of CNT is possible under relatively controlled conditions. CVD involves the catalytic decomposition of a carbon feedstock in the presence of metal catalysts such as nickel, cobalt, or iron at ~700˚C in a flow furnace at atmospheric pressure [68]. CVD is a promising growth technique for mass production also because it is easy to scale-up the growth by increasing the chamber size. Both the MWCNTs used in this work are synthesised by CVD process. The MWCNTs in powder form were purchased from SES Research Inc. and the MWCNT forest was purchased from A-Tech System Ltd., Republic of Korea. The growth details of the MWCNT forest is as described in Ref. [69]. Further details will be elaborated in Section 4.2. The SWCNTs used in this work were purchased from Unidym Inc. and were grown via high pressure carbon monoxide (HiPco) method [70] by using carbon monoxide gas as the carbon source.

2.2.1 Structural configuration of CNTs

The structural configuration of SWCNTs, such as the diameter and chirality, can significantly influence their properties such as electrical conductivity [71]. Electronically, SWCNTs can be metallic, small-gap semiconducting or semiconducting, depending on the chirality, i.e., how the graphene sheet is rolled-up with respect to the tube axis [72]. This is described by a chiral vector $\boldsymbol{C} = m\mathbf{a}_1 + n\mathbf{a}_2$, where m and n are integers representing the chiral indices and $\mathbf{a}_1$ and $\mathbf{a}_2$ are the lattice vectors of the graphene sheet, as shown in Figure 12(a). Depending on the type of chirality, i.e., the values of m and n and the chiral angle θ, CNTs can have different structural forms: if $m = n$ and $\theta = 30^\circ$, CNTs are called 'armchair'; if $n = 0$ and $m > 0$ and $\theta = 0^\circ$, they are 'zigzag' and all other tubes with $m > n > 0$ and $\theta = 0^\circ < |\theta| < 30^\circ$ are 'chiral'. The terms 'armchair' and 'zigzag' refer to the positioning of the hexagonal rings along the circumference of the tube [73], as illustrated in Figure 12(b). All armchair CNTs, i.e., (m, m) types are metallic with no band gap. CNTs with $m - n = 3q$ where q is an integer, are

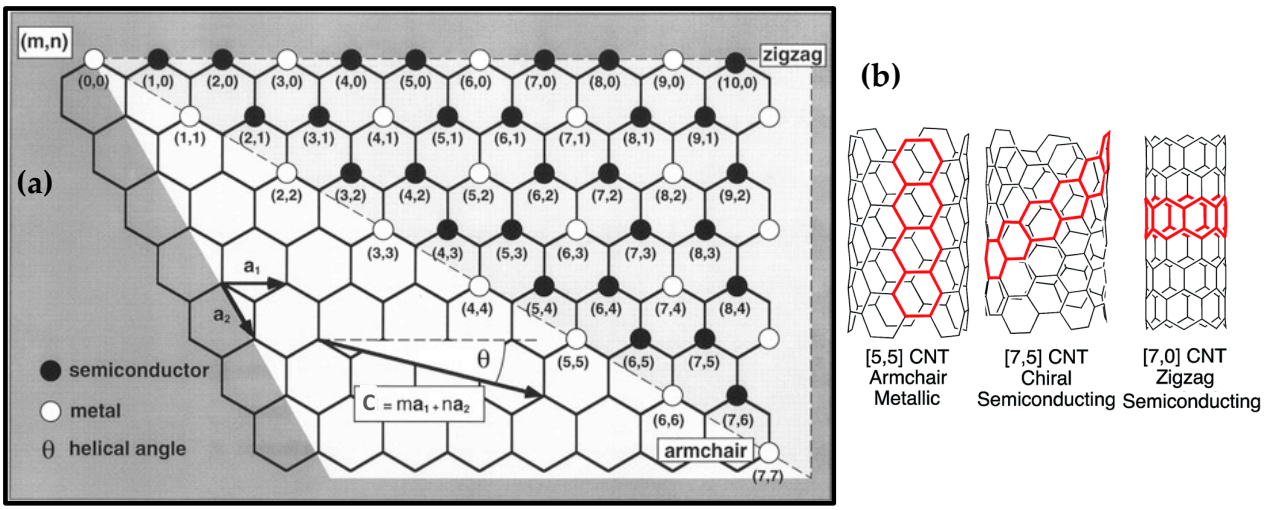

Figure 12: Schematic: (a) representation of the relation between the integers (m, n) and the electronic property of the CNTs, adapted from Ref. [65]. (b) illustrations of armchair, chiral and zigzag CNT structures, adapted from Ref. [184].

semiconducting with a small band gap induced by the curvature of the graphene and are known as semimetallic, quasimetallic, or small-gap semiconducting CNTs [74]. All other CNTs with $n \neq m$ are semiconducting with a band gap that inversely depends on the CNT diameter. The diameter d_{tube} and the chiral angle θ can be evaluated from the values of m and n as [75],

$$d_{tube} = \frac{|C|}{\pi}; \quad |C| = \mathrm{a}\sqrt{m^2 + mn + n^2} \tag{3}$$

$$\theta = \tan^{-1}\frac{\sqrt{3}\,n}{2m+n} \tag{4}$$

where the lattice constant $a=\sqrt{3}\,a_{C\text{-}C}= 0.246$ nm and C-C bond length $a_{C\text{-}C}= 0.142$ nm.

MWCNTs consist of several layers of concentric rolled-up graphitic sheets. Although most MWCNTs are metallic, it is difficult to determine their chirality due to the multiple coaxially nested single-walled tubes. If at least one tube has metallic chirality, the behaviour of MWCNTs is metallic [76]. However, the electronic transport of MWCNTs is considered to be similar to SWCNTs since the majority of the current passing through the MWCNT is confined to its outermost tube [77].

2.2.2 Properties of CNTs

Carbon nanotubes ascribe their extraordinary electrical and mechanical properties to the peculiar electronic structure of graphene. Similar to graphene, CNTs possess covalent sp^2 bonds between individual carbon atoms. In sp^2 hybridization, as in the case of graphene, one s-orbital and two p-orbitals (p_x , p_y) contribute to a planar assembly with a 120° angle between the hybrid orbitals to form a σ-bond and the p_z orbital perpendicular to the sp^2 orbital forming the π-bond [72]. CNTs are flexible and light, yet they have high mechanical strength [21] owing to the strong covalent sp^2 bonds between the carbon atoms. Individual CNTs can exhibit a Young's modulus up to ~1 TPa [78] and tensile strength ~100 GPa [79][80], the highest among all the known materials. However, there is a significant reduction in the effective strength of the macroscopic CNT assemblies due to the weak shear interactions between the adjacent tubes [80][78].

When graphene sheets are rolled-up, the σ and π bonds overlap, resulting in σ - π rehybridization because of the CNT sidewall curvature. This leads to an asymmetric distribution of the π-orbitals inside and outside of the CNT wall with more π-electron confinement outside the CNT wall, contributing to the high electrical conductivity of CNTs.

The attractive aspect of the one-dimensional structure of CNTs is the aspect ratio that can be as high as ~10^7: 1, resulting from diameters of few nanometres and lengths up to several centimetres [81], thus exhibiting anisotropic properties along both the radial and axial directions. Additionally, they form conductive networks with extremely small amount. CNTs, however, usually form bundles and agglomerates due to their high aspect ratio and high van der Waals attractive forces, which limits their practicality and the attainment of uniform and thin networks. Post-growth procedures, such as unbundling and stabilization of liquid suspensions of carbon nanotubes, are therefore necessary stages for practical applications. The details of this will be elaborated in Section 3.4.2.

Due to the existence of strong anisotropy in the properties of carbon nanotubes, it is always crucial to consider the orientation of CNTs in the axial direction when nanotubes are to be used in practical applications. In a macroscopic CNT assembly, the properties of the

individual nanotubes are preserved better if the nanotubes are well aligned in the same direction. CNT alignment can be achieved via two different techniques depending on when the alignment is achieved: *in situ* techniques, where the CNT alignment can be achieved during the nanotube growth process, and *ex situ* techniques where the CNT is initially grown randomly and then aligned afterwards [82]. The well-aligned MWCNT sheets that we use are from *in situ* vertically aligned forests and *ex situ* aligned on a substrate by mechanically drawing them from the sidewall of a MWCNT forest. This will be discussed in detail in Section 4.3.

2.3 Electrical conduction mechanism of CNT networks

A carbon nanotube network can be perceived as a network consisting of large amounts of either randomly or well-oriented individual nanotubes and small bundles of CNTs. It is worth mentioning that those nanotubes within a CNT network that form conductive paths between the electrodes only contribute to electrical conduction. The conductive behaviour of carbon nanotube networks depends on the modification of two main types of resistance: (1) the inherent tube resistance (R_{CNT}) of the CNT itself and (2) the inter-tube resistances of nanotubes that are in contact or in close vicinity. When an external pressure is applied to a CNT network, the change in resistance is due to the changes in either intrinsic tube resistance or inter-tube resistance.

2.3.1 Intrinsic tube resistance

Carbon nanotubes have excellent electrical conductivity owing to their one-dimensional nanostructure that permits ballistic transport of electrons [22][77]. Studies report the intrinsic resistance of multi-walled CNTs to be as low as 0.2–0.4 kΩ/μm [83][84]. The intrinsic resistance of carbon nanotubes is highly sensitive to mechanical strain and increased significantly at relatively small strain [12][85][86][87][88]. This is because an external strain can shift the energy band gap of the individual tubes, in turn affecting the conductivity. It was observed that the intrinsic resistance of a CNT shows an exponential

behaviour with the external strain [89] that depends on the chirality of the individual nanotubes.

2.3.2 Inter-tube resistance

The electrical conduction in a CNT network is not equally efficient in comparison to the inherent high conductivity of the individual nanotubes. This is because the inter-tube resistances are considerably higher than the intrinsic tube resistance. The inter-tube resistance can be altered via external strain by widening the inter-tube distance. Nevertheless, relative to the intrinsic tube resistance, the impact of an external strain on the inter-tube resistance is less significant. The inter-tube resistance is further divided into two categories: contact resistance (R_C) [90][91] of physically connected tubes, where electrical conduction between them is possible via electron diffusion, and tunneling resistance (R_T) [92][93] of CNTs separated by a small inter-tube distance, where conduction occurs via tunnelling or hopping mechanism. Previous studies demonstrate that R_C strongly depends on the contact region [91][90]. Tunneling resistance can be numerically estimated as follows [93][94]:

$$R_T = \frac{h^2 d}{Ae^2\sqrt{2m\lambda}} e^{\frac{4\pi d\sqrt{2m\lambda}}{h}} \quad (5)$$

where d is the inter-tube distance, h is Planck's constant, e is the quantum of electricity, m the electron mass, λ is the height of the potential barrier and A is the cross-sectional area of the tunnel.

2.4 Carbon nanotube-based pressure sensors

The pressure sensors with carbon nanotubes previously reported in the literature measure changes of resistance with applied pressure using both films [95] and individual CNTs

[96][97]. Additionally, vertically aligned CNTs, known as CNT forests, have good electromechanical properties [98]. Pressure sensors based on these forests have also been realized and reported [99][100]. In the field of microelectronics, Fujitsu [101] and Infineon [102] have conducted extensive studies and proposed vertically grown carbon nanotubes as vertical interconnects.

However, these fabrication techniques have certain limitations. The aforementioned sensors are built using complex and multi-step processes. In most cases, the CNTs are grown in specific locations, which require additional manufacturing steps. Such sensors based on the integration of as-grown CNTs can suffer limitations in terms of control of CNT purity, quality, and chirality. Furthermore, it is difficult to control the density of the vertical CNTs as lower densities can only be attained with samples formed by shorter tubes and higher density when the CNTs are grown as forests. Reliable fabrication of nanoscale sensors using individual nanotubes is challenging because of the difficulties of precise localized growth and, thus, sensors based on single tubes have the problem of reproducibility since the tubes have inherent structural and electronic differences that affect their mechanical and conductive properties. Another limitation is that individual CNTs have a limited maximum length up to which they can preserve their structure and optimal properties.

2.5 Why CNTs + LCs based pressure sensors?

Liquid crystals in combination with carbon nanotubes are an interesting area of research, as this alliance is a peculiar assembly of anisotropic nanoparticles (carbon nanotubes) in an anisotropic media (liquid crystal). As a reminder, CNTs are rolled-up graphene sheets with carbon atoms arranged in a honeycomb or hexagonal structure. The liquid crystal 5CB also has aromatic rings in its structure; this results in a LC-CNT interaction known as π-π electron stacking, where the aromatic rings of the LC stack on top of the honeycomb structure of the CNT with a binding energy of -2 eV [103].

Owing to the strong LC-CNT surface anchoring arising from the π-π interactions [103] between the CNTs and the LC molecules, the LC self-assembly can be used to align the dispersed CNTs [104][105]. The LC molecules will position tangentially with no fixed orientation on the CNT surface and once the LC is oriented along the director $\boldsymbol{n}$, via surface treatments or electric fields, the CNTs follow the same orientation. Likewise, if they are well-aligned, the anisotropic nature of CNT ensembles can orient the nematic LC molecules on a given substrate, either as films of nanotube bundles [106] or as sheets [27][107].

As pure liquid crystals are dielectric materials, there are neither free charge carriers nor the formation of any conducting paths between the electrodes. The modulation of conductivity, if any, due to ions present in the LC by external stimuli, such as pressure, temperature, electric or magnetic fields, is therefore considerably lower. Thus, to enhance the conductivity response of LCs and to be used for functional applications, they are often doped with nanoparticles [108][109][110]. When particles are introduced in a nematic medium, depending on its size and anchoring conditions, it may cause elastic perturbations in the LC structure, resulting in the generation of topological defects around the particles [111][112][113]. The different scenarios that can arise will be discussed in detail in Section 3.2.

In this thesis, we have developed two configurations of LC-CNT based pressure sensors. Sensor 1 is a vertical configuration where a vertical interconnect of MWCNT enveloped by a liquid crystal matrix acts as the sensing element. In this case, LC defect line or disclination are tailor-made via creating specific anchoring conditions on the substrate. This defect line then act as a template for the formation of the vertical interconnect. Unlike prior works that rely on the directed growth of CNTs, here we use dispersions of CNTs and thus, the nanotubes can have the required characteristics and purity.

Sensor 2 is a horizontal configuration where well-aligned MWCNT sheets are embedded in LC. Here, CNTs align the adjacent layers of the nematic molecules due to the surface anchoring and the bulk of the LC aligns accordingly. CNT sheets thus, simultaneously act as an aligning layer and a sensing element. CNT sheets are attractive as they can be deposited

onto a desired substrate via a single transfer process, consequently making the sensor fabrication quite simple and straightforward.

Both these pressure sensors do not have any complex fabrication processes and are relatively easy and cost-effective. We have seen above that the electrical properties of carbon nanotubes are strongly dependent on their structural configuration, making CNTs a potentially strong candidate in sensing devices. The pressure response in both these sensors is found to be dependent on the change in resistance of the CNTs, induced by the structural variations under the external applied pressure. The unique combination of CNTs, due to their very good electrical conductivity, low percolation threshold, light weight, and flexible characteristics and LCs, due to their ability to align easily and stably via surface treatments, possibility to reorient to their initial configuration because of their elasticity and softness, make both the pressure sensors developed in this thesis recoverable once pressure is released.

Chapter 3

Interactions of nano-diameter rod and tubular particles with a defect line in a nematic liquid crystal

Overview of the chapter

This chapter focuses on the systematic creation of liquid crystal defect lines, or disclination lines, and specifically those with a topological charge of +½. This is achieved by mechanically imposing conflicting anchoring conditions on the sample substrates. The difference in the trapping behaviour of two types of elongated nanoparticles, which are dissimilar in their actual geometry on a +½ nematic disclination, is also reported. Although both are cylindrical in shape, aggregates of $Mo_6S_2I_8$ nanowires (rod-shaped) and multi-walled carbon nanotubes (tube-shaped, i.e., hollow), trap in a different manner, even if they are because of the perturbations induced in the liquid crystal director field. Single-walled carbon nanotubes were not trapped since their bundles seemed considerably straighter and smaller than those of multi-walled carbon nanotubes and, consequently, neither topological defects nor standard liquid crystal perturbations are expected.

This chapter is primarily based on the publication 'Difference in the interaction of nano-diameter rod and tubular particles with a disclination line in a nematic liquid crystal', published in *RSC Advances* [114].

3.1 Introduction

The dispersion of particles into nematic liquid crystals has gathered much interest in physics and has played a major role in fundamental research through the introduction of a new class of long-range elastic interactions arising from the distorted LC director field [115]. When a particle is inserted into a nematic LC, the director field in the vicinity of the particle is determined by its surface anchoring conditions, i.e., the strength and orientation of the mesogens on its surface. When these boundary constraints impose conflicting orientations on the liquid crystal, topological defects are observed, generating discontinuities in the LC director $\boldsymbol{n}$ [46]. Surface boundary conditions are thus, a crucial factor responsible for the particle interactions and the director field deformation. The nature of the topological defects generated, the LC director configuration, the interactions amongst colloidal inclusions and the effects of different boundary conditions have all been widely studied [54][112] [113][115][116] [117][118][119].

This chapter mainly discusses how two untreated cylindrical nanoparticles that are not homotopically equivalent interact with a disclination line and the differences in trapping behaviour. Inspired by Fleury et al. [26] for their innovative approach to generate LC defect lines in specific locations through controlled surface treatments on the substrates, we have adopted the same technique to create the defect lines. In this work, we used aggregates of $Mo_6S_2I_8$ nanowires as rod-shaped nanoparticles and two types of carbon nanotubes (CNTs), single-walled carbon nanotubes (SWCNT) and multi-walled carbon nanotubes (MWCNT), as tube-shaped nanoparticles. When these nanoparticles are inserted into a uniformly oriented nematic liquid crystal, LC in the proximity of the nanoparticles are forced to deform from the orientation defined by the LC director at the interfacial layers and this locally distorts the nematic director field. The LC will form topological defects around these nanoparticles in order to compensate for the defects created by the particle's presence and so that the total topological charge of the system is zero. These topological defects are a consequence of the boundary conditions defined by the surface anchoring conditions of the particles [113] and hold a critical role in dictating the elastic interactions amongst these nanoparticles and the nematic defect line.

3.2 Inclusions in nematic liquid crystals

Recent studies on the introduction of particles in nematic LC have shown that specific interactions among the inclusions result in self-assembly [113][115][117][119][120]. In a uniformly aligned nematic LC, the elongated organic LC molecules uniformly orient to infinity along their director $\boldsymbol{n}$. When microparticles or colloids are introduced in the nematic environment, due to the elastic distortions of the director field on the particle surface, long-range forces and interactions are induced. To better comprehend the interaction of the particles with a nematic defect line, it is necessary to understand the LC orientation in the vicinity of a single particle with a particular anchoring on its surface.

3.2.1 Homeotropic surface anchoring

When a spherical particle having homeotropic surface anchoring is inserted into a nematic liquid crystal host, LC near the particle are forced to align perpendicularly along the entire surface of the particle, as illustrated in Figure 13. This results in frustration of the LC, leading to the creation of topological defects which cannot be eliminated [113]. The particle itself constitutes a 'radial hedgehog' defect with a topological charge s = +1. In order to maintain the net topological charge neutrality of the system, this topological charge must be

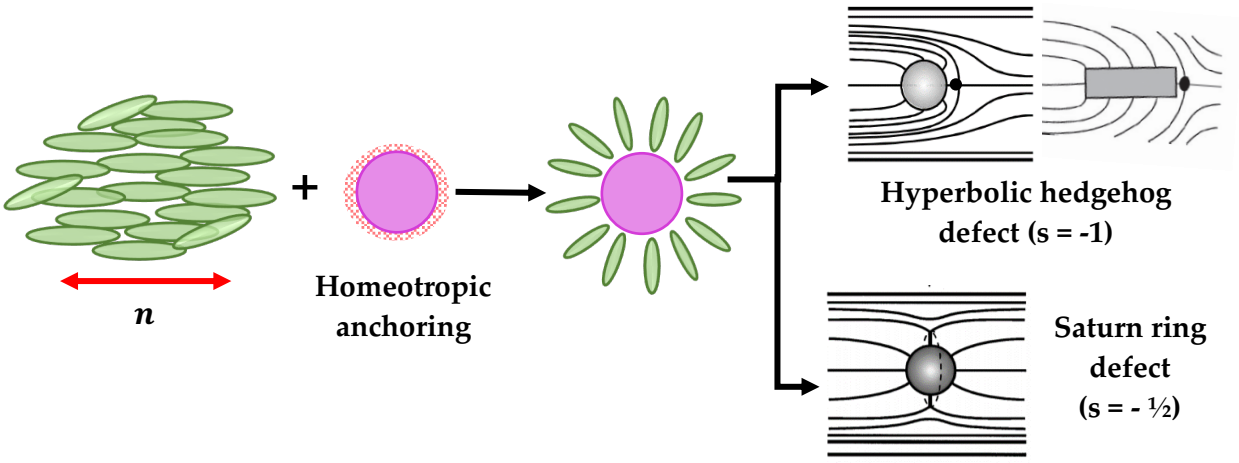

Figure 13: Schematic representation of the possible LC configurations around a spherical particle with homeotropic anchoring at its surface. They can be accompanied by a hyperbolic hedgehog or by a -1/2 disclination loop called a Saturn ring around the equator. The schematic of the director field was adapted from [113][120].

compensated by an additional topological defect in the nematic environment. Therefore, in this case, two types of defects can arise, as seen in Figure 13. First is a 'hyperbolic hedgehog defect' of topological charge of s = -1, called satellite point defect [115][113][117], and second is a 'Saturn-ring defect' [118][121], a disclination loop of strength -½ that surrounds the particle, normal to the far field director at the equatorial plane.

3.2.2 Planar surface anchoring

In the case of tangential boundary conditions, or planar surface anchoring, the director is tangential to the surface of the particle. This results in quadrupolar distortions in the liquid crystal with two surface point defects, called *boojums* [113][117][122] (in Figure 14 indicated by the two dots in the plane each of strength -½), that are polar opposites and aligned along the nematic orientation enforced by the boundary conditions. In the case of micro-rods as inclusions, similar observations were reported, as closed cylinders are topologically equivalent to spheres and, hence, similar defect creations are anticipated [120].

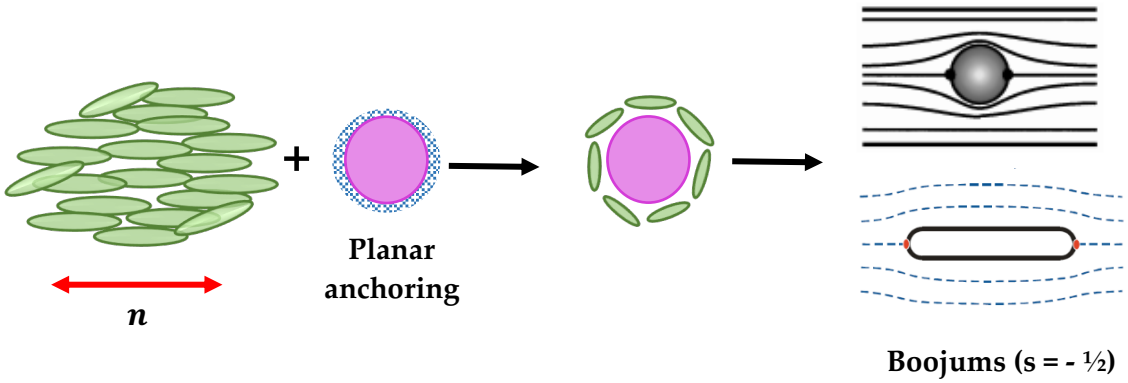

Figure 14: Schematic representation of the possible LC configurations around a spherical particle with planar anchoring at its surface. Two topological defects called boojums appear on either pole. The schematic of the director field were adapted from [113][135].

3.2.3 Nematic field distortion

We consider a particle that has a specific anchoring on its surface introduced into a nematic LC. The ability of this anchoring to orient the adjacent LC molecules and distort the bulk

director $\boldsymbol{n}$ is defined in terms of the characteristic surface extrapolation length $L = \frac{K}{W_a}$, where K is the Frank elastic constant and W_a the anchoring energy of the nematic molecules at the surface of the particle. Depending on the extrapolation length and preferred surface anchoring conditions, different director field structures can form around a single particle [112][111]. When the extrapolation length [46] becomes much greater than the radius of the particle R, Eq. (6), then, the orientation of the LC molecules is no longer defined by the specific angle given by the surface conditions on the particle, i.e., the anchoring is weak.

$$\frac{K}{W_a R} = \frac{L}{R} \gg 1 \tag{6}$$

In such a case, the LC is unperturbed. This is the case when extrapolation length tends to infinity: the bulk elastic energy dominates and can enforce a uniform LC orientation on the particle surface, thus avoiding the generation of any particle-associated defects, as seen in Figure 15 for an elongated and for a spherical particle.

Conversely, when the particle radius R is much greater than the extrapolation length L and the anchoring is strong, the molecular orientation at the particle surface is determined by the surface anchoring conditions and thus it conflicts with the bulk LC alignment. The LC cannot thus accommodate the particles by continuous elastic strain, ultimately resulting in the generation of topological defects.

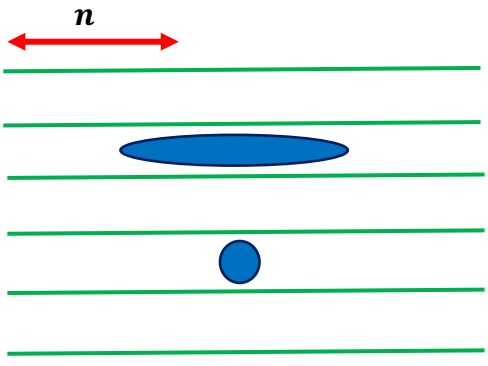

Figure 15: Illustration of the uniform configuration of LC director on the surface of an elongated and spherical particle. Here, the LC environment is unperturbed, and thus no nematic interaction is created upon dispersing them.

3.3 Creation of defect lines and cell preparation

The cell consists of two soda-lime glass substrates (purchased from DURAN Group, Germany) cut into dimensions of 20 mm × 20 mm × 1 mm. The substrates were consecutively rinsed in ultrasonic baths with acetone, isopropanol and distilled water. The substrates were then dried using an air blowgun followed by dehydration baking on a hot plate for 10 min at 100°C.

A thin layer of polytetrafluoroethylene (PTFE, or Teflon) can be smeared unidirectionally on a glass substrate in order to obtain a uniformly oriented nematic phase, adopting a technique introduced by Haller [123] and later modified by Wittmann and Smith [124]. For this purpose, the substrates are placed on a hot plate at a temperature of ~200°C and a suitably shaped Teflon bar is brought into direct contact with the glass substrate, as in Figure 16 [125]. At the glass-Teflon interface, as the Teflon is in a molten state, it is possible to deposit the polymer simply by smearing on the substrate. Using this technique, a thin layer (~1 μm thickness) of Teflon is coated on the substrate with the polymer chains aligned in the direction of rubbing. For better reproducibility of surface treatments, we re-sharpened the Teflon tip before each treatment. This surface treatment provides a strong unidirectional planar anchoring, perfectly fixing the orientation of the liquid crystal director $\boldsymbol{n}$. By controlling the LC boundary conditions, we can generate a defect line by inducing planar liquid crystal alignment with three areas of dissimilar director orientations.

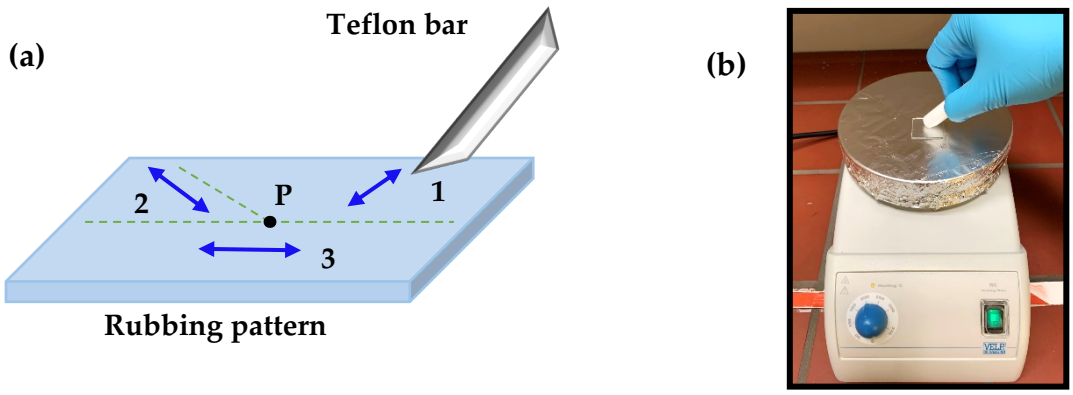

Figure 16: (a) Illustration of the glass substrate showing the rubbing directions of the Teflon bar. (b) Teflon rubbing on a substrate placed on a hot plate.

We use a triple rubbing technique consisting of three different directions generated around a point, as shown in Figure 16. The first rubbing is done at an angle of 60° along the whole surface of the substrate; the second rubbing is done at an angle of 120° along the vertical half of the substrate; and, finally, the third rubbing is done at an angle of 0° along the horizontal half of the substrate. Each rubbing will completely cover the one before it, so, in the end, we will have three different alignment directions on the same substrate. At the intersection of the three rubbing areas, the substrates will have conflicting planar anchoring on their surfaces and the LC molecules will be unable to orient along any specific direction, creating a point defect. Two glass substrates, smeared with Teflon by the triple rubbing technique, were positioned with appropriate spacing (~150 μm defined using isolated copper wires) on top of each other, as shown in Figure 17(b), such that the inward surfaces have the smeared Teflon film facing each other. Next, a nematic LC is filled in through capillary filling. The nematic distortions involving the continuous variation of the nematic director $\boldsymbol{n}$ will result in a disclination line of topological strength ½.

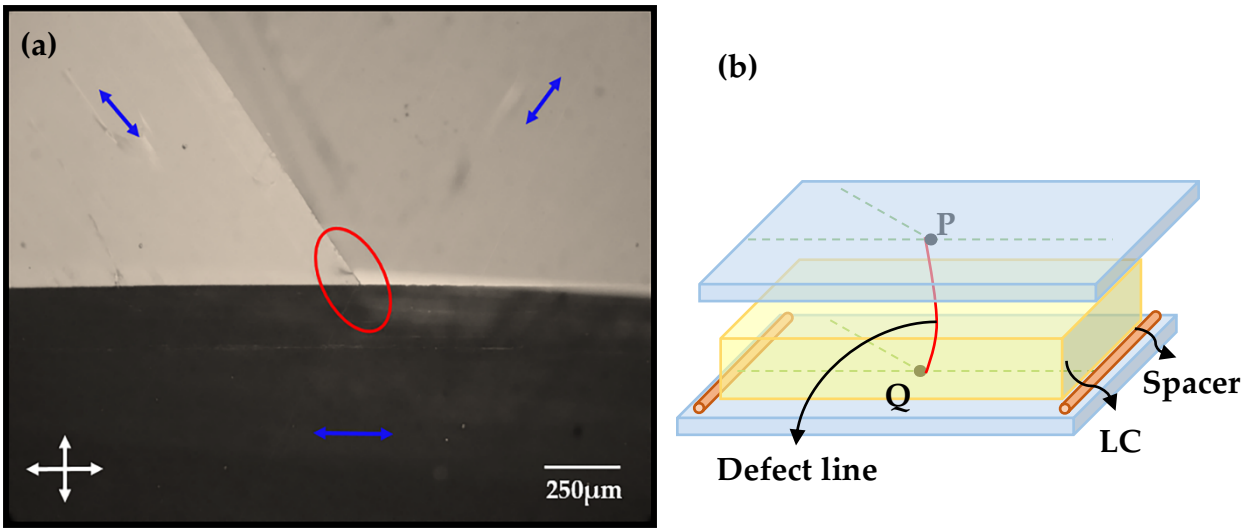

Figure 17: (a) Micrograph of a cell with two Teflon coated substrates filled with 5CB nematic liquid crystal observed between crossed polarizers. The defect line is indicated within the red oval. The blue arrows indicate the bulk LC alignment direction. (b) Schematic of the defect line created once the top and bottom substrates are sandwiched. Points P and Q represent the point defects on the surface and the red line represent the defect line.

The liquid crystal used in this research is a room temperature nematic LC, 4-cyano-4'-pentylbiphenyl, commonly known as 5CB, purchased from Synthon Chemicals (Germany), and used without further purification. The nematic to isotropic transition temperature of 5CB is 35.5˚C. When introduced into the customized cell, the LC aligns along the different directions, as observed between crossed polarizers in Figure 17(a), captured using a digital camera (Canon EOS 6D) mounted on a polarizing optical microscope (Nikon Eclipse LV100ND). The LC director orientations are indicated with blue arrows to aid the understanding of the three distinct orientationally ordered monodomains. The orientation of the LC is uniform in these monodomains, except close to their boundaries, along which the orientation gently changes from one domain to the other. A defect line is formed connecting the top and bottom substrates in response to the convergence of the three monodomains, as indicated within the red oval in Figure 17(a). The main objective is to trap untreated cylindrical nanoparticles that are not homotopically equivalent, particularly nanowires and nanotubes on the defect line, and analyse their trapping mechanism. For this task, dispersions of CNTs and nanowires in LC must be prepared, as described in the next section.

3.4 Characterization and dispersion of the particles

In this study, we used $Mo_6S_2I_8$ nanowires as the rod-shaped particles and CNTs of two types, single-walled carbon nanotubes (SWCNT) and multi-walled carbon nanotubes (MWCNT), as tube-shaped particles to analyse their trapping behaviour towards the defect lines in the context of their topological difference. One of the main obstacles in realizing these is the challenge of achieving a good nanoparticle dispersion in the nematic matrix. To resolve this, here we use a mechanical approach of ultrasonic treatment to improve the dispersibility, especially, of the CNT nanoparticles. Prior to introduction in the nematic medium, the nature, and morphology of the dispersed particles were characterized via analysing the scanning electron microscope (SEM) images of both the types of carbon nanotubes and $Mo_6S_2I_8$ nanowires after the dispersion procedures.

3.4.1 $Mo_6S_2I_8$ nanowires

$Mo_6S_2I_8$ nanowires are inorganic materials in the category of nanowires composed of molybdenum, sulphur, and iodine (MoSI). The nanowires studied in this thesis were kindly provided by Dr. Aleš Mrzel from the Jožef Stefan Institute in Ljubljana, Slovenia. These nanowires or nanorods have many advantages including ease of fabrication, monodisperse diameters, metallic behaviour [126] and easier dispersion compared to CNTs. They were synthesised directly from the elements mixed in the desired stoichiometry as reported in reference [127]. The resultant material is a powder consisting of bundles of individual nanowires each with sub-nanometre diameter. The bundles are generally 50–80 nm in diameter and their length was up to several micrometres [128]. The nanowires were inserted directly in the nematic liquid crystal (0.01% by weight) and dispersed for 2–3 min using pulsed ultrasound waves generated by a Hielscher UP200St tip probe ultrasonicator (36 W) before introduction into the cell. For scanning electron microscopy (SEM, JEOL JSM-6010LA) observations, the nanowires were dispersed with ultrasounds in distilled water for

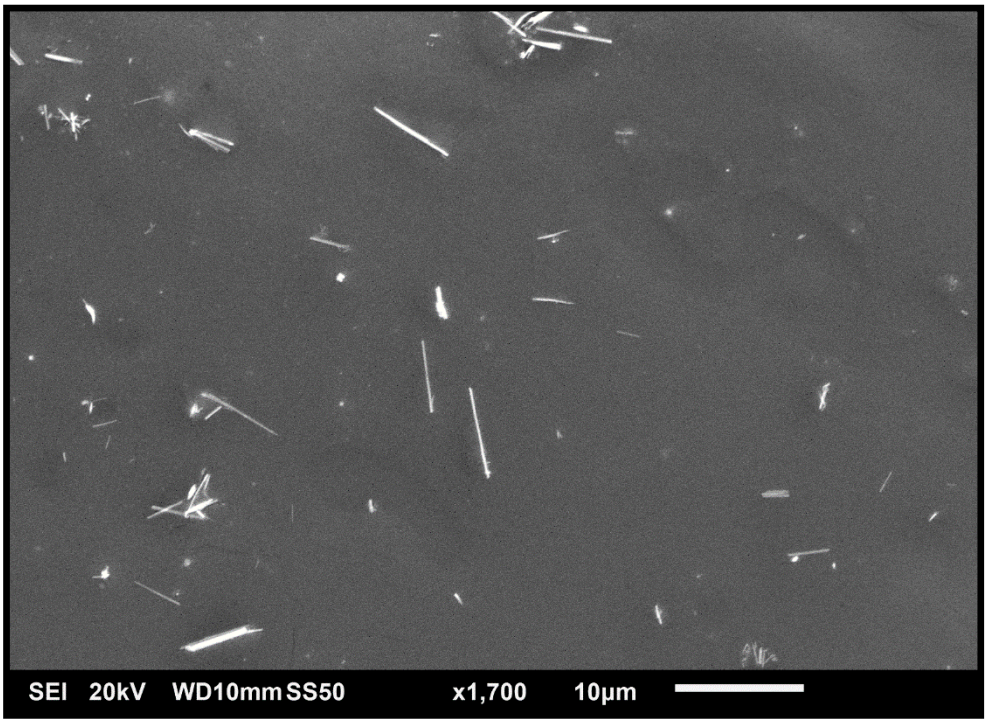

Figure 18: Scanning electron microscope (SEM) image of $Mo_6S_2I_8$ nanowires after dispersed in deionized water.

2 min, deposited on silicon wafer, and dried at room temperature, Figure 18. They mostly appear as monodisperse straight rigid rods, although some of them appear to be broken and as large aggregates.

3.4.2 Carbon nanotubes

Large-scale synthesis methods of nanotubes generally produce bundles comprised of up to hundreds of single nanotubes. The high aspect ratio of the nanotubes coupled with their pliability contributes to physical tangling, and individual nanotubes naturally assemble into "ropes" held together by van der Waals forces [10]. They thus tend to be agglomerated and, for practical applications, debundling and stabilising dispersion techniques are required [129]. Both physical and chemical strategies have been explored to resolve this issue. Mechanical or physical approaches are mainly based on sonication treatments in appropriate solvents. Covalent chemical modifications of CNTs include both end-group [130] and sidewall [131] functionalization.

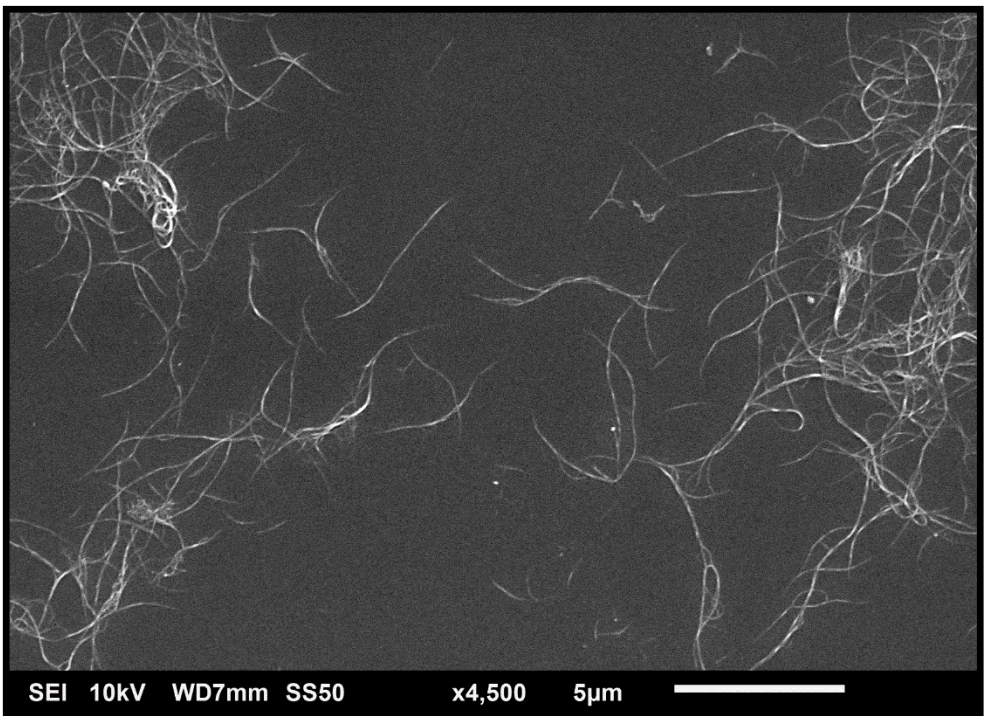

Figure 19: SEM image of single-walled CNTs dispersed in dichloromethane and deposited on a silicon wafer.

In this work, two types of carbon nanotubes were used, as purchased: single-walled CNTs (SWCNT) having diameter ~0.8 nm–1.2 nm obtained from Unidym Inc. (Lot# P2772) and multi-walled CNTs (MWCNT) of length 5 µm–15 µm and 60 nm–100 nm outer diameter from SES Research Inc. (Lot US - 0551). Here, we disperse both the carbon nanotubes (0.1% by weight) in dichloromethane CH_2Cl_2 (DCM) via mechanical treatment using a probe ultrasonicator (36 W) for about 70 min. The resulting colloidal dispersion showed a stable dispersion for over two weeks.

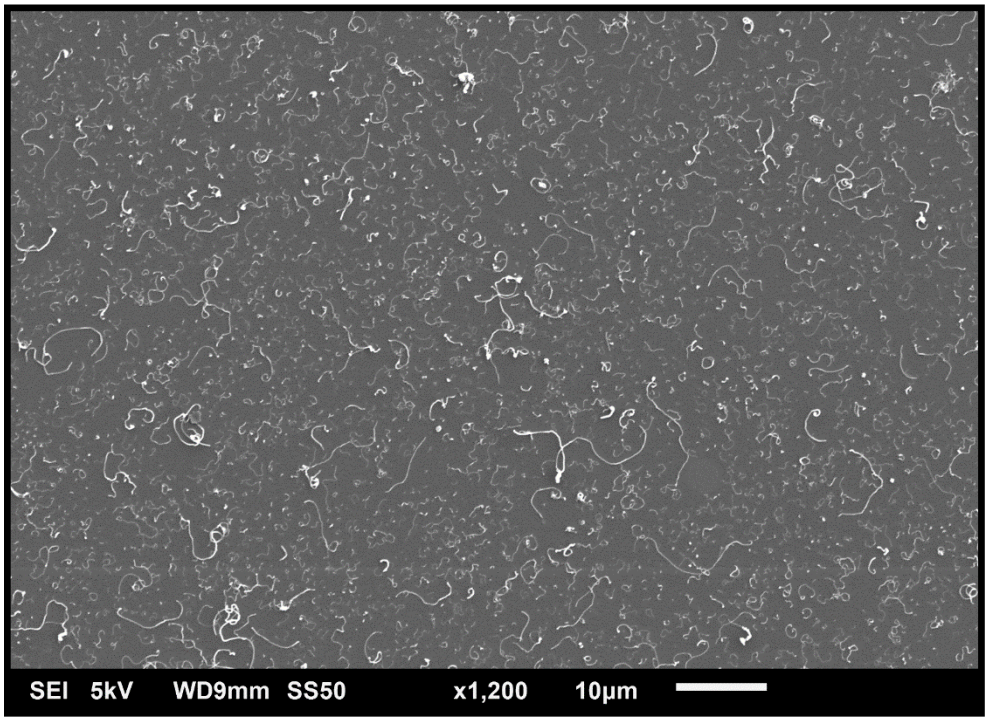

Figure 20: SEM of multi-walled CNTs dispersed in dichloromethane and deposited on a silicon wafer

Figure 19 and Figure 20 show the SEM images of both the CNTs deposited on a silicon wafer after dispersion and solvent evaporation. Both images reveal a good dispersion of CNTs and the absence of large bundles or entangled aggregates. We observe that, for SWCNTs, the tubes seem to be comparatively straighter than the MWCNTs that appear with kinks, a sign of defects created in the walls that cause local bending.

The CNT dispersion in DCM was then inserted into the nematic liquid crystal 5CB and then heated to 80°C for ~10 min to evaporate the solvent and achieve a concentration of 0.01% by weight in LC. This mixture was then inserted into the cell with its substrates treated to induce a defect line in a predefined position, as described in Section 3.3.

3.5 Interactions of nanotubes and nanowires with the defect line

Surface treatments are usually performed in order to obtain the desired LC orientation on the surface of the particles. In contrast, the surfaces of both the elongated nanostructures were untreated in our study to explore the trapping mechanisms only in the context of their topological differences and not due to any surface anchoring modifications. When nanoparticles whose surfaces have strong infinite anchoring are inserted into a uniformly aligned nematic LC, the interactions between the surface of the particle and the LC create an energetically favoured orientation for the nematic alignment. Such preferences distort the otherwise uniform alignment with a subsequent elastic free energy cost. The tendency to minimize this energy can result in forces on the particles, which attracts them towards the defect line.

When $Mo_6S_2I_8$ nanowires are introduced into a uniformly oriented nematic liquid crystal, LC molecules orient tangentially to their surfaces along the long axis of the nanowires [132][133]. The elastic deformations around these nanowires impose topological constraints that should be fulfilled by the director, resulting in the generation of topological defects. Deformations in the uniform director field increase the elastic free energy of the LC nematic medium, as defined by the Frank-Oseen elastic free energy density, shown in Eq. (2) [55]. Consequently, the director field is directed towards a state, which minimises the overall free energy while still satisfying the topological constraints imposed by the boundary conditions. To maintain the total topological neutrality, two antipodal surface defects of -½ strength, boojums appear symmetrically at the opposite poles of the nanowire as shown in Figure 21.

The nanowire-boojums assembly generates two opposite splay moments $\boldsymbol{P_s}$ of a dipolar nature and both together correspond to a quadrupole moment $\boldsymbol{Q_s}$ [117], which interacts with the splay distortion formed by the defect line. The elastic interaction between the two can be expressed as the coupling of the quadrupolar moment $\boldsymbol{Q_s}$ to the splay field $\boldsymbol{n}$ ($\nabla \cdot \boldsymbol{n}$) generated by the disclination line, and is given by

$$U = -K\, Q_s\, \boldsymbol{n} \cdot \nabla (\nabla \cdot \boldsymbol{n}) \qquad (7)$$

where K is the LC splay elastic constant. A resulting nematic force is derived from this interaction potential [60], given by $\boldsymbol{F_{particle-line}} = -\nabla U$.

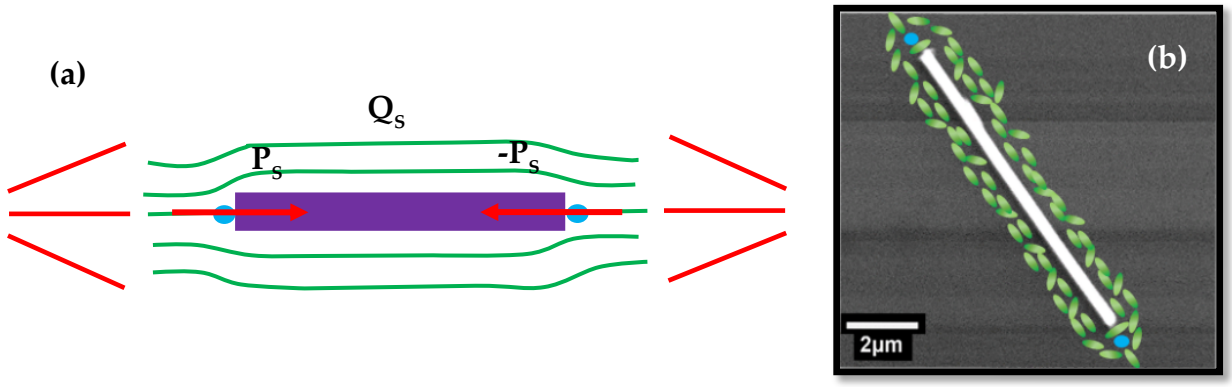

Figure 21: Schematic of (a) a nanowire having planar surface anchoring, generating opposite splay distortions (marked in red) and thus having two opposite splay dipole moments *Ps*. The green lines denote the director field lines. (b) SEM image of a nanowire with illustrations of LC molecule orientation (not to scale) around it. The blue dots represent the two boojums.

MWCNTs, on the other hand, are curved bundles, as seen in Figure 20, and hence generate a bend distortion in the nematic medium, Figure 22. It has been experimentally shown that a bend distortion is produced for a spherical particle with planar alignment, that generates defects in asymmetric configuration [134]. It interacts with the elastic distortion of type bend generated by the disclination line.

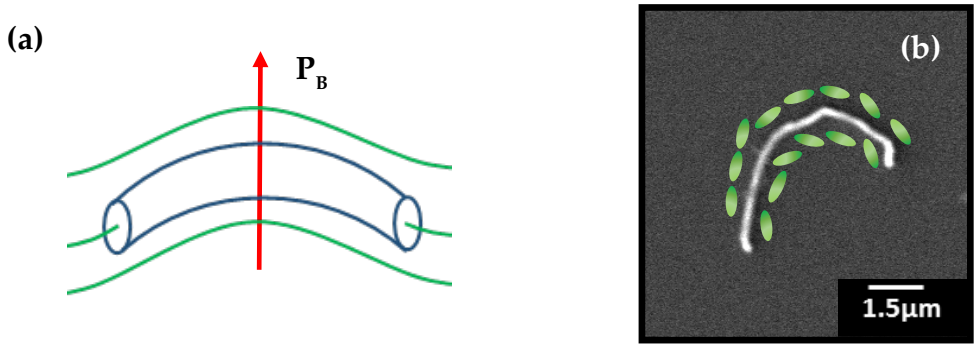

Figure 22: Schematic of (a) bent MWCNT producing a bend dipole moment P_B. The green lines denote the director field lines. (b) SEM image of a bend MWCNT with illustrations of the LC molecule (not to scale) orientation around it.

The elastic interaction U between the two can be expressed as the coupling of the bend moment $\boldsymbol{P_B}$ produced by the particle, to the bend field [60] $\boldsymbol{n} \times (\nabla \times \boldsymbol{n})$ generated by the defect line, and is given by

$$U = -K\,\boldsymbol{P_B}.(\boldsymbol{n} \times (\nabla \times \boldsymbol{n})) \quad (8)$$

Therefore, in this scenario, we would predict a stronger nematic force $\boldsymbol{F_d} \sim 1/r^2$ originating from a dipolar potential than the quadrupolar case, where r is the distance of the particle from the defect line. We can state that this configuration can have similarities to the case of the bent MWCNTs even though there are no topological defects leading to large local distortions of the director. Nevertheless, the observed force behaves contrarily as for a quadrupolar interaction $\boldsymbol{F_q} \sim 1/r^3$, expected for the straight nanowires.

3.6 Particle Tracking Method

In this study, we have analysed the defect-trapping trajectories of elongated aggregates of nano-diameter particles of similar dimensions. The distance measurements and travel-time calculation were performed using a standard particle tracking technique. The nanoparticles introduced in the nematic LC acted also as tracers for the measurements. The aggregation of CNTs into very large, disordered structures was avoided by using a very low concentration of CNTs and by using dispersions immediately after sonication. The approach of the particles

towards the defect line was observed using a polarizing optical microscope (Nikon Eclipse LV100ND) and a digital camera (Canon EOS 6D) mounted on the top generates a sequence of images at discrete time intervals (15 s). The images were analysed using an imaging processing program, ImageJ. Each location of the particle during its motion towards the defect line was monitored by assigning (x, y) coordinates. The instantaneous velocity of the nanoparticle can be evaluated from the time-derivative of the recorded trajectory. Consequently, the force of attraction can be determined from the velocity. It is critical that there is no hydrodynamic flow within the sample that may interfere with the particle's trajectory, and the only forces acting on the particle are the Stokes' drag and nematic force.

3.7 Confinement of nanoparticles on the disclination

3.7.1 Non-trapping of SWCNTs

We reconstructed the trajectory of the nanostructures (SWCNT, MWCNT, and $Mo_6S_2I_8$ nanowires) during their approach towards the defect line using the standard particle tracking method as discussed above.

In our study, in the case of SWCNTs, we found no trapping even after several hours of leaving the cell, as seen in Figure 23(a-c). For further confirmation, the sample was heated to isotropic phase and if the SWCNTs were drawn into the disclination, traces of large aggregates or bundles would have been evident once the defect line disappeared. One reason for not trapping may be that, besides being small, the SWCNTs appear too straight to create sufficient perturbations in the surrounding nematic medium. For highly distorted nanotubes, the Brownian motion induces major fluctuations that dominate the movement of the SWCNTs towards the disclination. In addition, Agha et.al [60] theoretically calculated the minimum particle radius to be ~30 nm for the particles to become definitively trapped onto a disclination. Consequently, the nanoscale diameter of isolated single-walled CNTs can prove a challenge as it is indeed smaller than the above-estimated value. Therefore, compared to the thermal fluctuations dispersing the SWCNTs, their interaction with the

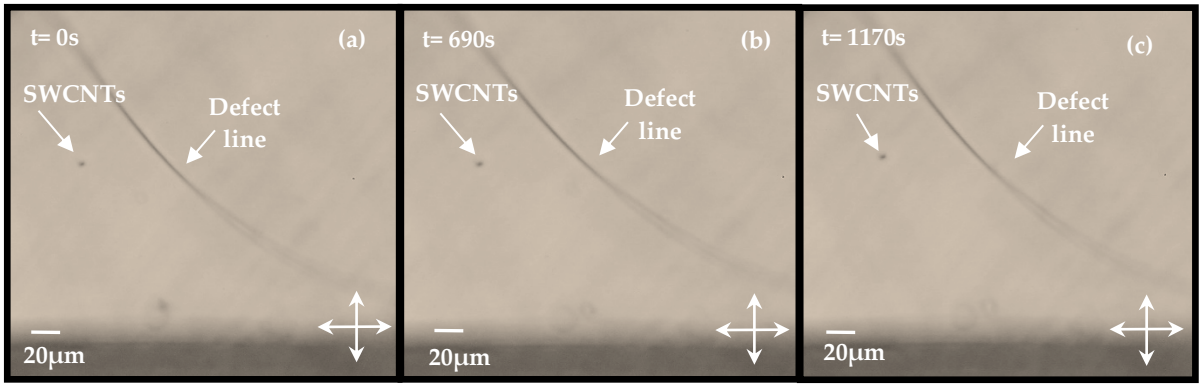

Figure 23: Micrographs tracking the position of SWCNT aggregates as a function of time observed between crossed polarizers. Here, the points P and Q (shown in Figure 17b) are not on top of each other for better view and thus, the defect lines are long and oblique.

defect line can be assumed either non-existent or negligible in order to be able to attract them to the defect line.

Moreover, as carbon nanotubes are hollow, the LC orientation at the tube ends differs from what is estimated in the rigid rod approximation model, wherein a similar LC alignment exists throughout the rod surface as well as the ends. If the anchoring is planar, the nematic director is normal to the rod axis, creating conflicting LC orientations in the uniform alignment of the surrounding LC [135]. For CNTs, the alignment of the LC molecules at the tube ends is along the same directions as the tube wall, i.e., along the direction of the tube long axis, which is, in turn, along the bulk nematic director. SWCNTs generally exist in bundles and aggregates and, although these can be very small in good dispersions, the dimension of the diameter can be greater than the size reported for not producing distortions of the director. Nevertheless, no trapping was observed in SWCNTs and we can exclude the occurrence of any topological defects at the tube ends, resulting in defect-mediated interactions with the disclination. The claim that no trapping was observed for SWCNTs (Figure 23) is therefore in agreement with the lack of attraction forces owing to no formation of topological defects besides the absence of simple strong nematic distortions in the liquid crystal medium.

3.7.2 Trapping of $Mo_6S_2I_8$ nanowires and MWCNTs

Unlike with SWCNTs, we achieved the trapping of numerous $Mo_6S_2I_8$ nanowires and MWCNTs that further appear like dark threads, which make the disclination lines more apparent, as seen from the polarising optical microscopy images shown in Figure 24. These images were captured a couple of hours after the liquid crystal with dispersed nanoparticles was introduced into the cell.

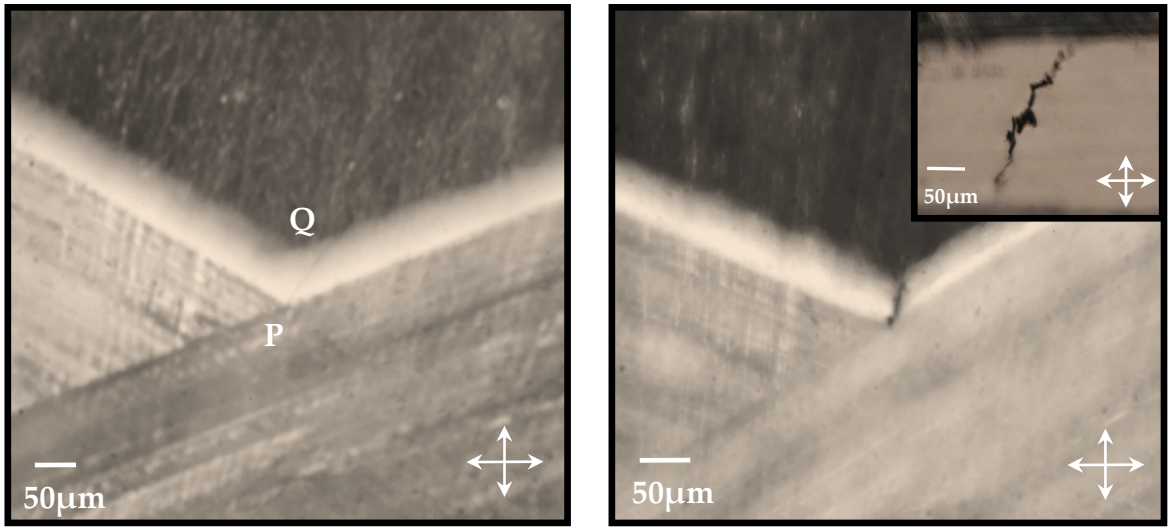

Figure 24: Micrographs of the (a) defect line alone (b) defect line with MWCNTs trapped. Inset shows the defect line with $Mo_6S_2I_8$ nanowires trapped. In both the cases, the two substrates are slightly shifted for better visualization.

Figure 25 is a series of micrographs of aggregates of nanowires (a-c) and MWCNTs (d-f) advancing towards a ½ defect line and eventually trapping on it. In Figure 25 (a-c), the disclination is relatively long and oblique as the glass substrates are shifted apart for better visibility, i.e., the points P and Q are not on top of each other, as seen in Figure 24. However, we only used samples that had a straight short defect line for the trajectory measurements. In general, trapping of nanowire aggregates, as shown in Figure 25(a-c), was more efficient than MWCNTs. We also observed that some of the MWCNTs were not drawn towards the disclination in Figure 25(d-f). This is because the elastic energy of interaction between the MWCNTs and the disclination is lower at larger distances relative to that of a nanowire. This

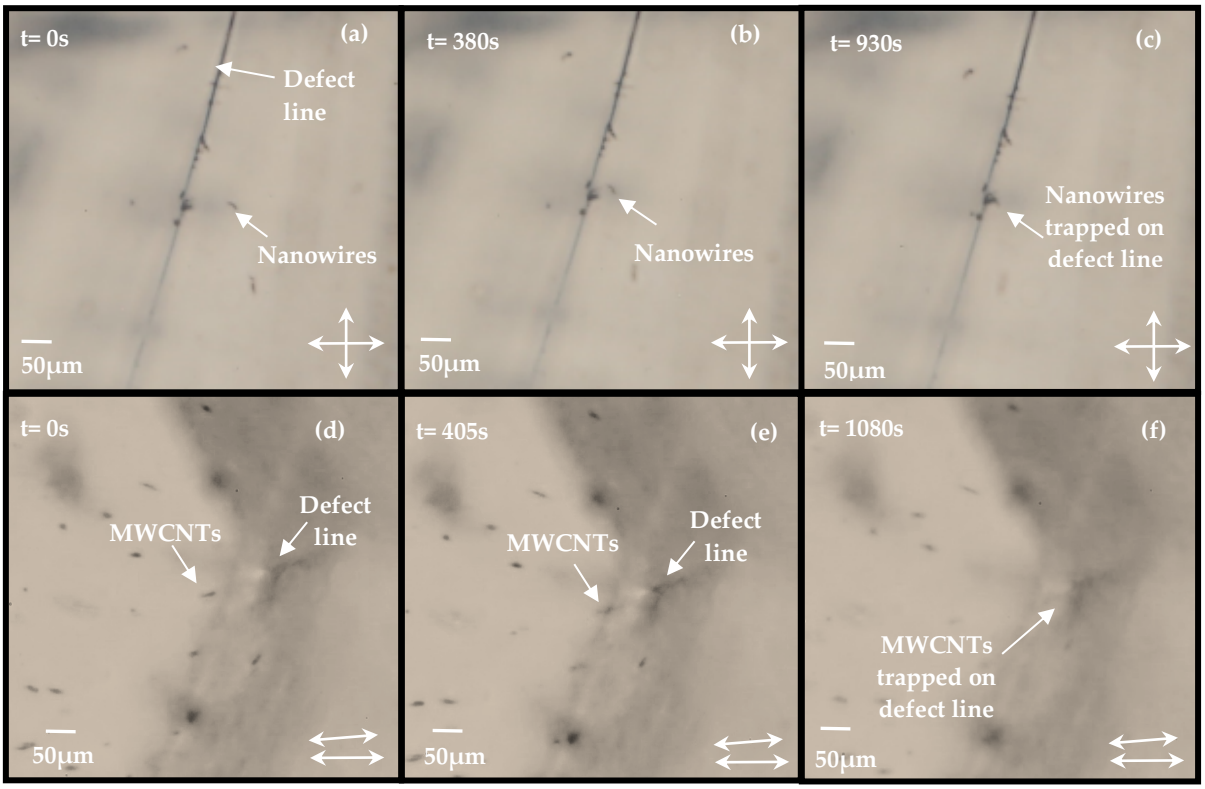

Figure 25: Position of aggregates of (a-c) nanowire observed between crossed polarizers (d-f) MWCNT, here the polarizer & analyser is at an angle of 10° for better observation.

behaviour is observed to be consistent with all the evaluations we performed on different particle trajectories and can be understood by taking into account the difference in the structural morphology of the nanoparticles, which will be elaborated in the following sections.

3.8 Measurement of the nematic force of attraction

The fundamental concept of calculating the interaction between the nanoparticles and the disclination is based on the principle of the balance of forces experienced by the dispersed nanoparticle. When the particles are within the proximity of the disclination, $\boldsymbol{F_{particle-line}}$ the orientation-distortion mediated force arising from the interaction reviewed in Section 3.5 will attract the particles towards the disclination line. Since the particles are moving in a viscous medium, they experience a Stokes' drag force that is proportional to the particle

velocity. In addition, the value of *Ericksen* number $Er = \frac{\eta L v}{K} \sim 10^{-2}$ is small, where $\eta = 0.0525$ Pa·s represents the viscosity of 5CB [136]; $L = \sim 5$ µm the characteristic length scale of the system, here the diameter of the aggregate of the particle; $\boldsymbol{v} = \sim 0.17$ µm·s^{-1} the average velocity of the aggregate, $K = 10^{-11}$ N the elastic constant). Therefore, no viscous coupling between the velocity $\boldsymbol{v}$ and the director $\boldsymbol{n}$, and elastic deformations of the nematic medium in response to the moving nanoparticles are insignificant. Furthermore, since the *Reynolds* number $Re = \frac{\rho v L}{\eta} \sim 10^{-9}$ is also very small, where $\rho = 1.03$ g·cm^{-3}, mass density of 5CB [137], the flow remains laminar around the particle.

Under these conditions, and disregarding vertical motion due to gravity, the motion of the nanoparticles can be projected onto the x and y-axes, described by the plane parallel to the glass substrates. The average velocity of the nanoparticle as a function of its distance r to the disclination is determined from the average trajectory. Since the defect line-particle interaction is a function of distance, the velocity of the nanoparticle increases as it advances towards the defect line. Brownian motion introduces small fluctuations in the motion of the particles during its trajectory as noticeable in Figure 26.

Since they are in a steady regime, the nematic force of attraction can be derived from the balance of forces experienced by the particle, in which the attractive force on the particle is balanced by the viscous force acting on the particle due to Stokes' drag [138]. Thus, the nematic force can be determined at any given time by calculating the Stokes' drag force acting on the particles, which is determined from Stokes' equation for a cylinder moving in a viscous fluid:

$$\boldsymbol{F_{Stokes}} = \frac{2\pi\eta\, L}{ln\left(\frac{L}{2R}\right) + \gamma}\, \boldsymbol{v} = \boldsymbol{F_{nematic}} \qquad (9)$$

where $\boldsymbol{v}$ is the velocity of approach of the particle towards the defect line, $\gamma = -0.114$ [139] is the correction factor and R and L the radius and length of the aggregates of nanoparticles, respectively, considered as cylinders.

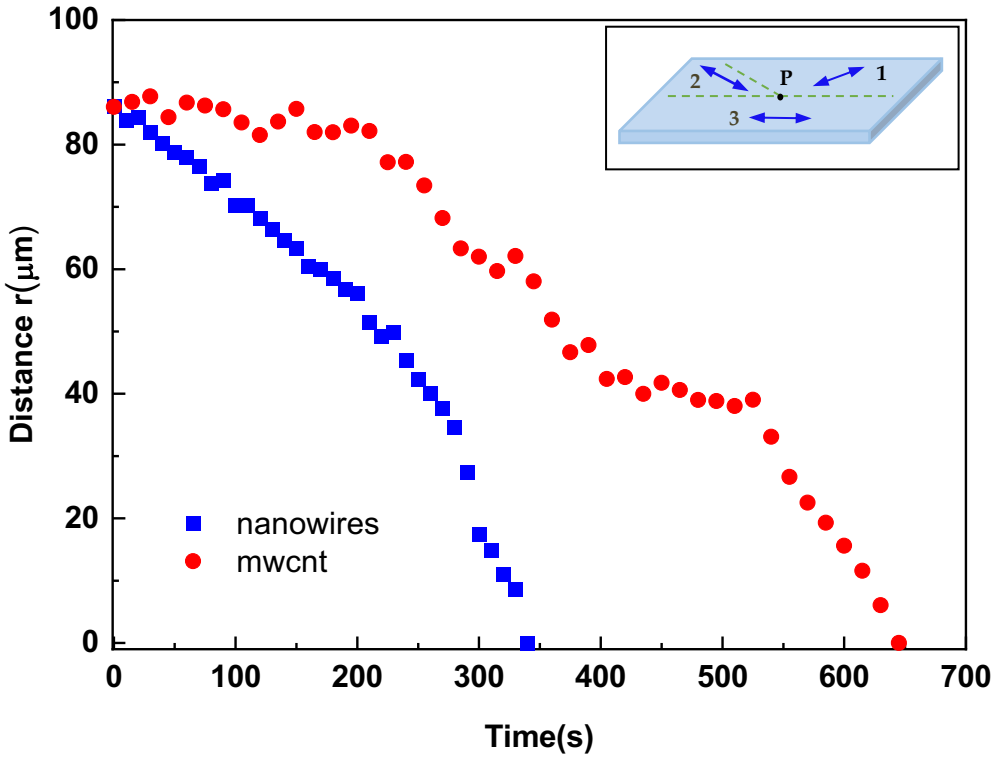

Figure 26: Displacement of the dispersed aggregates of MWCNTs and nanowires towards the defect line as a function of time. In this plot, the area of approach of the nanoparticles to the defect line is three, as indicated in Figure 16, also shown here in the inset.

It is apparent from Figure 26 that, as opposed to nanowires following similar trajectories, multi-walled CNT aggregates take approximately double the time to reach the disclination. However, in contrast to the single-walled CNTs, the multi-walled CNT aggregates ultimately become trapped on the disclination. This indicates that, even though the multi-walled nanotubes are structurally identical to the single-walled nanotubes, there are considerable differences in the alignment of the liquid crystal molecules. Because of their larger diameters, MWCNTs have a comparatively greater number of aromatic rings per unit length than SWCNTs, which provide more surface area [140] for the LC molecules to interact with and, consequently, to anchor. This results in an overall stronger London interaction energy per unit length of nanotubes for multi-walled CNTs with the liquid crystal [135]. Taking into

account that 5CB has reported to show strong anchoring on single-walled CNTs [141], we expect the multi-walled CNTs also to be in the strong anchoring regime. Therefore, multi-walled CNTs should facilitate a stronger planar anchoring on a nanotube compared to single-walled CNTs and, if the nanotubes cause a director deformation, this is more severe for MWCNTs [114].

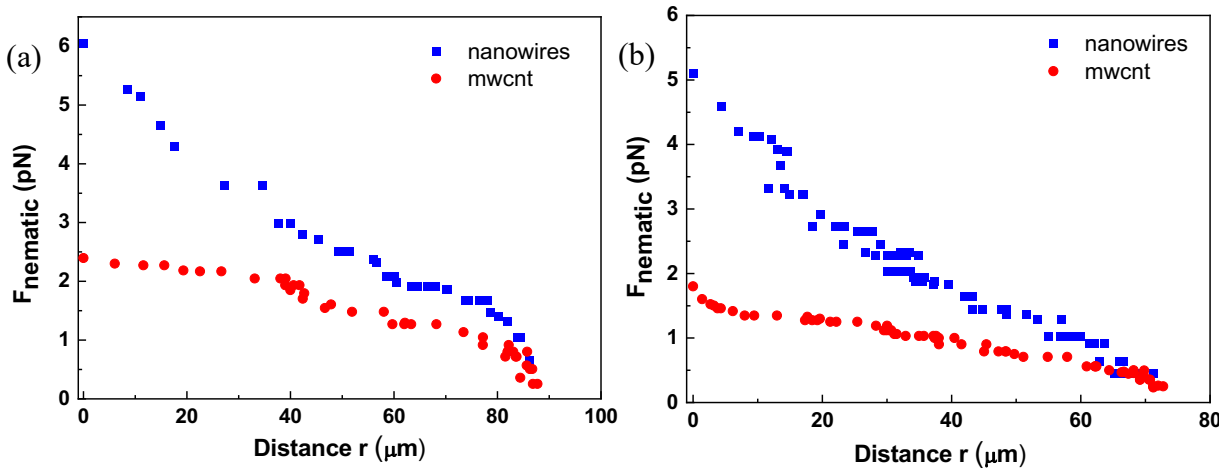

Figure 27: The force on the aggregates of MWCNTs and nanowires in the vicinity of a defect line, plotted as a function of relative separation. Here the areas of approach of the particles are the ones: (a) indicated as three and (b) indicated as one, in Figure 16.

Figure 27 plots the attractive nematic force as a function of the relative separation between the nanoparticles and the disclination line. The aggregates of both the nanoparticles tracked in these plots are selected in a way that they are nearly of the similar size, as judged by the POM micrographs and approach the disclination from similar locations. We used the following dimensions, measured from optical microscopy images, and analysed using ImageJ, for the tracked particle to calculate the attractive force $\boldsymbol{F_{nematic}}$:

- for the particles that approach the defect line from region one, R =2.20 μm and L =23.32 μm for MWCNTs; R =2.89 μm and L =23.64 μm for the nanowires and,
- for particles advancing from region three, R =2.39 μm and L =20.38 μm for MWCNTs; R =3.05 μm and L =19.95 μm for the nanowires [114].

It is evident in these two cases, that the nematic force acting on the nanowires is nearly twice the force exerted on the MWCNTs. Because of the inability to locate the precise position of the particle closer to the defect line due to the distortion around it, let us consider the force up to couple of microns before the defect line. The attractive nematic force acting on the nanowire aggregates at a distance of 10 μm from the defect line is about 4 pN and 5 pN, while that for the MWCNT aggregates is around 1.5 pN and 2.5 pN, respectively. It is worth noting that the observations described here are for aggregates of similar dimensions, but the trend of easier trapping for nanowires compared to CNTs is consistent for aggregates of nanowires of different dimensions [114]. This implies that the overall trapping efficiency of the $Mo_6S_2I_8$ nanowire aggregates does not appear to depend on the particular dimension range stated here but is instead a very general behaviour. We observed similar trends with all the measurements we conducted, and this can be described by taking into account the difference in structural morphology of the nanowires and CNTs.

Though we assume both the nanoparticles to be rigid rods, in reality, only the bundles of $Mo_6S_2I_8$ nanowires are actually rods. The ends of the nanowire bundles are closed and made of the same material and structure as the lateral surfaces. This results in the same alignment at the ends as defined for micro-rods or spheres, resulting in LC defects and nematic forces [114]. CNTs, on the other hand, are hollow structures and both the tube ends, and the wall surfaces therefore do not have the same planar alignment; accordingly, the boundary conditions do not induce strong director distortions and defect formations. There can be air or liquid crystal molecules in the inner part of the tubes, and, in both these instances, the LC molecules at the ends is expected to obey the planar alignment of the LC along the sides, dissimilar to the perpendicular orientation on the contour of the tube ends as seen in the case of a cylinder [114].

Therefore, for nanowires, on one hand, the attractive potential arises from the interaction between the disclination and the system of particle-induced defects, i.e., from the disclination-particle system's free energy minimization. On the other hand, the elastic interaction between the multi-walled CNTs and the defect line can be understood based on the observation that the MWCNTs introduced in the liquid crystal are highly curved bundles

with noticeable kinks, Figure 20. The planar anchoring of the LC molecules along these curved surfaces coupled with the strong bending deformations of the MWCNTs induces overall elastic distortions that are strong enough to allow the multi-walled CNTs to be attracted by the disclination and eventually be trapped onto it in order to minimize the free energy of the liquid crystal [114].

3.9 Conclusions

In this chapter, we have systematically analysed the attraction forces between the defect lines and aggregates of nanoparticles using customized disclinations which were created at a particular location with a specific topological strength using Teflon surface treatments on glass substrates assembled into cells and filled with a room temperature nematic liquid crystal 5CB. The nematic interaction of liquid crystals with CNTs and $Mo_6S_2I_8$ nanowires is fundamentally different in nature, and the source lies in the topological difference between the two shapes. Although the hollow nature of the CNTs has so far been overlooked due to its very high anisotropic ratio, its influence is substantially demonstrated while observing the space-time plots and the derived nematic attractive forces before the trapping.

When rod-shaped nanoparticles with planar surface anchoring conditions are inserted in a well-oriented nematic liquid crystal, these particles reduce the total free energy of the elastically distorted nematic LCs by generating topological defects of opposite sign. Thus, two surface defects of strength -½, compensating for the +1 formed by the rod-shaped nanoparticle, are formed near the interfacial region of the particle. Nematic attractive forces are created to compensate for the distortion and the particle advances towards the +½ defect line.

Single-walled CNTs could not be trapped in these defect lines. Even though the isolated single-walled tubes have a diameter of ~1 nm, smaller than the size considered sufficient for generating the attractive nematic forces, their actual size is larger due to bundling and aggregation of the tubes. In either case, the tubular structure does not allow the creation of topological defects close to the tube ends, they additionally have minimal distortions even when bundled and thermal fluctuations, and Brownian motion are dominant.

The trapping of multi-walled CNT aggregates was relatively slower than that of the $Mo_6S_2I_8$ nanowire aggregates. Consequently, the attraction forces, as seen from the experimental observations, are evidently stronger and of longer range for $Mo_6S_2I_8$ nanowires than for multi-walled CNTs. The tubular shape of the CNTs ensures that the planar alignment is absent at the tube ends, consistent with an alignment parallel to the tube axis and, hence, the LC does not create any topological defects as compensation. Nematic forces due to the director deformation can be generated to align the nanotubes by forcing their orientation along the LC director or from the strongly deformed shape, as is the case here for MWCNTs. In the latter scenario, the deformed director field couples with the distortions generated by the defect line, resulting in an attractive force that allows the trapping of the MWCNTs. This confinement of MWCNTs onto a defect line to create a vertical interconnect could be potentially used for applications as pressure sensitive vertical conductive interconnects.

Chapter 4

Characterization of aligned carbon nanotube sheets in nematic liquid crystal

Overview of the chapter

In this chapter, we lay the groundwork for the Sensor 2 by characterizing the electrical and optical properties of well-aligned carbon nanotube networks drawn from a CNT forest, based on the DC electrical characterization of aligned multi-wall carbon nanotube sheets with distributed electrical contacts, in the presence and absence of LC. We also compare the electrical properties of the aligned MWCNT sheets with those of unaligned MWCNTs. The presented results demonstrate the significance of having aligned CNTs in improving the electrical conductivity and be used for reproducible pressure sensing applications.

4.1 Introduction

Macroscopic structures based on carbon nanotubes (CNTs), such as solid-state spun free-standing sheets and yarns, have been extensively investigated in recent years for their multifunctional properties [142][143][144]. The anisotropic properties of CNTs necessitate the alignment of nanotubes in a particular orientation to translate the mechanical and physical properties of individual nanotubes to the macroscale [145][146]. Well-aligned CNT sheets constitute the initial macroscopic CNT assembly for further scaling, and, for many applications, they have been extensively explored as a host material [20][147].

Bulk CNT ensembles can be fabricated as sheets or yarns using wet or dry methods for large-scale assembly of individual CNTs. The early approach of manufacturing CNT sheets, called the dispersion and filtration technique, was inspired from the ancient art of papermaking. This comprises of dispersion of carbon nanotubes in an aqueous surfactant solution followed by filtration and drying process [148][149]. Further solution-based methods include self-assembly [150], Langmuir–Blodgett technique [151] based on the hydrophobic interactions of the nanotubes, and dip coating method [152][153]. While solution-based/wet methods permit the deposition of nanotube thin films on a wide range of substrates, the undesirable residues on CNTs that require post-treatment processes, such as thermal annealing, make it challenging for large-scale applications. In 2002, Jiang et al. [13] first demonstrated a solid-state technique of spinning of CNT yarns drawn from the sidewall of a vertically aligned array of CNTs formed by chemical vapour deposition (CVD). Zhang et al. [14] further, in 2005, reported that continuous CNT sheets could be pulled from spinnable CNT arrays or forests by "dry spinning". These nanotubes are assembled as a consequence of the van der Waals attractive forces between them. Nevertheless, in current technology, the fixed dimensions of the CNT array restrict the CNT sheet length.

Owing to this approach of aligning CNTs, we were motivated to explore the use of MWCNT sheets embedded in liquid crystals for pressure sensing. LC acts as an excellent functional filler for this application because they are soft, viscoelastic fluids that are highly responsive. Nevertheless, some basic concepts need to be understood, in particular the effects on the electrical properties of CNT sheets when embedded in liquid crystals. This chapter outlines

the electrical and optical characterization of the CNT sheets mechanically drawn from a MWCNT forest. Firstly, their fabrication methods are elaborated, and their relevant electrical and optical properties are then examined.

4.2 Multi-walled CNT forest

Vertically aligned arrays of CNTs, also known as CNT forests, were first synthesized by Li et al. [154]. Since then, CNT forests have attracted much research interest because continuous CNT sheets can be mechanically drawn from spinnable carbon nanotube arrays through van der Waals forces between the CNTs. The multi-walled CNT forest used in our research was purchased from A-Tech System Ltd., Republic of Korea. This drawable CNT array was grown using chemical vapour decomposition (CVD) of acetylene gas on an iron-coated silicon wafer. The average height of the CNT forest is about 350 μm and CNT diameters range from 10 nm (inner) to 20 nm (outer) [69]. When a single layer of MWCNT sheet was mechanically pulled from the forest, bundles of nanotubes could be drawn as shown in Figure 28, primarily aligned in one direction.

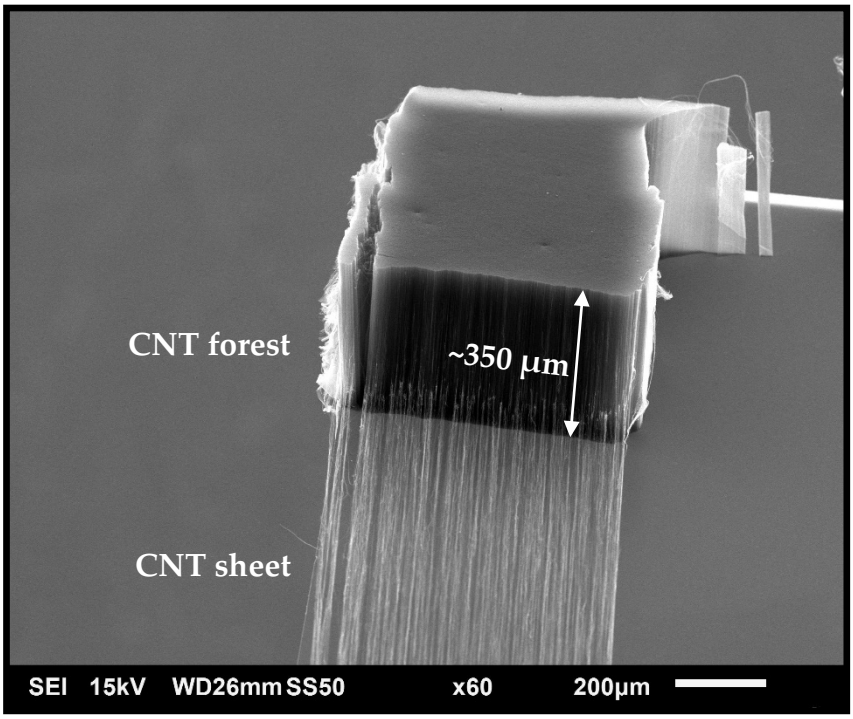

Figure 28: Scanning electron microscopy image of MWCNT sheet drawn from MWCNT forest. (Courtesy: Dr. Hakam Agha)

4.3 Fabrication of substrates with aligned CNT sheets

4.3.1 Substrate preparation and etching process of ITO

The different steps of fabrication of the substrates are as illustrated in Figure 29. The cells were made using bare glass as top substrates and indium tin oxide (ITO) coated glass as lower substrates. Thin strips of ITO electrodes were etched in linear patterns by wet chemical etching using zinc (Zn) powder and concentrated hydrochloric acid (HCl) using Scotch tape as etching mask. Zn powder was dusted on top of the masked ITO substrate and then immersed in 1M HCl solution. The surface resistivity of the ITO layers was 100 Ω/sq.

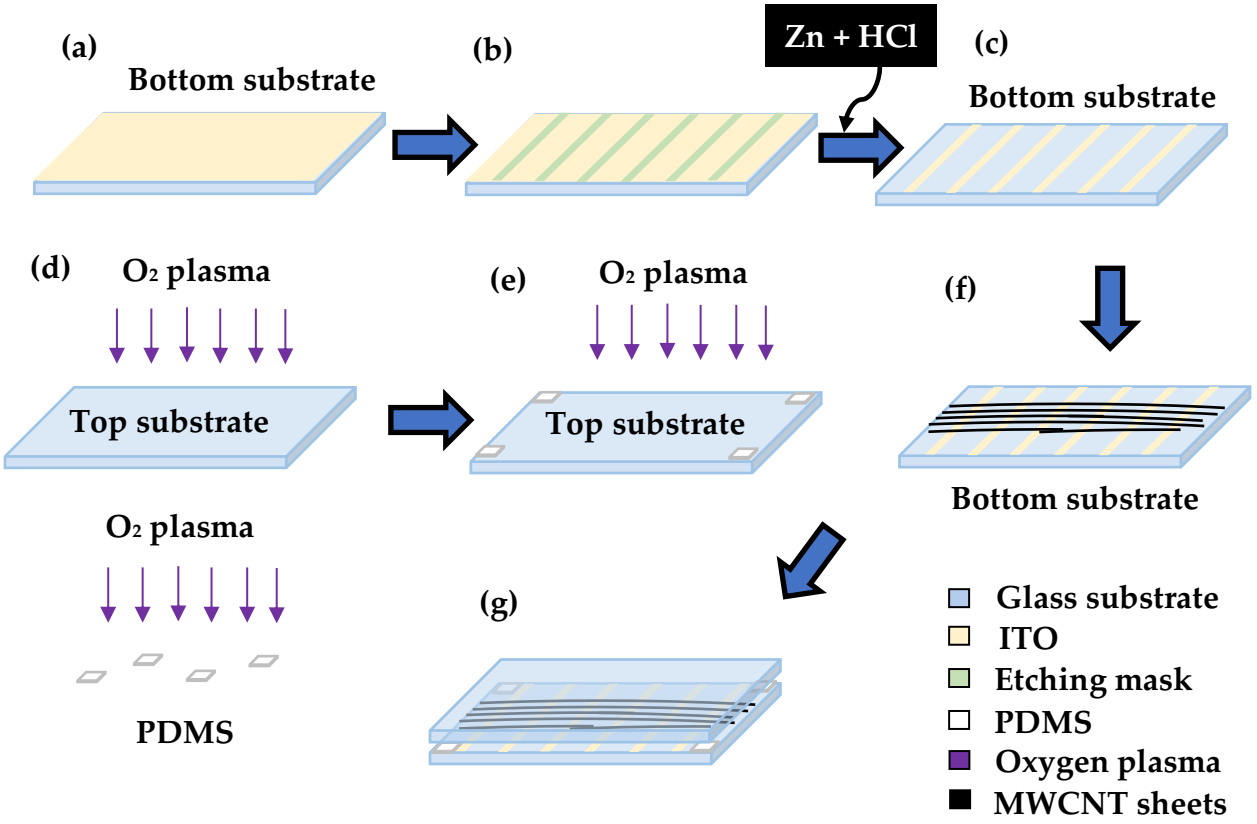

Figure 29: Fabrication of substrates. (a) ITO glass as lower substrate. (b) Patterning of ITO electrodes using Scotch tape. (c) Etching of ITO using Zn+HCl. (d) Oxygen plasma treatment (indicated using violet arrows) on the top substrate and PDMS spacers. (e) Bonding of PDMS onto the top substrate and further oxygen plasma treatment above the bonded PDMS. (f) Deposition of MWCNT sheets on bottom substrate. (g) Assembling the cell by bonding of lower substrate with PDMS on top substrate.

To prepare cells containing liquid crystal, soda-lime glass slides (purchased from DURAN Group, Germany) cut into appropriate sizes were used as top substrates. Both upper and lower substrates are cleaned via a standard procedure of ultrasonication in acetone, followed by isopropanol and then deionized water, respectively, for 15 min in each solvent. Finally, the substrates were dried using an air blowgun followed by dehydration baking on a hot plate for 10 min at 100°C.

The cell thickness was defined using polydimethylsiloxane (PDMS), a cross-linked polymer of thickness 150 μm, as spacers. PDMS (184 Sylgard elastomer kit) was produced by mixing the curing agent and elastomer base in a weight ratio of 1:10, which was then degassed and polymerized in a vacuum oven at 75˚C for 1 hour and left overnight. The top glass substrate and the PDMS spacer were bonded after surface activation using oxygen plasma. On top of the PDMS spacer, surface activation was again performed, and the top glass substrate was bonded to the bottom substrate bearing the deposited MWCNT sheets. The deposition of MWCNT sheets is as elaborated below.

4.3.2 Drawing of CNT sheets from CNT forest

The MWCNT sheets used in our work were pulled from the vertically aligned multi-walled CNT forest/array as shown in Figure 28. In a CNT array, the vertically grown nanotubes on a silicon wafer are aligned parallel to each other. The CNT sheet consists of long, macroscopically well-aligned MWCNT bundles that are held together.

Figure 30 shows the different steps of fabrication of the MWCNT sheets. First, we placed a scalpel blade lightly on the sidewall of the MWCNT array and gradually pulled a continuous layer of MWCNT sheet from the MWCNT array. Afterwards, the nanotube sheet was affixed to capillary glass tubes attached to a homemade rotatable stage. Next, the CNT sheets were further pulled by rotating the stage and were stretched for unidirectional alignment [14]. The number of stacked CNT sheet layers could be increased by multiple rotations of the stage. When these sheets were stacked layer by layer on top of one another, multiple layers of CNT sheets could be formed. The CNT sheets were then placed directly on the required glass substrate.

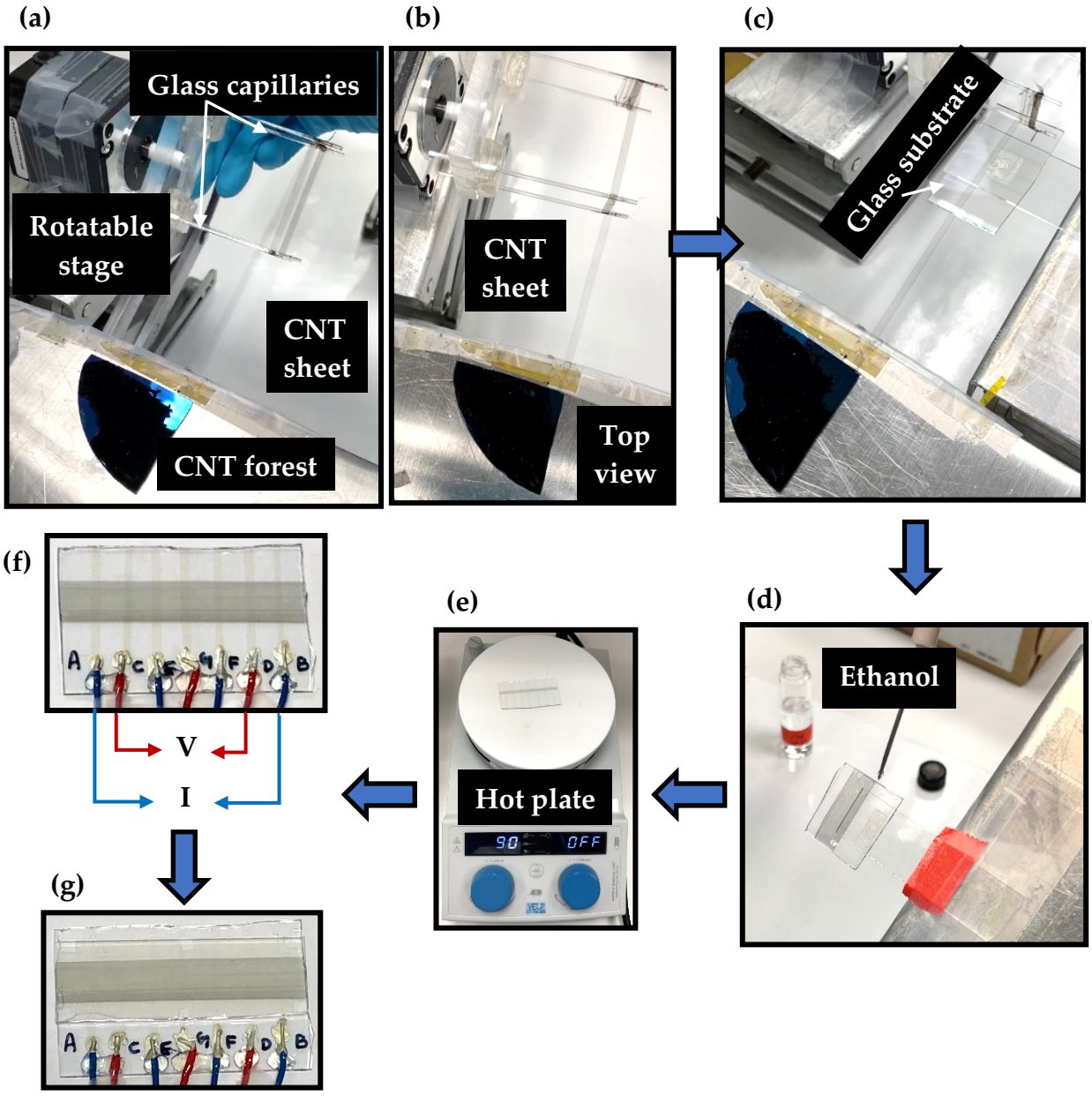

Figure 30: Fabrication of the samples. First step: (a) Pulling of CNT sheets from CNT forest. (b) Top view of freestanding CNT sheet attached to glass capillaries connected to a rotatable stage. Second step: (c) Deposition of CNT sheets onto glass substrates. (d) Adhesion using ethanol. (e) Drying on hot plate. (f) Sample with MWCNT sheets alone with electrical wires and schematic depicting connections in four-wire configuration. (g) Cell of MWCNT with LC introduced in between through capillary filling.

This was followed by densification using a few droplets of ethanol (VWR chemicals, 96%) flowed along the nanotube alignment direction through the glass substrate held at an angle to improve adhesion. The substrate was then dried on a hot plate at 90°C for 15 min. Since each nanotube had a length limit equivalent to the height of the forest (350 μm in our study), this long aligned CNT sheet was composed of numerous nanotubes held together by van der Waals interaction between the nanotubes and, hence, adhesion treatment is necessary. The details of this treatment will be discussed later. Electrical contacts were formed between the ITO electrodes and the connecting wires using a conductive silver paste. The gap between each pair of ITO electrodes is ~5 mm.

Finally, to prepare samples with liquid crystal, a bare glass substrate was placed on top, with spacing maintained using polydimethylsiloxane, and LC is filled in between through capillary filling.

4.4 Two-Wire vs. Four-Wire Configuration: Which resistance measurement technique is relevant for our application?

The electrical properties of the samples were investigated using a source meter (Keithley Model 2450) in two-wire [155] and four-wire configurations [156]. However, these two configurations are not similarly suitable for all applications of resistance measurement. A source meter is a device that can simultaneously source and determine both voltage and current and can be configured to display the resistance. In this chapter, we mostly used the constant-current method to evaluate the resistance, which supplies our sample with a constant current and measures the resistance across the sample.

In two-wire configuration, the same electrical probe that measures the voltage also supplies the current. When applied to low-resistance samples, the primary issue with the two-wire measurement technique is that the total contact resistance is added to the measurement. Since the current applied induces a small, but significant, drop in voltage across the electrical

leads, the voltage measured by the source meter will not be the same as the voltage directly across the sample, and considerable error can result.

The limitation of the two-wire method can be rectified by separating the roles of the probes, such that the current is sourced by one pair of probes and the voltage is determined by another pair [157]. This method is called the four-wire technique and is used for low resistance measurements to minimize the effect of contact resistance. With this configuration, the probes are spaced inline, with the outer two probes inducing a set current through the sample and the inner two probes measuring the voltage drop across the surface of the sample, as shown in the Figure 30(g).

To evaluate which configuration made sense for our application, we measured the resistances in both two-wire and four-wire configurations across different lengths of sample with a single layer of MWCNT sheet.

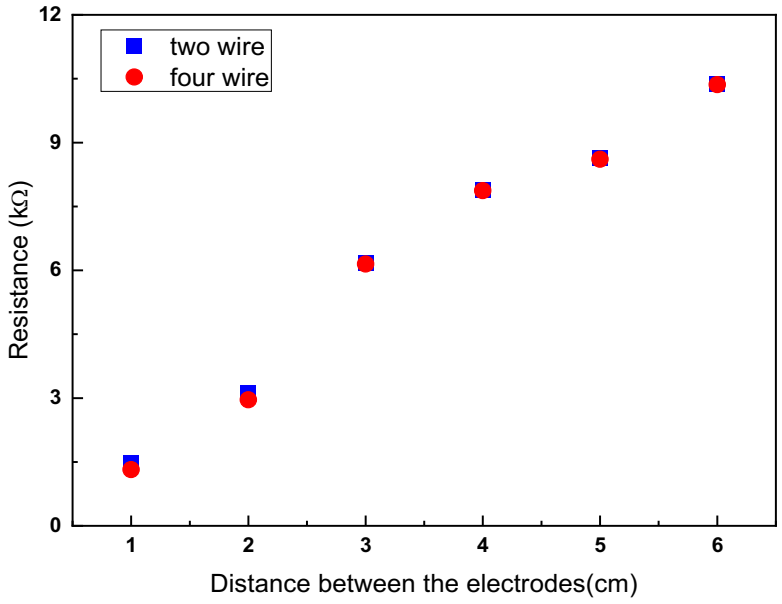

Figure 31: Plot showing the comparison between two-wire and four-wire measurements of MWCNT sheets for electrode distances > 3 cm.

We observe that, for electrode distances (or MWCNT sheet lengths) greater than ~3 cm, four-probe measurements gave similar results to those acquired by two-probe measurements (difference ~20 Ω), as seen in Figure 31. This reveals that the contact resistances of the electrodes are insignificant compared to the resistance of the CNT sheets for distances greater than 3 cm.

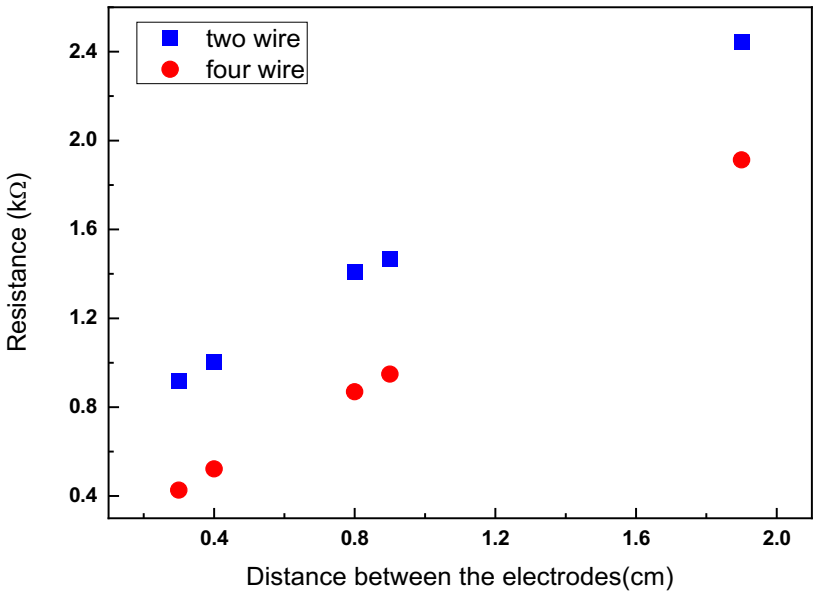

Figure 32: Plot showing the comparison between two-wire and four-wire measurements of MWCNT sheets for electrode distances < 3 cm.

In contrast, for distances less than ~3 cm, we observed a notable difference of up to 1 kΩ in the values of measurements between two-wire and four-wire measurements, as seen in Figure 32, clearly indicating the influence of contact resistance in the system. Thus, we can conclude that the four-wire configuration is best suited for our samples, as most of the sample lengths were less than 3 cm.

4.5 Adhesion of CNT sheet on the glass substrate

When MWCNT sheets are deposited onto the glass substrate, one critical aspect that needs to be addressed is the deposited layer not being completely adhered to the surface of the substrate. This leads to a lack of uniformity, with some nanotube fibres dangling from the substrate, which can also become more susceptible to the flow of the liquid crystal during the filling of the cell. The effect of CNT orientation and alignment on the electrical conductivity has already been investigated in the literature [158][159] and highlights their direct relationship. Therefore, we used a volatile solvent, ethanol, to improve the adhesion [160]. Droplets of ethanol were flowed along the nanotube alignment direction through the glass substrate held at an angle, as shown in Figure 30(d). The substrate was then dried on a hot plate at 90°C for 15 min. The capillary bridges generated between the tubes and the substrate surface pull the wavy CNT fibres to the surface during evaporation. This flattens the tubes to the substrate and enables the coherence of MWCNTs and their adhesion to the substrate due to the increase in contact area between the nanotubes and the substrate.

4.5.1 Effect of ethanol treatment on resistance of CNT sheet

We examined the resistance values of the MWCNT sheet before and after the ethanol treatment. However, as seen in Figure 33, this treatment affected the resistance measurements of the MWCNT sheet, as shown in Table 1.

Table 1: Comparison of the resistance values of bare MWCNT sheet before and after ethanol treatment.

Distance between electrodes (cm)	Resistance (kΩ) of MWCNT (before ethanol treatment)	Resistance (kΩ) of MWCNT (after ethanol treatment)
5	5.78	5.91
3	3.24	3.32
1	1.23	1.25

It was observed that the resistance values increased, though not significantly, and this increase could be attributed to an increase in disorder of the nanotubes [161]. This can modify the electronic structure of the nanotube and, in turn, its electrical transport properties. Thus, though the ethanol treatment improved the adhesion of the CNT sheets, the offset is the slight increase in resistance. It is also worth noting that, for smaller electrode distances, the increase in resistance is only ~20 Ω.

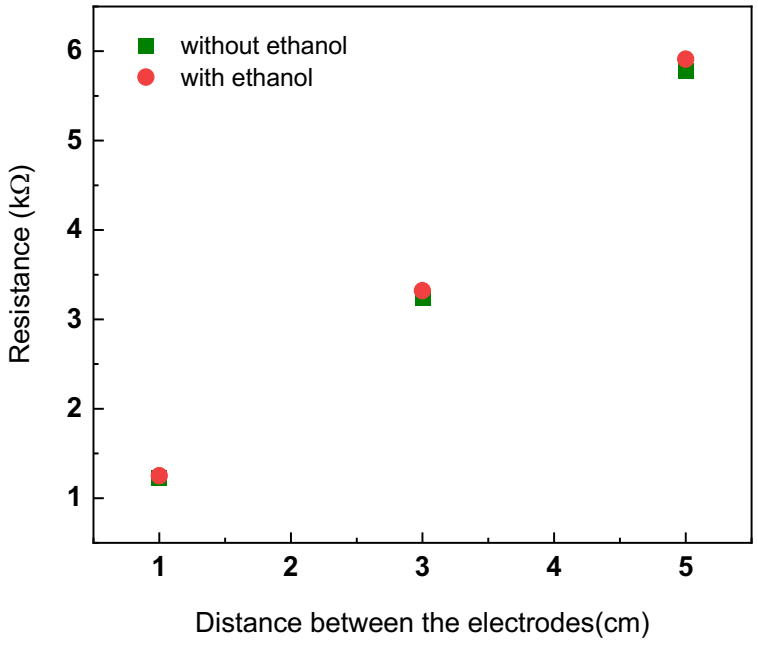

Figure 33: Plot showing the change in resistance as a function of the distance between the electrodes before and after ethanol treatments.

4.6 Cells of LC with aligned MWCNT sheets

Cells were made by sandwiching a bare glass slide as the top substrate and MWCNT sheets deposited on etched ITO substrate as bottom one, as shown in Figure 34. Four rectangular-shaped PDMS fragments of dimensions ~2.5 mm × 1.5 mm were used as spacers. A nematic liquid crystal, 5CB was introduced between the cells via capillary action. We chose 5CB as

the LC matrix as it exists in the nematic phase at normal room temperatures and therefore does not require further treatments to maintain the liquid crystal phase. The cell thickness was maintained using PDMS as spacers (~150 μm).

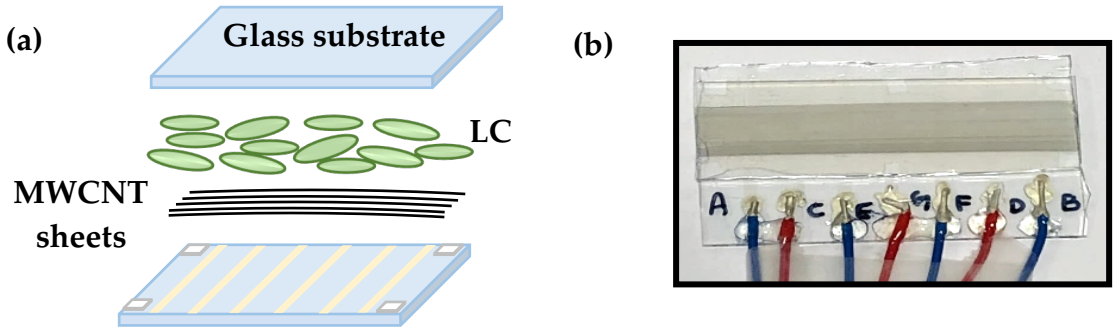

Figure 34: (a): Schematic of the MWCNT+LC cell. (b): Fabricated cell with filled LC.

4.7 Optical characterization of aligned CNT sheets

Optical characterization provides information on how the presence of liquid crystal affects the orientation of the aligned CNT sheets and, consequently, the electrical transport. Transmission studies demonstrate the variance of the transparency of the CNT sheets with the increasing number of sheet layers.

4.7.1 Orientational order of aligned MWCNT sheets

We followed the method typically used to estimate the nematic order parameter of liquid crystals in a planar-aligned cell to determine the degree of alignment of the MWCNT sheets. The nematic orientational order parameter for a 3D system in a nematic LC is defined based on the average of the second Legendre polynomial, as already seen in Eq. (1). Since the CNTs are ethanol-treated and well-aligned on the glass substrates, resulting in the two-dimensional confinement of the nanotubes, the role of CNTs projecting out of the plane can be disregarded in the calculation of the order parameter and the equation becomes [162]:

$$S = \langle\, 2\cos^2\theta - 1 \,\rangle \tag{10}$$

The absorption anisotropy can be used to estimate the orientational order parameter of the CNT sheets [163]. For anisotropic-shaped absorbing molecules, the order parameter is quantified by the molecular transition dipole moment [164] and represented in terms of absorbance parallel ($A_{\parallel}$) and perpendicular ($A_{\perp}$) to the long axis as, for 3D systems:

$$S = \frac{A_{\parallel} - A_{\perp}}{A_{\parallel} + 2A_{\perp}} \tag{11}$$

and for 2D systems [165]:

$$S = \frac{A_{\parallel} - A_{\perp}}{A_{\parallel} + A_{\perp}} \tag{12}$$

Hence, the degree of orientation of the aligned MWCNT sheet was calculated using the two-dimensional order parameter (S) defined by Eq. (12). To explore the influence of LCs on the alignment of CNTs, a polarizing optical microscope connected with a local spectrophotometer (Avantes AvaSpec-2048) was used to analyse the absorbance of CNTs in the presence and absence of LC. We used a LED light source for illumination (CoolLED pE-4000). The intensity of absorbance in the spectra with incident light polarized parallel ($A_{\parallel}$, along with the CNT length; maximum absorption) or perpendicular ($A_{\perp}$; minimum absorption) to the CNT length was observed and used to determine the orientational order parameter of the CNTs.

For each cell, a background correction was performed using a bare glass substrate for the case of CNT alone and the LC in isotropic state sandwiched between the glass substrates for MWCNT+LC samples. Absorbance measurements for the MWCNT+LC samples were performed in the isotropic phase due to the lack of proper extinction of light in the nematic phase as a result of the absence of an alignment layer on the top glass substrate, as shown in

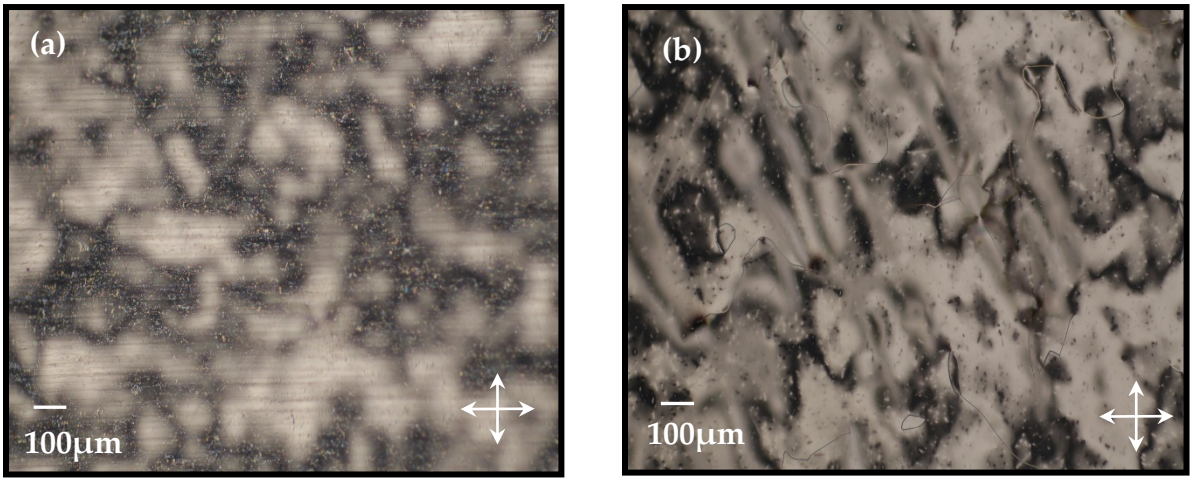

Figure 35: Polarising optical microscopy images of (a) MWCNT+LC sample in nematic phase; (b) An area of the same sample with LC alone in nematic phase.

Figure 35. This also affected the background corrections. Absorbance of each cell was measured with the CNT tube axis parallel and perpendicular to the direction of propagation of light. Orientation was varied by rotating the cell about the axis perpendicular to the plane of the cell.

Figure 36 and Figure 37 show the absorbance spectra of the CNT sheet in the absence and presence of LC respectively. The order parameter of the CNT sheet alone (at a wavelength of 520 nm, arbitrarily chosen) was measured to be 0.45, which was reduced to 0.33 in the presence of LC. This thus indicates that the presence of LC disturbs the alignment of the CNTs. This can be due to the shifting of the tubes while the LC is filled via capillary action, which, in turn, disturbs the alignment of the nanotubes. The influence of this shifting on the electrical properties will be detailed in the subsequent sections.

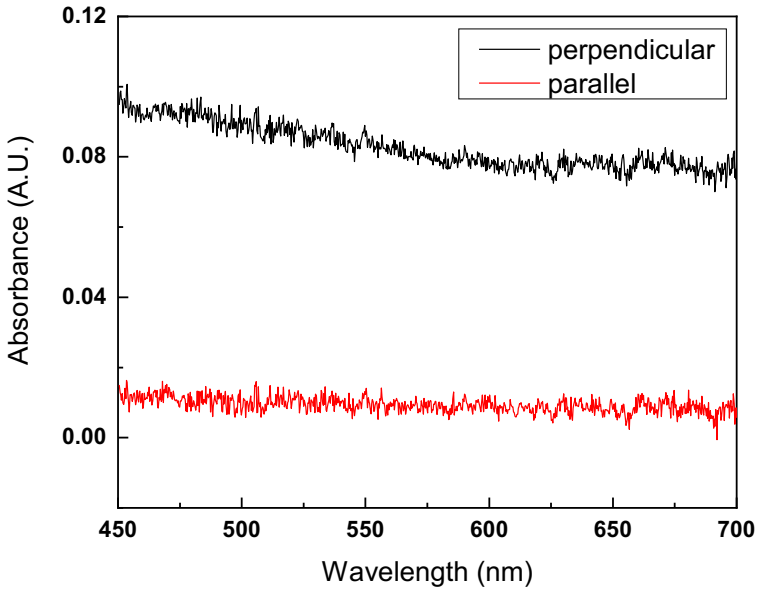

Figure 36: The absorbance spectrum for the sample with MWCNT sheets alone in the visible spectrum with the MWCNT sheets parallel and perpendicular to the tube axis of MWCNTs. The calculated order parameter is 0.45.

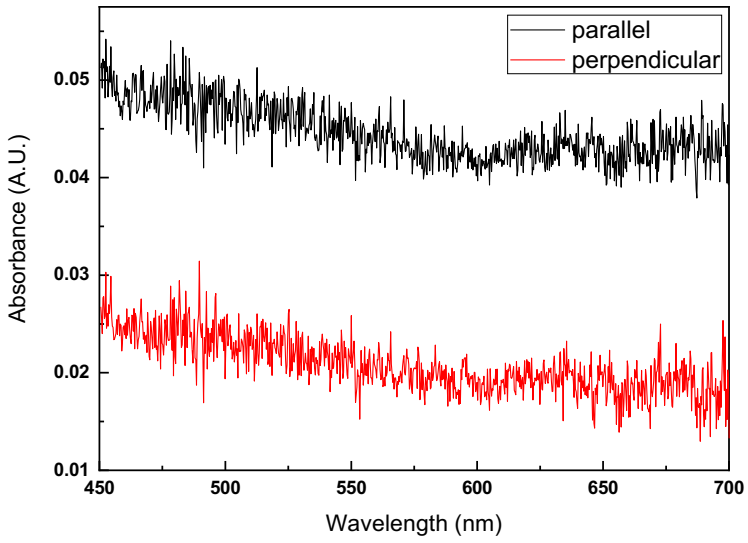

Figure 37: The absorbance spectrum for the sample with MWCNT sheet + LC in the visible spectrum with the MWCNT sheets parallel and perpendicular to the tube axis of MWCNTs. The calculated order parameter is 0.33.

4.7.2 Transmittance of multiple layers of CNT sheets

Multiple layers of CNT sheets can be formed when the sheets are stacked layer by layer on top of each other, thus varying the thickness of the MWCNT sheets. The absorbance of CNTs is an additive property, which implies it depends on the number of sheets that are stacked above each other. We observed that as the number of sheets increase, the transmission decreases. The transparency of the sheets decreased from 85% to 59% when one to four layers were deposited, Figure 38. Accordingly, we consider that, by placing a layer above another, the nanotubes, instead of lying on top of one another, seem to be between the CNT fibres (thereby decreasing the voids also because of the knocking-down motion during the deposition of the CNT sheets).

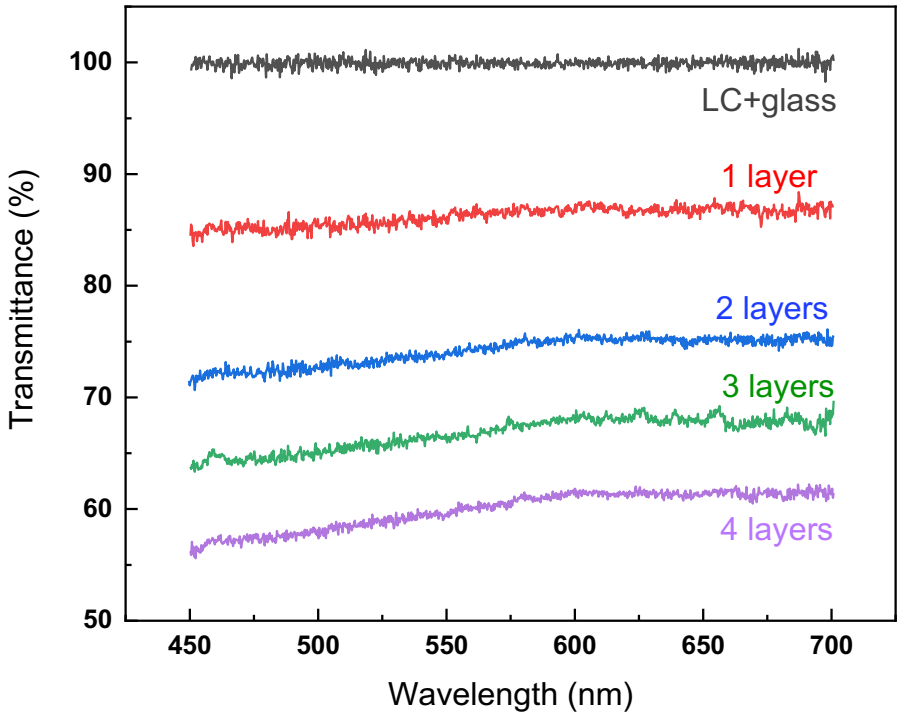

Figure 38: Optical transmittance of the MWCNT sheet + LC in the visible spectra as a function of number of MWCNT sheet layers, where the thickness of CNT film increases with an increase in the number of CNT sheet layers. The reference is glass+LC in isotropic phase.

4.8 Electrical transport properties of CNT sheets

The electrical transport of single nanotubes has been widely reported with regard to experimental and theoretical aspects that have been described by the phenomena of disorder and localization [8][166]. Electrical transport over macroscopic carbon nanotubes (such as films/sheets, yarns, bundles and networks) can be analysed in terms of charge conduction across individual nanotubes, which can be explained in terms of the diffusion of valence electrons through overlapping π electron clouds [167] and conduction between nanotubes by the hopping or tunnelling [168] of the charge carriers. The micro- and macroscale morphologies, besides the defects on nanotubes, could additionally influence the electrical properties [146]. In this section, we report the I-V characteristics of the CNT sheets and the electrical resistance measurements of aligned MWCNT sheets and unaligned networks of drop-cast MWCNTs, both in the presence and absence of LC. The effect of alignment on the electrical transport of CNTs is thus experimentally examined.

4.8.1 I-V characteristics of a single layer of CNT sheet

The current was swept across a range of values and the resistance calculated using Ohm's law from the slope of the resulting line. Figure 39 shows the current-voltage characteristics of the MWCNT sheets in the presence and absence of liquid crystals. The applied voltage ranged from -18 V to 18 V in 0.5 V steps for MWCNT sheets alone and -17 V to 17 V in 0.5 V steps for MWCNT sheets embedded in LC. The I-V data displayed ohmic behaviour, i.e., the current increased as the applied voltage was increased. For the MWCNT sheets alone, when the current is within ± 10 mA the I-V plot is linear, which shows that the MWCNT is metallic with a resistance of 1.88 kΩ. The hysteresis level in the response was also investigated: we saw that there was negligible hysteresis in the resistance measurements.

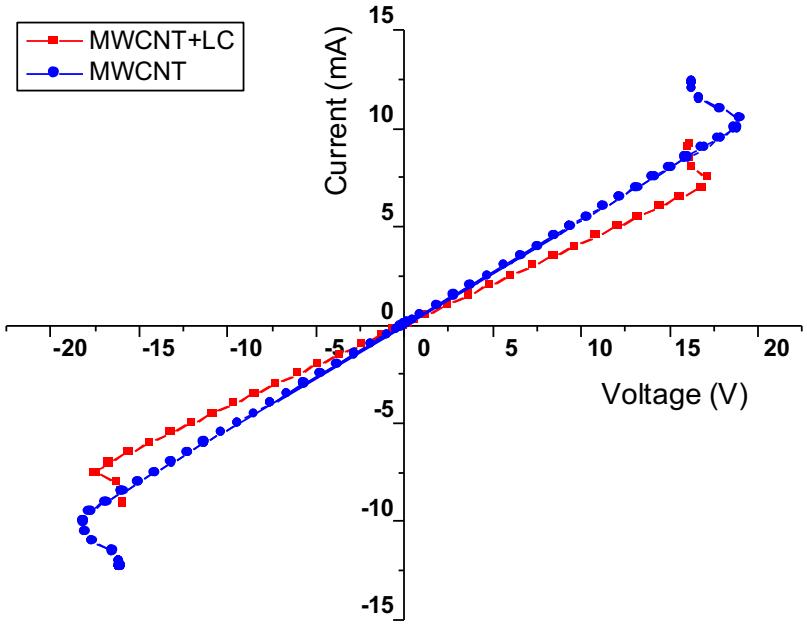

Figure 39: Current-voltage characteristics for different values of I applied through outer terminals; measured the corresponding V across an inner terminal; blue denotes MWCNT sheets alone, resistance: 1.88kΩ; and red MWCNT sheets with LC, resistance: 2.4kΩ

4.8.2 Characteristics of aligned MWCNT sheets pulled from CNT forest

One layer of MWCNT sheet pulled from the MWCNT forest is comprised of several interconnected nanotubes, aligned in the direction of pulling. In order to investigate the role of tube–tube interconnections and the effect of LC on the electrical transport in CNT sheets, we measured the electrical resistance of the sheets in the presence and absence of LC for varying electrode distances. By reducing the electrode distance and thereby the length of the MWCNT sheet, we decreased the number of inter-tube connections.

For bare MWCNT sheets, as the MWCNT sheet is exposed to air, the presence of oxygen increases the carrier-hole density in the MWCNTs through electron transfer from the MWCNTs to oxygen. Consequently, the resistance is comparatively lower. This result is consistent with that observed by Collins et.al [169].

Electrical resistance data confirm the existence of strong interactions between nanotubes and the liquid crystal matrix (Figure 40). It was observed that the CNT resistance is length-dependent and demonstrates that LCs can affect the electrical response of embedded CNT networks. The electrical resistance in the presence of LC shows a noticeable increase (as compared to the bare MWCNT sheets) already at very low MWCNT sheet lengths (3 mm).

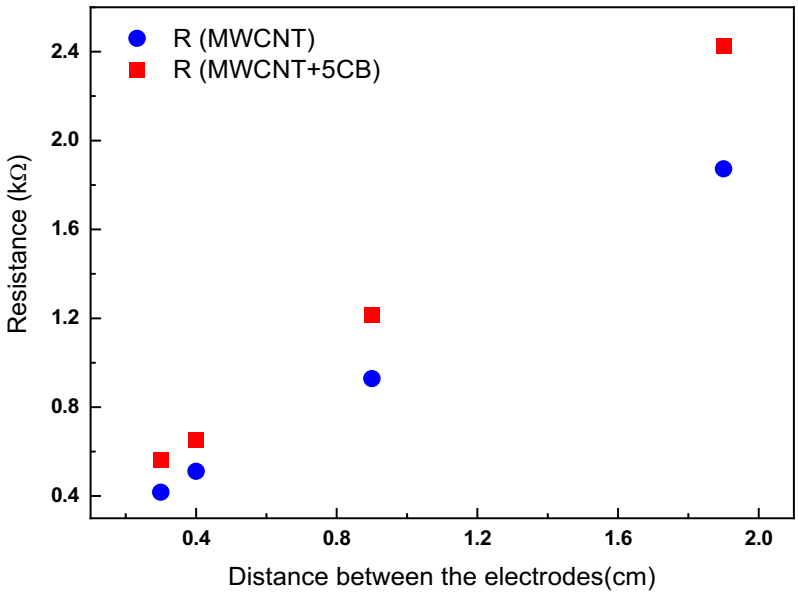

Figure 40: Plot for constant current (I=1mA) applied in four-wire configuration through outer electrodes and resistance measured as a function of MWCNT sheet length, i.e., distance between the electrodes.

When LCs cover CNTs, we infer the increase of resistance observed is due to the interactions between the LC matrix and MWCNTs at the CNT-LC interface that disrupt the continuous path for electron transfer. This increase is due to the strong interfacial coupling between the nanotube surface and the aromatic core structure of 5CB via π- π interactions [170], which facilitates the transfer of electronic density between the CNTs and LC. In addition, we observed that the presence of LC disturbs the alignment of the CNTs (Section 4.7). This

disturbance of the orientation can cause an interruption in the conductive pathway of the CNTs, thereby leading to an increase in resistance in the presence of LC.

Further, at larger distances, the length of the CNT may be smaller than the electrode distance: consequently, this results in more tube-tube interconnections and the CNT junction resistance is therefore more dominant. From Figure 40, we observe that, as the electrode distance increases, there is a larger difference between the resistances of the two systems, possibly denoting the alignment being disturbed over a larger distance and the LC matrix disturbing the possible electron hopping. Thus, the presence of LC decreases the number of inter-tube connections and increases the energy barrier required for the electrical transport between the inter-tube junctions.

4.8.3 Characteristics of drop-cast MWCNT film

Multi-walled carbon nanotubes (0.1wt %) of length 5 μm–15 μm and outer diameter 60 nm–100 nm (purchased from SES Research Inc.) were dispersed in dichloromethane using pulsed ultrasound with a probe ultrasonicator (Hielscher UP200St) for 70 min. The dispersion was then deposited on etched ITO substrates by drop-casting as shown in Figure 41, and the solvent was then left to evaporate for several hours to ensure no residual solvent was left inside. The formed MWCNT film adheres to the substrate owing to the van der Waals forces and a 'coffee ring effect' is observed because of the differential evaporation rates of the solvent. Electrical resistance measurements for varying electrode distances were carried out on this sample as well.

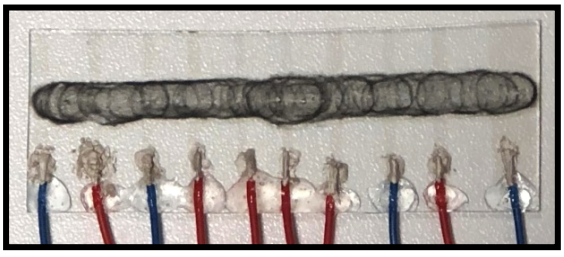

Figure 41: Sample having dispersed MWCNTs drop-cast on etched ITO substrate

Here, the MWCNTs in the network are disordered with poor uniformity and the thickness of the CNT film dependant on the nanotube concentration. Since the CNTs are randomly oriented, the resistance is much higher as the contact resistance of the CNTs strongly depends on how the nanotubes are oriented (if the tubes are parallel, i.e., oriented end-end, or perpendicular, i.e., crossed) at the contact region. Small displacements of the tubes from the end-end configuration can lead to dramatic increases in the resistance [91]. It was observed that the resistance values of the deposited MWCNTs were approximately two orders of magnitude higher than those observed in the case of the aligned MWCNT sheets, denoting an increased contact resistance as well as a probable hopping or tunneling mechanism of electrical conduction due to the CNTs being disordered.

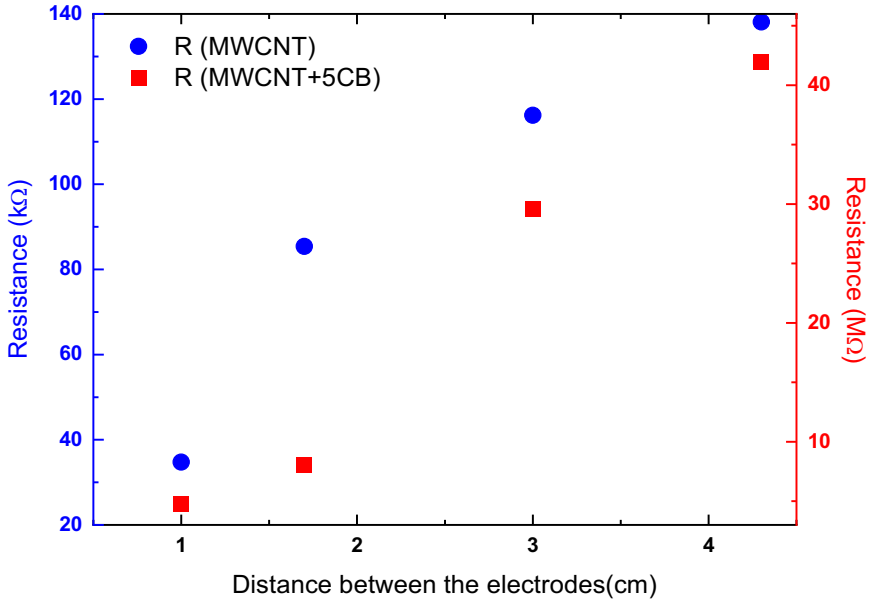

Figure 42: Plot for constant current (I=1mA) applied through outer electrodes and resistance measured as a function of distance between the electrodes for MWCNT deposited via drop-casting.

In the presence of the liquid crystal 5CB, the resistance is even much higher, in the order of MΩ, as in Figure 42. The presence of LC further worsens the orientation of one tube with respect to the other, resulting in no proper pathway for electron transport and thus, a larger contact resistance. In addition, electron hopping (tunneling) between the neighbouring

CNTs is interrupted by the presence of 5CB. These high values of resistances further reinforce the importance of having a well-aligned CNT network for practical purposes. Moreover, their lack of homogeneity is detrimental in realising pressure sensors that are reproducible.

4.8.4 Electrical resistance of multiple layers of CNT sheets

The resistances of multiple layers of CNT sheets embedded in an LC were measured and compared. As shown in Figure 43, the electrical resistance of the CNT sheets, both in the presence and absence of LC, decreased as the number of sheet layers increased, indicating the further conductive pathways formed by the overlapping nanotube layers. The resultant resistances for MWCNT sheets alone varied from 2.96 kΩ to 0.77 kΩ, whereas those for MWCNT+LC ranged from 4.3 kΩ to 0.82 kΩ. This could also be accounted for the fact that the increase in the number of CNT layers leads to an increase in the cross section of the CNT film, which, in turn, results in a reduction in the resistance of the CNT film.

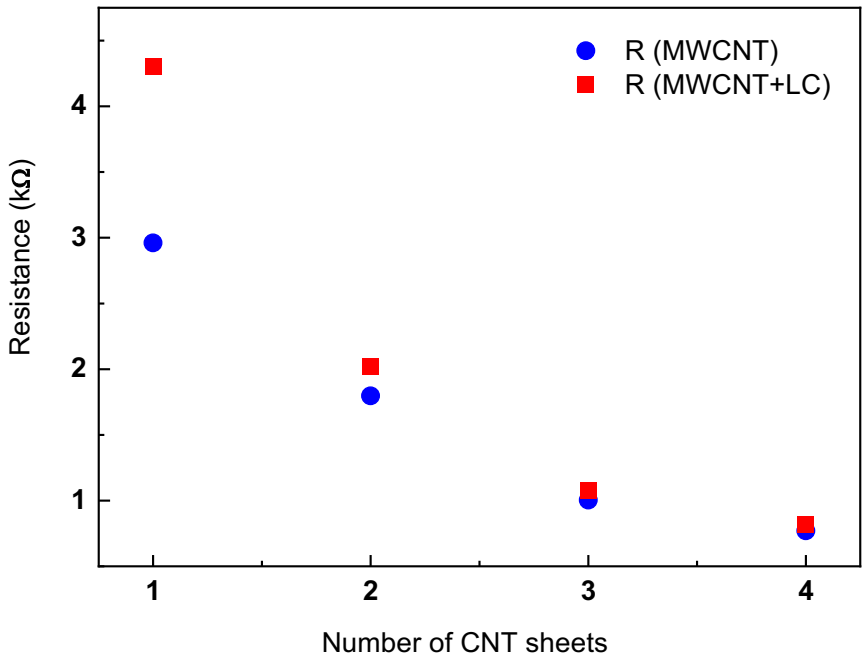

Figure 43: Electrical resistances of the MWCNT sheet +LC as a function of the number of layers.

4.8.5 Temperature dependence of electrical resistance

We have systematically evaluated the temperature effects on the resistance of MWCNT sheets within our working range of temperatures. Generally, regardless of the metallic origin of individual MWCNTs, neither of the macroscopic MWCNT assemblies display a positive resistance temperature coefficient [171]. Accordingly, the decrease in resistivity at higher temperatures is typical for MWCNTs [8][166] and has been associated with the effects of electron interaction and interference [172]. This is consistent with our observations in Figure 44. However, the decrease of resistance per degree rise in temperature is only 1.6 Ω/˚C for a sample with MWCNT sheets alone.

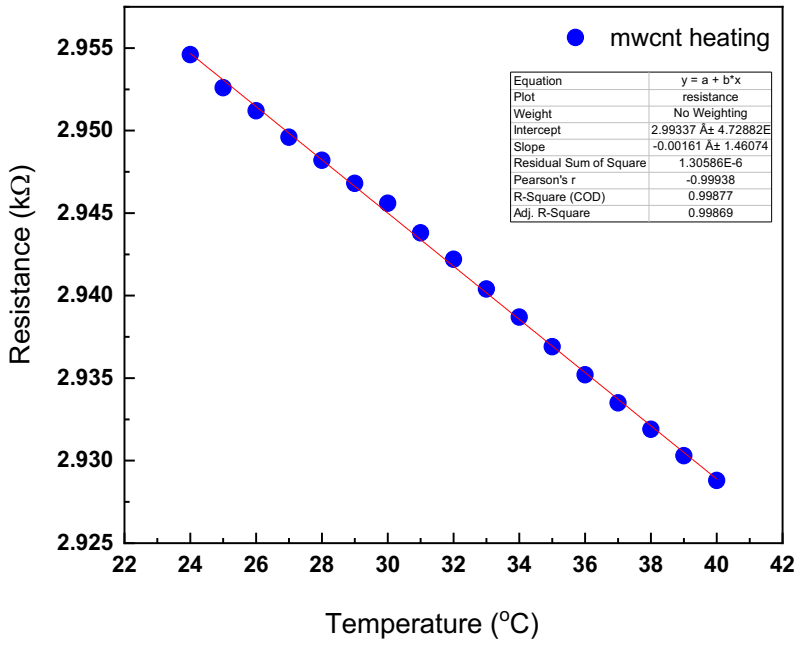

Figure 44: Temperature dependence of the electrical resistance in a sample of MWCNT alone for different temperatures below the isotropic transition temperature of 5CB liquid crystal.

To determine the effect of temperature on the resistances of MWCNT+LC system, the thermal response of the MWCNT+LC sample was studied where the electrical response was measured by monitoring the change in electrical resistance of the sample in a temperature

range from 24˚C to a couple of degrees above the nematic to isotropic transition temperature (T_{N-I}: 35.5˚C) of 5CB, as shown in Figure 45. The temperature of the sample was increased from room temperature to 40°C and then cooled using a hot stage (Linkam UK) at a rate of 2˚C/min and the resistance values were measured at different temperatures from the isotropic phase. In the MWCNT+LC system, we observed the decrease of resistance per degree rise in temperature to be ~4 Ω/˚C. Nevertheless, this is still a negligible variation.

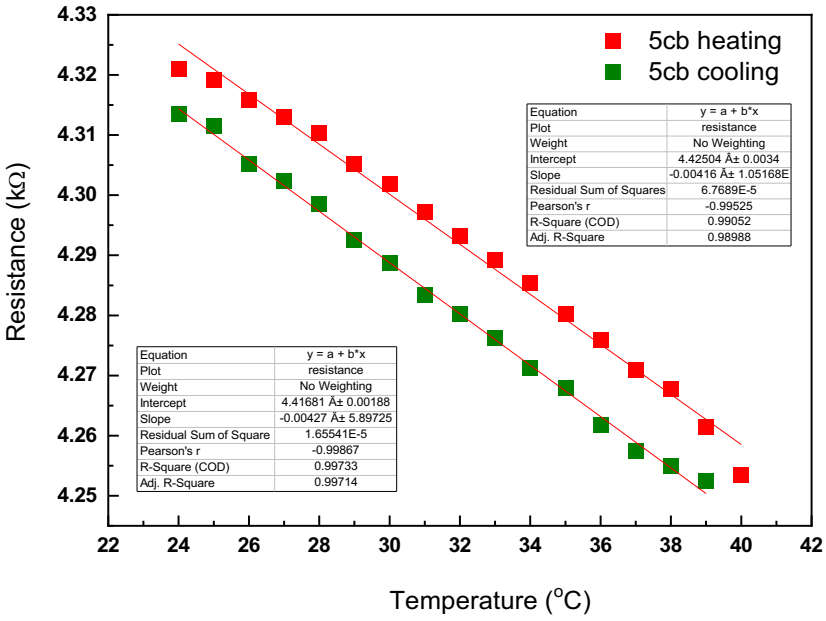

Figure 45: Temperature dependence of the electrical resistance in a sample of MWCNT+5CB for different temperatures below the isotropic transition temperature of 5CB liquid crystal.

The resistance of CNT sheets when LC is isotropic was measured to assess the effect of thermal fluctuations and that for different temperatures in the nematic phase was measured for evaluating the existence of any effect of changes in the dielectric constant. Since the temperature effects are negligible, we can disregard the existence of such effects. The temperature coefficient of resistance (TCR), a quantity used to describe the resistance stability of a material with temperature changes, and the thermal hysteresis were calculated using the following relations:

$$\text{TCR} = \frac{\Delta R}{R_0 \, \Delta T} \tag{13}$$

$$\text{Thermal Hysteresis (\%)} = \frac{R_H - R_C}{R_H} * 100\% \tag{14}$$

where R_0 = the reference resistance of the sample at 25˚C; ΔR = the resistance changes of the sample with respect to R_0 ; ΔT = the change in temperature; R_H = resistance at a particular temperature while heating; and R_C = resistance at the same temperature while cooling.

It was observed that the MWCNT sheet in the presence and absence of LC exhibits decreasing resistance with increasing temperature. This could be associated to the thermal excitation of electrons into conduction band of the nanotubes, which can thus overcome the potential barrier more easily thereby causing an increased mobility of electrons. However, this effect is not significant: the thermal hysteresis value at 30˚C is calculated as 0.3%. Thus, we note that there is not a drastic change of resistance with changing temperature conditions, reflecting no substantial effects induced by the thermal fluctuations nor any influence of dielectric constant of LC molecules. The temperature coefficient of resistance for MWCNT+5CB is about -0.0009/˚C. The low TCR value indicates our system to be temperature invariant within our working range of temperatures. Hence, the temperature effects on the resistance of MWCNT networks can be neglected.

4.9 Conclusions

In this chapter, we have reported the fabrication and electrical properties of dry-spun CNT sheets in the presence and absence of LC. Multi-walled CNT sheets were mechanically drawn from a CNT array using our home-built set up. For MWCNT samples with larger electrode distances (>3 cm), it was observed that the measurements obtained via two-wire and four-wire configurations were not substantially different (~20 Ω), whereas, for smaller electrode

distances (<3 cm), there was a difference of up to 1 kΩ between the two measurement techniques. Hence, four-wire configuration measurements were more reliable for smaller electrode distances as it eliminated the lead resistances. For larger distances, the lead resistance was negligible. Accordingly, the resistance was further measured only using the four-wire configuration.

The orientational order parameter of MWCNT sheets was also determined to analyse the impact of liquid crystal on the alignment of the nanotubes. Indeed, we found that the order parameter of the sheets before the introduction of the liquid crystal was higher (S=0.45) than that after (S =0.33). This indicates that the presence of LC disturbs the alignment of the MWCNT sheets. We infer this is due to the shifting of the tubes while LC is inserted by capillary filling, which thus decreases the alignment.

The electrical measurements of the MWCNT+LC cells demonstrate that LCs can affect the electrical response of embedded MWCNT networks. The existence of strong interactions between the LC matrix and MWCNTs is supported by high resistance values. The increase of resistance when 5CB covers CNTs might be due to the π-π electron stacking at the CNT-LC interface. This was compared to the electrical properties of the drop-cast MWCNT film, which further highlights the importance of having well aligned CNT networks for practical purposes. On investigating the consequence of the temperature changes on the electrical resistance of MWCNT sheets+LC, it was observed that there is not a drastic change of resistance for LCs at different temperatures around the nematic-isotropic transition temperature, denoting no substantial effects induced by the thermal fluctuations nor any influence of dielectric constant of LC molecules. Hence, the temperature effects of MWCNT networks on resistance changes can be neglected within our working range of temperature.

Chapter 5

Pressure sensing using liquid crystals with carbon nanotubes

Overview of the chapter

This chapter presents the fabrication and development of two different kinds of resistive pressure sensors based on liquid crystals with carbon nanotubes. Two main LC-CNT configurations are targeted in this thesis: (i) vertical interconnects of MWCNTs in LC (the configuration discussed in Chapter 3) and (ii) planarly aligned MWCNT networks embedded in LC (the configuration discussed in Chapter 4). This entire chapter is divided into two main parts, each dealing with a specific configuration of the pressure sensor.

5.1 Introduction

The combination of one-dimensional macroscopic alignment, ultra-light weight, and high electrical and thermal conductivity of CNTs is quite exceptional in that it is possible to investigate the multifunctional aspects of nanotubes. The electromechanical properties of CNTs depend comprehensively on chirality, since axial strain opens a bandgap in some metallic CNTs, and opens or closes the bandgap in semiconducting CNTs [86][87][88][173]. Since mechanical strain can significantly reduce the conductivity of a metallic nanotube [85], CNTs are proposed to be used as active elements in nanoelectromechanical devices such as strain gauges and pressure sensors. The performance of single-walled carbon nanotubes (SWCNTs) is susceptible to chirality and purity and is hence very difficult to control. Even though multi-walled carbon nanotubes (MWCNTs) tend to be more prone to defects, they are much more cost-effective and can be grown with comparatively high purity. Further, MWCNTs are not susceptible to the intrinsic limitations related to chirality and can tolerate intensive processing. Hence, from the practical point of view, we concentrate in this research on analysing and implementing multi-walled carbon nanotubes to develop pressure sensors.

As previously mentioned, LC phases possess the fluidity of liquids as well as the long-range orientational ordering of solids. Additionally, owing to their softness and high responsiveness, LC was chosen as an ideal matrix to embed the CNTs in our easily recoverable pressure sensors. LCs in combination with CNTs have attracted a lot of attention as a medium for simultaneously ordering and dispersing CNTs due to their ease of forming large-scale monodomains: this is especially true for thermotropic LCs and can be achieved by simply controlling the interfacial layers or by using external electric or magnetic fields [104][105][174].

The first configuration of pressure sensor (Sensor 1) discussed in this chapter is designed based on the method of creating vertical interconnects of MWCNTs in a nematic liquid crystal using disclination lines as templates as previously elaborated in Chapter 3. We take advantage of the colloidal-nematic interactions and use them to synthesize a three-dimensional conductive wire of MWCNTs that automatically connect electrodes at the designated locations. This system can be used to detect the variations in the electrical

properties in response to an applied local pressure. The softness of the LC matrix enables deformations of continuous CNT network onto defect lines, thereby disrupting it upon applying pressure. Nevertheless, the defect line acts as a trap, restoring the original CNT network after the deformation and thus making it reversible.

The second part of this chapter describes our study aimed at the fabrication and characterization of an alternate configuration of a resistive pressure sensor (Sensor 2), using aligned MWCNT sheets drawn from a multi-walled CNT forest (as previously elaborated in Chapter 4) integrated as the sensing element in a nematic liquid crystal. On applying pressure, the LC matrix uniformly distributes the pressure above the CNTs and improves the electrical conduction by reducing the inter-tube distance and, by doing so, providing information about the applied pressure. Here, we analyse the effect of thickness of cell spacers and the effect of multiple MWCNT sheet layers on the pressure response.

5.2 Working principle of CNT-based resistive sensors

Mechanical force can induce replicable variations in the electrical properties of CNT networks, making them an attractive candidate for resistive pressure sensors. The working principle of resistive sensors developed from a macroscopic carbon nanotube assembly involves the variation of their electrical resistance when subjected to an external force/pressure.

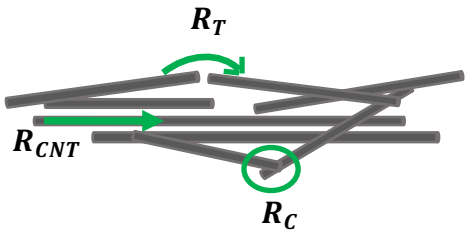

Figure 46: Schematic of electrical conduction in a randomly oriented CNT network.

We recall that the mechanism of pressure sensing in CNTs is governed primarily by the modification of two types of resistance, Figure 46, in a carbon nanotube network: (1) the

intrinsic tube resistance (R_{CNT}) of the CNT and (2) the inter-tube resistances of nanotubes that are in contact or in close vicinity to each other. Changes in the intrinsic resistance are due to the stretching of the C-C bond, resulting in a shift in energy bandgaps in response to an external strain [86][87][88][89]. The change in inter-tube resistance is further classified as change in contact resistance (R_C) [90][91], i.e. the change in resistance due to increase/decrease in the area of contact between physically connected tubes, and change in tunneling resistance (R_T) [92][93], i.e., the change in resistance due to a change in inter-tube distance. The orientation, configuration, and position of CNTs in a network all change when external pressure is applied, inducing a change in the conducting paths.

5.2.1 Sensing mechanism of Sensor 1

In this pressure sensor, the sensing material is a vertical network of MWCNTs confined into a defect line in a nematic liquid crystal. When suitable carbon nanotubes are introduced in a uniformly aligned LC matrix, they induce elastic distortions due to which they are attracted to and trapped onto the defect line. Chapter 3 addresses these distortions and interactions in detail. The linear network of carbon nanotubes in the disclination line allows the spatial regulation of interconnects even at comparatively low spatial density.

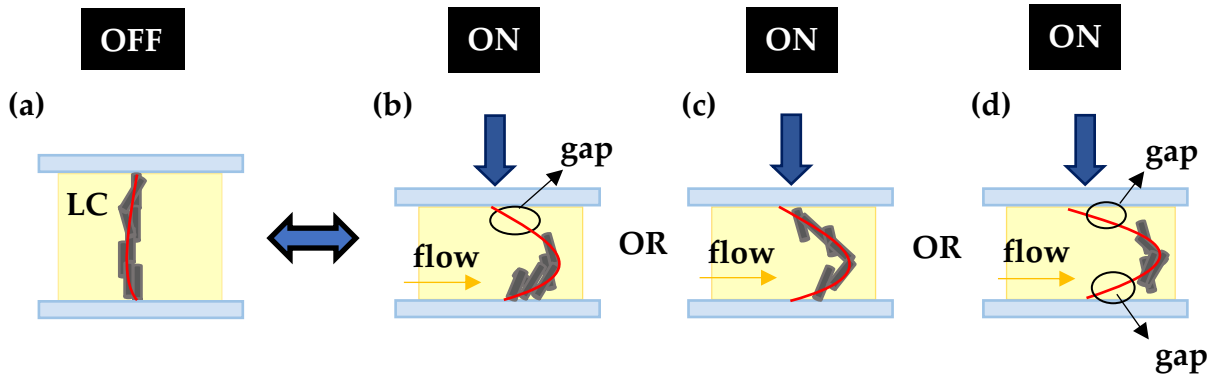

Figure 47: Pressure sensing mechanism of the device. When force/pressure is applied, the flow of the LC affects the embedded CNT network by breaking the electrode contacts: (b) Disrupting the top electrode contact. (c) Elongation of the defect line causing thinning of the network. (d) Disrupting both top and bottom electrode contacts.

When force/pressure is applied vertically on the top substrate (**ON** state), the LCs flow inducing an elongation of the defect line in the direction of flow with their ends remaining pinned to the substrate surface, consequently affecting the network of CNTs confined within it. In such a scenario, the vertical interconnect is stretched and either elongated while thinning the network, or the top or bottom electrode contact with the CNT network becomes disrupted, as seen in Figure 47, causing an increase in the resistance. Under circumstances of extreme flow within the sample, the electrode contacts with both the top and bottom electrodes may become disrupted but with the CNT networks nevertheless remaining intact due to their high van der Waals force. When the pressure is released (**OFF** state), the boundary conditions provided by the surface treatment induce elastic forces in the LC, triggering the contraction of the defect line to its initial position that satisfies both the boundary and minimal free energy considerations. The CNT network is also pulled along, recovering its vertical configuration. The disclination line thus serves as a trap to restore the original CNT network after the deformation, thereby making it reversible. Moreover, the softness of the LC matrix allows deformations of the CNT network for relatively small-applied forces.

5.2.2 Sensing mechanism of Sensor 2

In the case of Sensor 2, taking into account that the nanotubes do not extend over the full length of the CNT sheet, intrinsic tube resistance is anticipated to have an insignificant role in the pressure sensing mechanism. Thus, it may be deduced that inter-tube resistance governs the pressure response of CNT fibres. In the **OFF** state, some CNTs may not be involved the electrical conduction; therefore, inter-tube resistance is high. Additionally, in this sensor, the CNT sheets align the LC molecules in their direction of orientation. Upon exerting an increasing pressure on top of the physically interconnected CNT sheets, the liquid crystal flow on top of the CNTs, along their alignment direction, and reduce the inter-tube distance, thereby reducing the inter-tube resistance as more CNTs become involved in the electrical conduction.

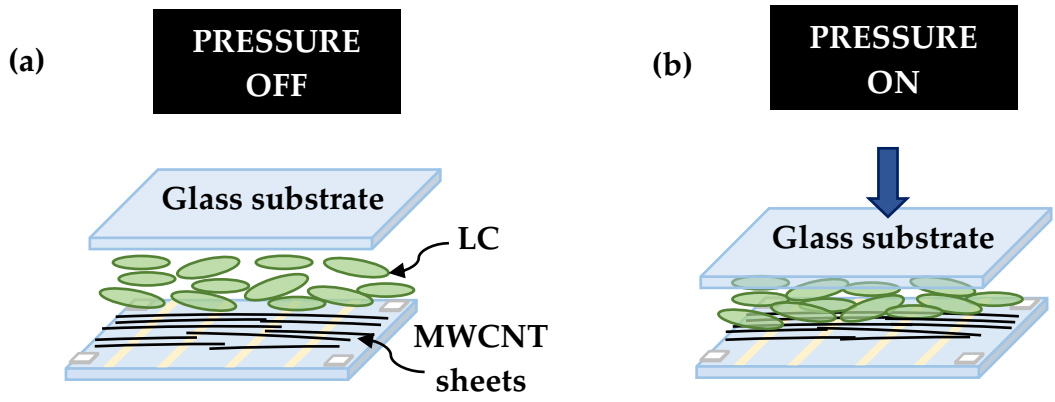

Figure 48: (a) Schematic representation of the MWCNT sheet-based pressure sensor. (b) Schematic model for the change of conductive structure in the CNT under pressure.

Moreover, once the pressure is **ON**, more nanotubes also come into contact with the bottom ITO electrodes, as shown in Figure 48. When the pressure is released, the LC reorients to its initial orientation, thereby making the sensor reversible.

5.3 Pressure response measurement setup

The pressure response of each sensor was calculated by measuring the force applied on the sensing device using a digital force gauge (Mark-10 model M3-5) mounted on a vertically translatable platform (Mark-10 ES10 manual test stand), as shown in Figure 49. The force was applied via a metal probe of area 6 mm^2. Different pressures can be applied to the sensing device by adjusting the compressive forces that can be exerted by the vertical motion of the test stand. The electrical properties were analysed using a sourcemeter (Keithley 2450 SourceMeter Instrument) in two-wire configuration for Sensor 1 and four-wire configuration for Sensor 2 using DC voltage. As Sensor 1 involves high resistance measurements, we used a constant-voltage method, where a constant voltage of 1mV is sourced and the corresponding current/resistance is measured. In comparison, in Sensor 2, we used constant-current method, where a constant current of 1 mA is sourced through the sensing device and the corresponding voltage/ resistance measured.

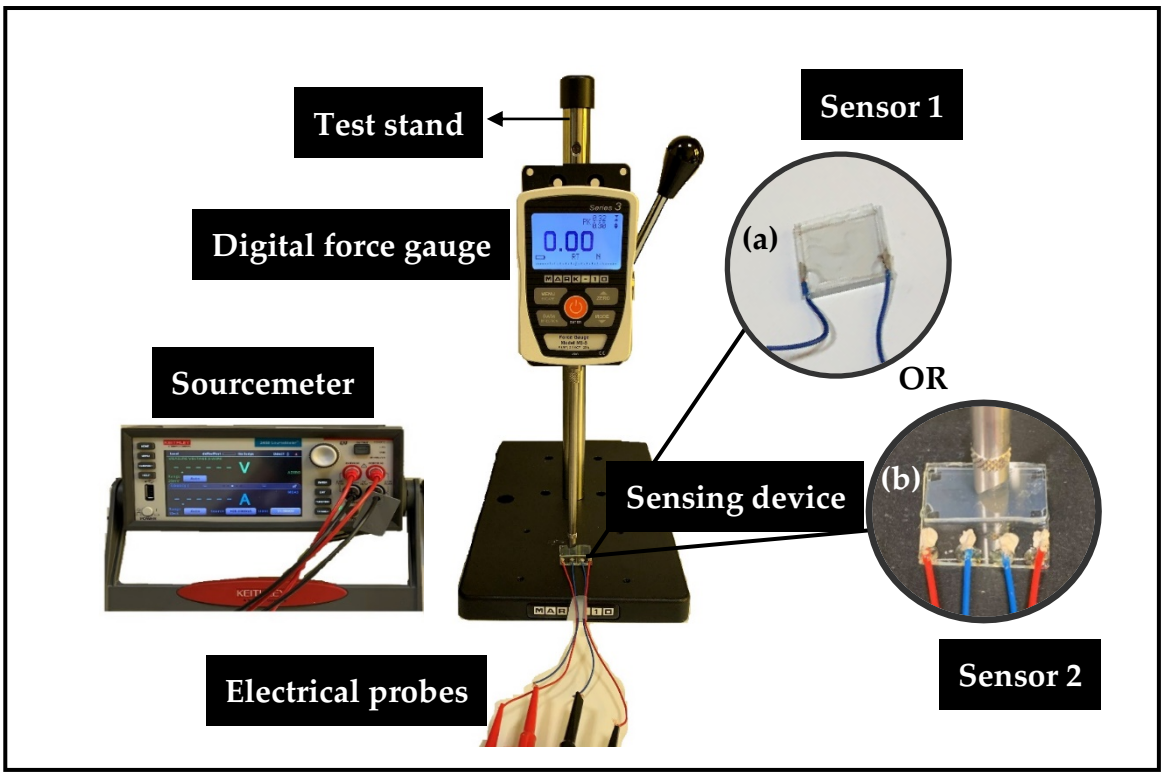

Figure 49: Experimental set-up for measuring the resistance of the pressure sensors. The sensing device can be either: (a) Sensor 1 (vertical interconnect of MWCNTs), or (b) Sensor 2 (aligned MWCNT sheets embedded in LC).

5.4 Sensor 1: Vertical interconnect of MWCNTs for pressure sensing

Unlike previous works, which rely on directed growth of individual nanotubes, the present sensor utilizes fabrication techniques for the creation of the vertical interconnects of CNTs. The active structure is composed of a liquid crystal embedding localized and vertically oriented MWCNT networks, realized after mixing the CNTs with liquid crystal via a self-assembly fabrication technique based on LC defect–CNT interaction. Since we used dispersions of pristine MWCNTs, we have the advantage of selecting CNTs of desired types and purity, characteristics influencing the values of resistance of the interconnect, which is not possible with CNTs grown in forests. After sufficient trapping, the CNTs form a continuous network inside the defect line, creating continuity of conduction with pathways

across it, and this sensor component offers improved tolerance to faults over individual nanotubes. In sensors based on CNT networks, when an individual carbon nanotube breaks, other nanotubes in the network will offer conductive pathways; in contrast, if only a single tube was used and broken, the corresponding sensing device will become defective. In Sensor 1, the recovery of the initial state of the defect line, that can elongate easily doubling its original length, is ensured by the liquid crystal with the tailor-made aligning surfaces. In CNT forest sensors, there is no equivalent recovery mechanism independent of the CNT properties. Moreover, the repetitive application of pressure can irreversibly deform the nanotubes in forests, but this is not expected in our system due to the containing effect of the defect line in the liquid crystal and its location and shape stability. However, in the current pressure sensor, the trapping of the CNTs onto the defect lines may be time-consuming and the stability of the device still needs improvement.

5.4.1 Fabrication of the sensor

The method of fabrication of the sensor exploits two inherent properties of nematic LCs: the capability to create disclination lines at specific locations and the ability to attract dispersions introduced into an aligned liquid crystal. Figure 50 demonstrates the various steps of fabrication process of the sensing device. The top and bottom layers of the sensor are commercial glass substrates coated with specific patterns (sketched in grey colour) of ITO, purchased from EHC Co. Ltd, Japan.

The first step was the application of appropriate surface treatment on the substrates using a Teflon bar, as described in Section 3.3. The second step was the assembling of the substrates in a way that the smeared Teflon surfaces faced each other. The spacer was defined using isolated copper wires (~150 μm thickness). The third step the filling of MWCNT+LC dispersion (prepared as discussed in Section 3.4.2) into the cell through capillary action, resulting in the creation of defect lines with MWCNTs becoming trapped on them. Step 4 illustrates the assembled sensor device. The electrical signals are acquired via the ITO electrodes on the top and bottom substrates. A constant input DC voltage was applied in two-

wire configuration via a sourcemeter between the electrodes and the changes in output resistance are monitored as effect of the applied pressures.

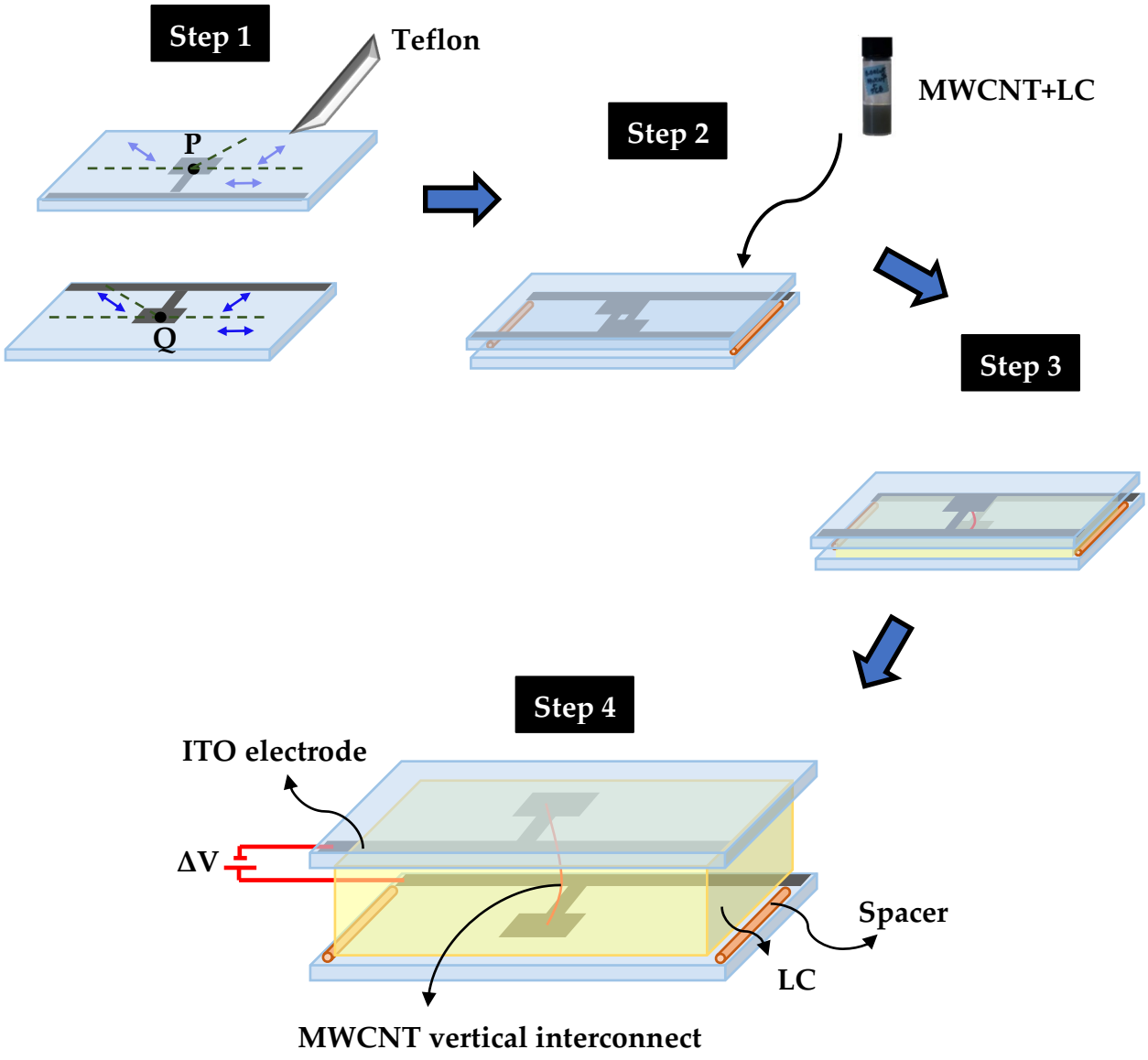

Figure 50: Fabrication process of the proposed pressure sensor of LC with vertical CNT network (sketched as orange line) within the two substrates. 1. Unidirectional smearing of Teflon on inner surface. The ITO electrodes on the glass substrates are represented in grey. 2. Assembling the cell. 3. Filling of MWCNT+LC dispersion and formation of defect line. 4. The assembled pressure sensor.

5.4.2 Pressure-resistance response of the sensor

To validate the concept of pressure sensing, the electrical conductivity through the cell must be measured. For that purpose, we also measured the cell's electrical resistance with LC alone, without the addition of MWCNTs. The electrical wires were soldered at the edges of the ITO electrodes and connected to a sourcemeter in two-wire configuration to measure the resulting resistance using DC (direct current) voltage. The optical characterization was performed using a polarizing optical microscope.

Liquid crystals are dielectrics, but some conductivity can be measured due to the ions present in the LC. However, the contribution of these ions can be minimized or even suppressed using DC conditions, since a constant voltage induces the motion of ions towards the electrode with opposite polarity: these ions will be localized at the electrodes and no longer contribute to the current. This is at the expense of a reduction of the effective voltage actually applied to the LC. The resistance of a cell without CNTs was measured for comparison, finding $R_{LC} = 76 \pm 16$ MΩ. Similar measurements were performed on the MWCNT+LC sample with nanotubes forming a possible continuous network (Figure 51) giving $R_{\mathrm{MWCNT+LC}} = 52 \pm 2.5$ MΩ. The result clearly indicates that the nanotubes are

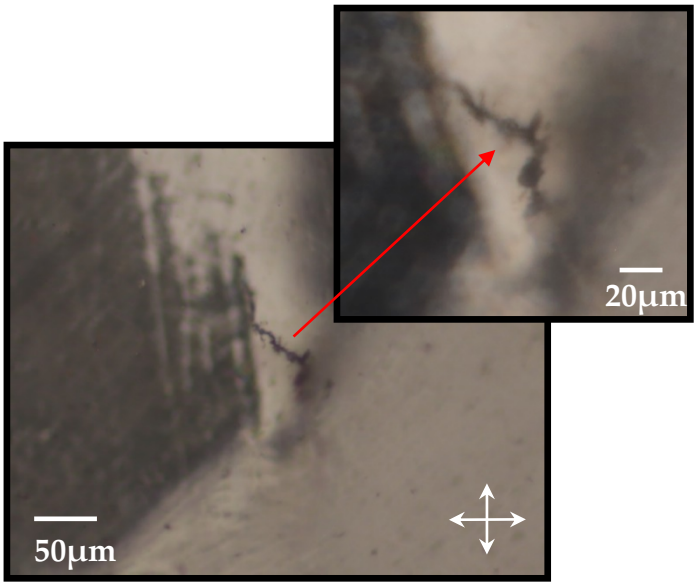

Figure 51: Polarizing optical microscopy image of the MWCNTs confined into the disclination line in the cell.

continuous and well connected. Thus, we observe that MWCNTs confined into a defect line in a nematic liquid crystal form a vertical network between the two glass plates coated by patterned alignment layer. Accordingly, the sensing element in this pressure sensor is a 3D wire of length ~150 µm and width of micrometre scale or less.

Figure 52 shows the experimental setup for measuring the pressure response of the vertical interconnect. The different components are as clearly indicated in Figure 49. The cell is placed between the metal probe and a horizontal stage. High-resistance measurements (above 10 MΩ) are extremely sensitive to environmental noise, such as electrostatic interference, so proper shielding of the device is critical [175]. Electrostatic interference can occur due to DC electrostatic fields generated from an electrically-charged object in the vicinity of the device, resulting in noisy readings [176]. These fields can be easily observed when movement of a person or a charged object near the experiment causes fluctuations in the measurement readings. Therefore, we enclosed the sensor in a box covered with a sheet of aluminium foil during the measurements.

Figure 52: Experimental set up for pressure sensing

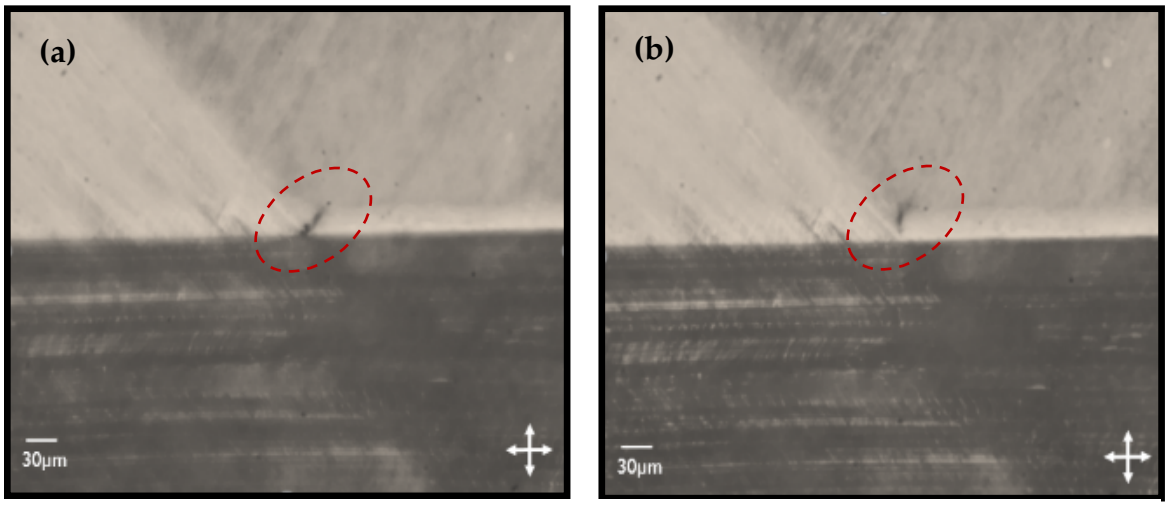

Figure 53: Polarizing optical microscopy image of the cell with a vertical interconnect of MWCNT (a) before applying pressure (b) during the application of pressure. The elongation of the defect line could be clearly seen.

Upon the application of force, the resistance increases and then reverts when the pressure is released. The softness of the LC matrix enables continuous deformations of the defect line and, in turn, of the CNT network confined onto the line, thereby altering the network upon applying pressure. The pressure exerted thus induces a flow in the liquid crystal that stretches the defect line, as can be seen in Figure 53, due to which the CNT network became elongated while breaking the electrode contact. This produced an increase in resistance, which could be read externally via the electrical leads.

The response of the sensor in terms of the change in resistance of the vertical interconnect when a force of 0.1 N is applied and then removed is shown in Figure 54. The change of resistance is solely due to the conduction of one vertical linear network embedded in a liquid crystal matrix. Prior to the application of pressure, the resistance values were $\sim 52 \pm 2.5$ MΩ and, upon applying the pressure, the resistance value gradually increased to >75 MΩ, denoting a disruption in the conduction, and immediately returned to its initial value upon releasing the force. The response time was ~6 s. This slow response to the application of pressure can be due to the existence of strong van der Waals forces among the physically entangled CNT networks on the defect line.

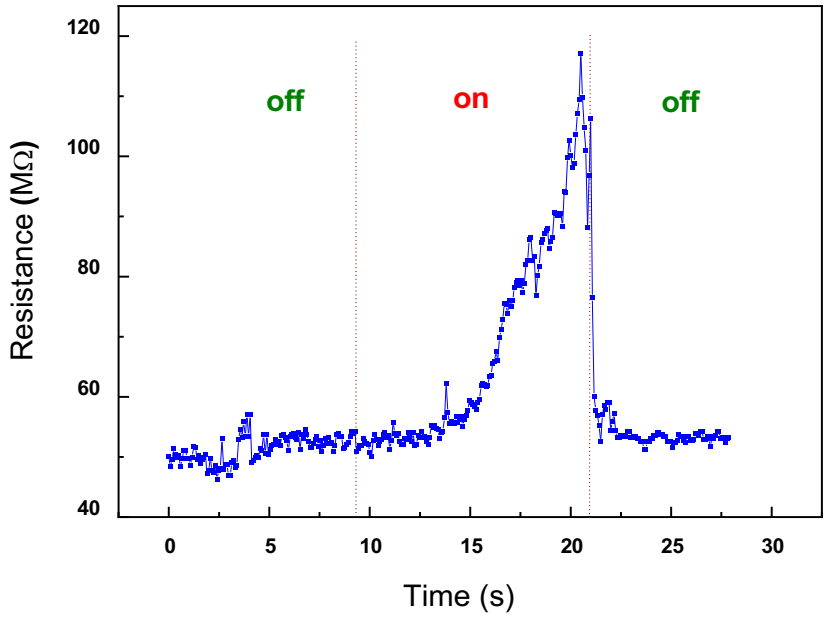

Figure 54: Plot of the response of the sensor to a force of 0.1 N. Off indicates the region when no force is applied, and on indicates the region when force = 0.1 N is applied

Thus, in Sensor 1, though the vertical interconnect of CNTs is the sensing element, the LC acts as a template to create the vertical interconnect of CNTs, and, at the same time, the LC matrix also transfers the external pressure to the linear CNT network formed in the defect line.

5.5 Sensor 2: Contact pressure sensor using aligned MWCNT sheets in liquid crystal

This section of the chapter elaborates the results of development and investigation of the second configuration of the pressure sensor targeted in this thesis, which is a contact pressure sensor based on highly aligned CNT sheets contained in a nematic liquid crystal matrix. The objective of the present study is to develop an easy, cost-effective, and reproducible method of integrating carbon nanotube sheets into LC for pressure sensing. The thickness of the developed sensor is a substantial aspect influencing the overall performance and the response of the sensor. Hence, we assess the effect of different spacer thicknesses and the subsequent effect of the number of CNT layers on the sensing response (one, two, three, and four).

5.5.1 Fabrication of CNT sheet-based pressure sensor

The pressure sensor was fabricated as elaborated in Section 4.3. A MWCNT forest synthesized by chemical vapour deposition (CVD) was purchased from A-Tech System Ltd., Republic of Korea. Using a scalpel blade, the MWCNT sheets were drawn mechanically from the vertically grown MWCNT forest as described in Section 4.3.2. The CNT sheets were stretched for unidirectional alignment [14] and were directly deposited on the ITO-coated glass substrates consisting four thin strips of etched ITO electrodes separated by 5 mm distance, with the inner two to be used as sensing electrodes and outer two as sourcing electrodes (Figure 55). MWCNT sheets were stacked, one on top of another, up to four times for samples with multiple layers, as shown in Figure 55(c). The CNT sheets produced by this approach are densified with ethanol for better adhesion to the substrate. Cells were prepared by using bare glass as the top substrate and MWCNT sheet deposited on etched ITO substrate as the bottom one, Figure 55(a).

The cell thickness was defined using soda-lime glass microspheres (silica beads; purchased from Cospheric) for 30 µm and polydimethylsiloxane (PDMS) of thicknesses 80 µm, 150 µm, 250 µm and 400 µm sealed onto the glass substrate after surface activation with oxygen

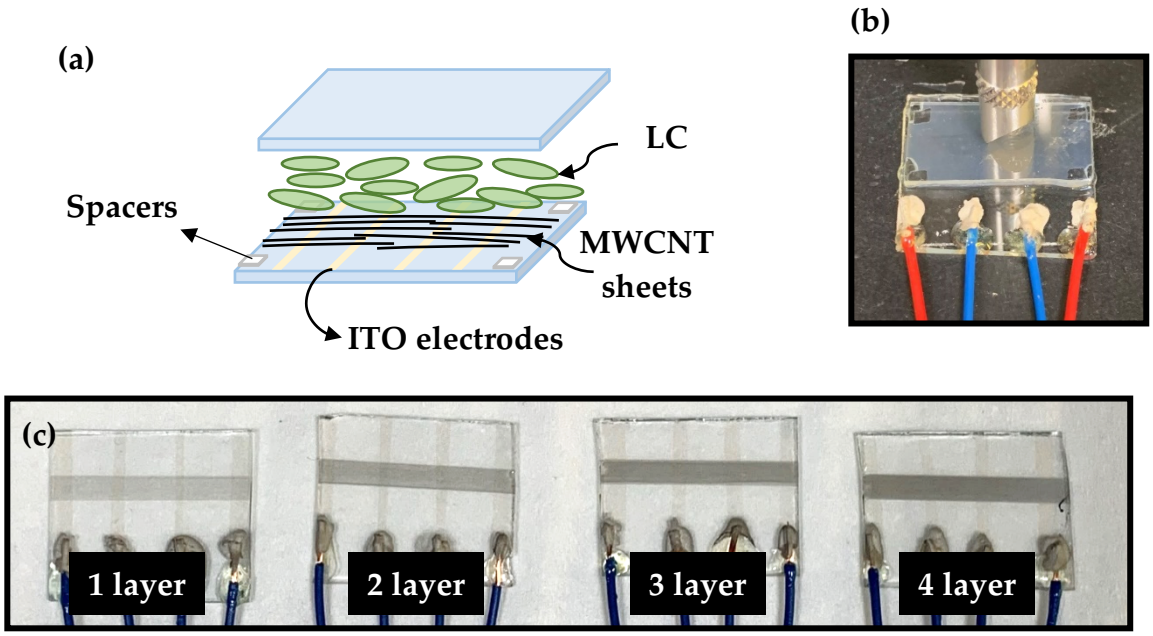

Figure 55: (a) Schematic representation of the MWCNT sheet-based pressure sensor. (b) Fabricated sensor. (c) Multiple layers of MWCNT sheet deposited on ITO glass substrate

plasma. Thanks to its intrinsic flexibility and the possibility of irreversible bonding to glass, PDMS was chosen as the ideal material for spacers. External pressure applied will cause the PDMS to elastically deform and distribute the applied pressure uniformly within the sample. The LC 5CB was introduced into the cell via capillary action. The dimension of the sensing area is ~22.5 mm × 9.5 mm.

5.5.2 Pressure response measurements

The electrical properties were characterized using a sourcemeter in four-wire configuration using DC voltage. The pressure/force was usually applied on the sample between the inner electrical probes. Figure 55 illustrates the schematic of the MWCNT sheet-based pressure sensor. Here, the CNT sheets also act as an aligning layer, thereby orienting the LC in the CNT alignment direction. In the **OFF** state, as seen in Figure 56(a), the POM texture is dark as the LC director is aligned along the direction of CNT orientation and is parallel to the polarizer. In the **ON** state, when the pressure is applied, a flow induced in the direction along the CNT

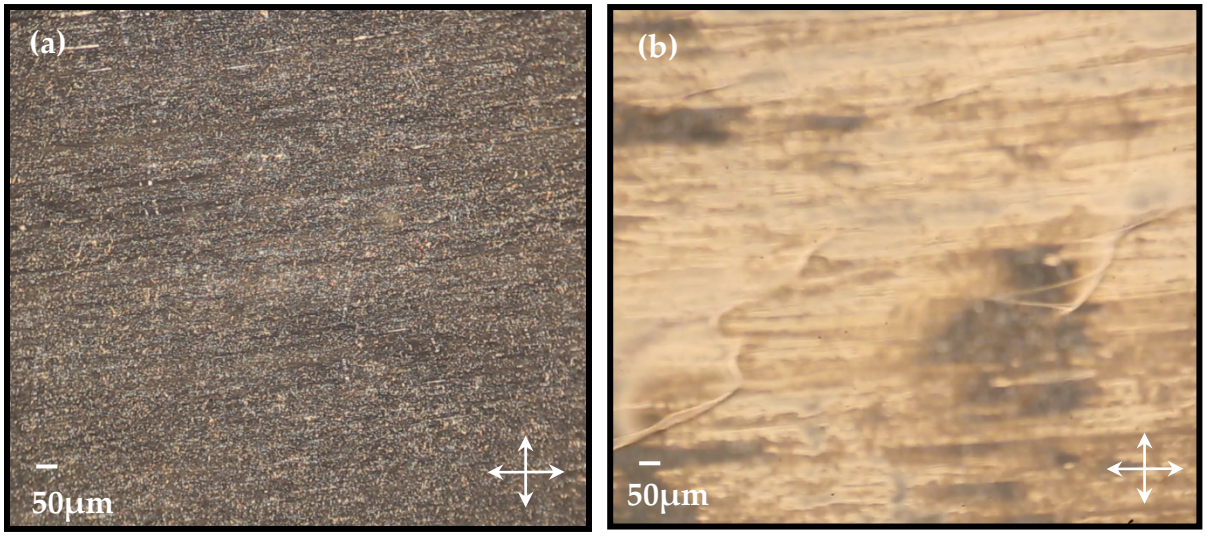

Figure 56: (a) LC orientation in Sensor 2 when no pressure is applied. (b) LC flow in the direction of CNT alignment during the application of pressure.

orientation causes deviations of the director from the initial state, seen as bright textures in the POM image in Figure 56(b). When the pressure is released, the director reorients to the initial state, thus making the sensor reversible. We evaluated the pressure response by systematically varying two components: the spacer thickness (30 µm, 80 µm, 150 µm, 250 µm, and 400 µm) and the number of MWCNT sheet layers (one, two, three, and four) with the optimum spacer thickness obtained.

5.5.2.1 Varying the spacer thickness of the sensor

The electrical resistance during the application and release of a constant force at specific intervals of time was measured to characterize the performance of the aligned CNT sheet + LC based sensors under different spacer thicknesses. We used spacers of thicknesses 30 µm, 80 µm, 150 µm, 250 µm, and 400 µm on a sample with one layer CNT sheet embedded in the LC. Each case thus, had different amounts of LC inserted into the cell.

The plot in Figure 57 shows the measured pressure response of a single layer of CNT sheet with different specified cell thicknesses. For this measurement, the force (=10 N) is applied for some time and released afterwards. **'On'** denotes the application of force and **'off'** denotes

the release of force. During this process, the resistance was measured using a sourcemeter by applying a constant current of 1 mA.

Generally, the phenomenon of pressure sensing in CNTs (as described in Section 5.2.2) is governed by the modification of two types of resistances in a carbon nanotube network: the intrinsic resistance of the tube and the contact resistance, more specifically the inter-tube and tube-electrode resistances. The changes in intrinsic resistance occurs due to the energy bandgaps or energy landscape modification in response to an external strain. When pressure is applied, it causes reorientation and flow of liquid crystal in the device. The LC thus transmits the external pressure to the embedded CNT network. The soft LC matrix narrows the gap between the CNTs and the ITO electrodes underneath, as well as between the nanotubes themselves, thereby facilitating a better contact, in this manner leading to a decreased inter-tube resistance.

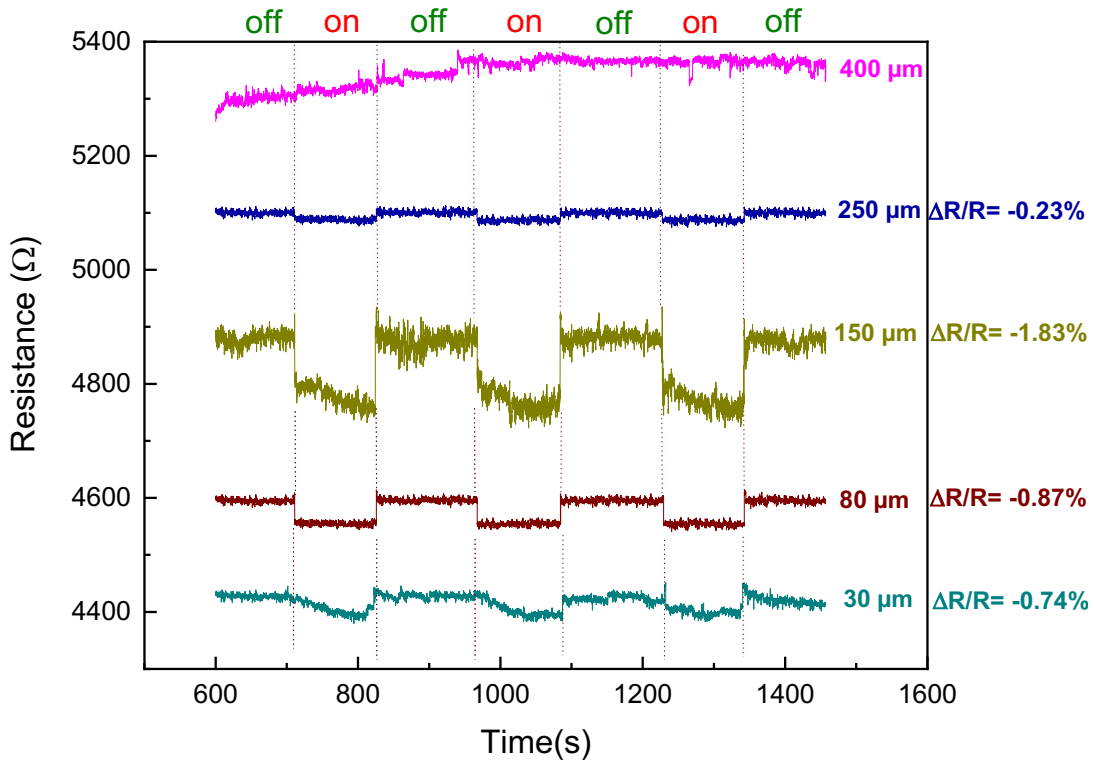

Figure 57: Pressure response (46 kPa) of the sensor with single layer of CNT sheet for different spacer thicknesses: 30 µm (defined using silica beads), 80 µm, 150 µm, 250 µm, and 400 µm (made from PDMS). 'On' indicates the region when force is applied and 'off' denotes the release of force.

From the values of relative change in resistances obtained, for the different spacer thickness, as shown in Table 2, we observe that, in the presence of sufficient amount of LC that flows on top of the CNTs, the pressure applied on a bundle of intersecting conducting CNT fibres lead to a decrease in the contact resistance of the intersecting fibres. Thanks to the ability of LCs to reorient on release of the applied force, the sensor recovers its initial state. A similar, though comparatively lower, resistance change was observed for the sensor with thickness of 30 µm. The spacers made of PDMS distributed the pressure more uniformly into the sample than the silica beads (30 µm). However, we still observe that the system also responds to small, non-uniform changes, but we notice that the sensor is less sensitive as the thickness of the spacer increases (250 µm and 400 µm). This is primarily because the same 10 N force applied to the thicker PDMS is not enough to cause as much deformation as the thin PDMS spacers and, thus, less pressure is transferred to the CNT sheets. The spacer thickness can accordingly be adjusted to the desired pressure sensing ranges. This sensor thickness dependence on the external applied pressure is consistent with that observed by Huang et.al [177].

Table 2: Comparison of the relative change in resistance for samples with different spacer thickness

Spacer thickness (µm)	Initial resistance R_0, (Ω); force: 0 N	Resistance R_{10}, (Ω); force: 10 N	Relative change in resistance $\Delta R/R_0$
30	4432	4399	-0.74%
80	4595	4555	-0.87%
150	4898	4808	-1.83%
250	5100	5088	-0.23%

Figure 58 clearly demonstrates the deformation of the PDMS (150 µm and 400 µm) when subjected to a force of 10 N. There was no liquid crystal inserted into the cell. These images were captured using a USB digital microscope (Andonstar V160) and the cell gap was

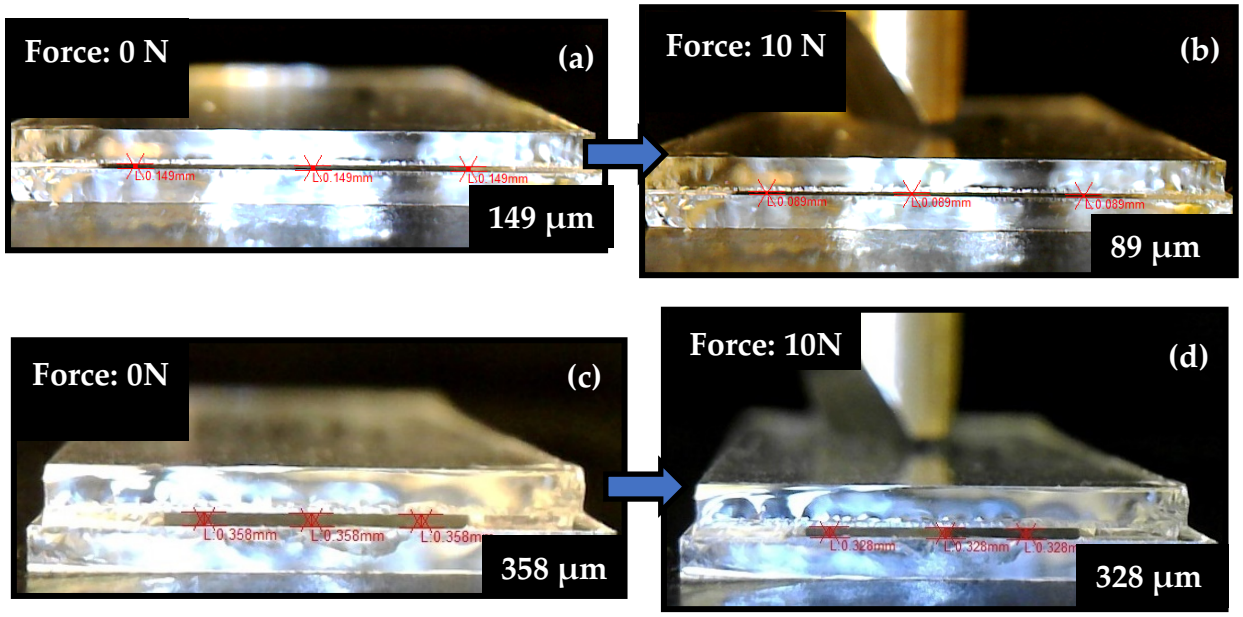

Figure 58: Side view of deformation of the cell with two glass substrates having no LC inserted and sandwiched using PDMS spacer. (a) Cell with a 150 µm spacer with no applied force, with a measured cell gap of 149 µm. (b) Upon applying a force of 10 N, the cell gap was reduced to 89 µm. (c) Cell with a 400 µm spacer with no applied force, with a measured cell gap of 358 µm. (d) Upon applying a force of 10 N, the cell gap was reduced to 328 µm.

measured using the Andonstar measure software. It can be clearly noticed that the PDMS spacer of 150 µm thickness has comparatively more deformation to a force of 10 N than the 400 µm spacer. Initially, when no force was applied, the cell gap measured 149 µm and, upon applying a force of 10 N, reduced to 89 µm, resulting in a cell gap decrease of 60 µm, whereas the 400 µm spacer had a cell gap decrease of only 30 µm upon application of force. This deformation can be enhanced by increasing the amount of applied force. However, our force gauge could only exert a maximum force of 25 N. Moreover, increasing the thickness of the sensor will require more amount of LC for our present sensor dimensions (thus more resources), which also contributes to greater fluctuations in the electrical signal. Consequently, the PDMS spacer of thickness 150 µm was chosen as the spacer for our pressure sensor to obtain optimal sensor response over our pressure range of interest and was used for all further experiments.

5.5.2.2 Varying the CNT sheet layer of the sensor

In pressure sensors, individual CNT fibres will have to maintain physical interconnection to develop electron conducting routes or, at best, be sufficiently adjacent to enable electron tunnelling [178] when pressure is exerted. Hence, the responses of the nanotubes depend on this electrical interconnection. When pressure is applied, it causes the liquid crystal molecules to flow and reorient themselves, eventually modifying the electrical conduction of the embedded CNTs. In this section, we evaluate the pressure response of sensors with multiple layers (one, two, three, and four) of CNT sheets with 150 µm spacer thickness.

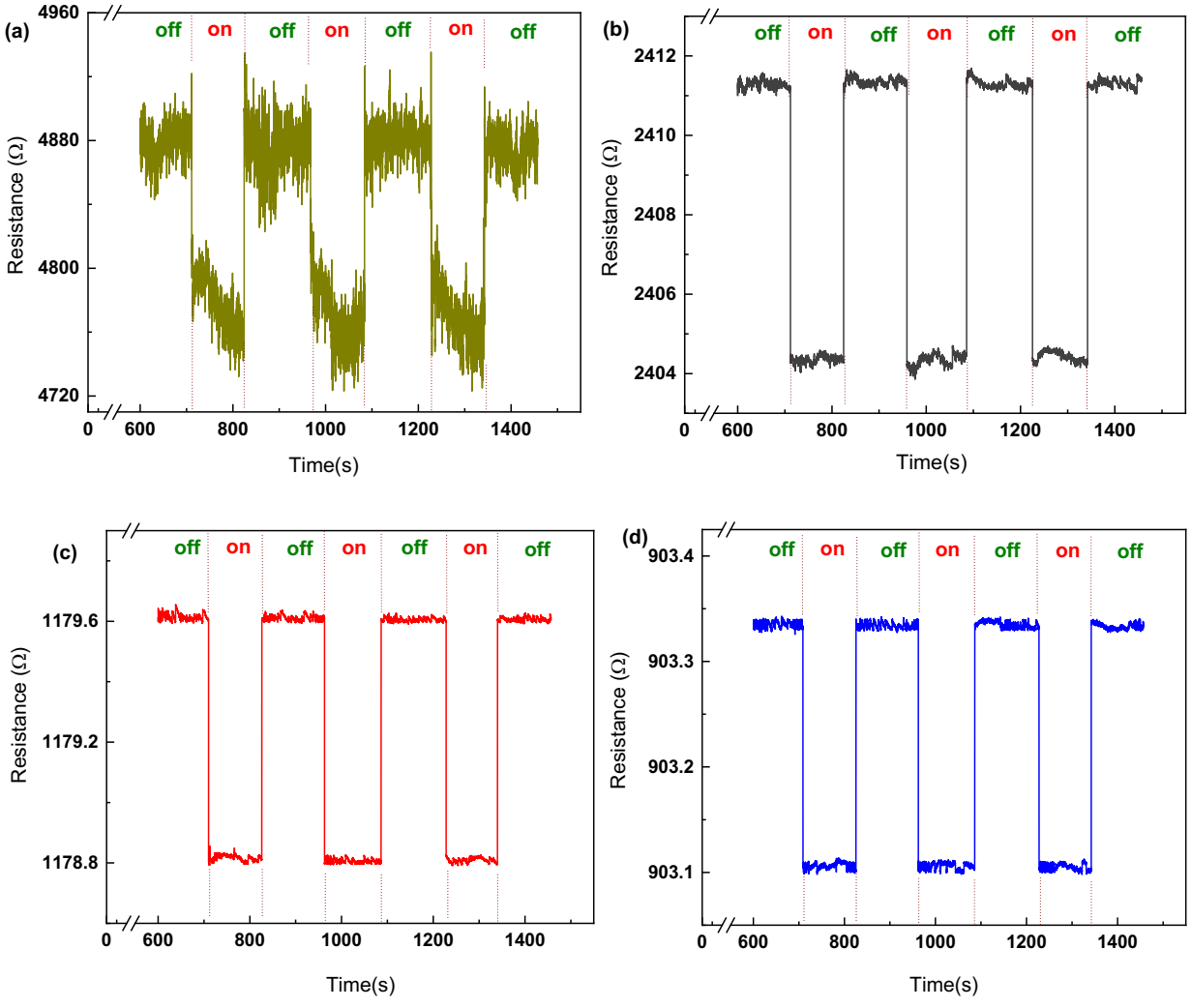

Figure 59: Pressure response of sensor with (a) single layer (b) two layers (c) three layers (d) four layers of CNT sheets and 150 µm spacer thickness.

We observe that the sensitivity is highest in the sensor that had only one layer of MWCNT sheet, as seen in Figure 59(a), as it demonstrated the largest change in resistance ($\Delta R/R_0$: ~ -1.83%) due to higher possibility of electrical conduction through tunneling between the nanotubes. Whenever pressure was applied, the connections between the CNT fibres would improve, causing the resistance to decrease. The transmission studies of the CNT sheets in the presence of LC, as discussed in Section 4.7.2, indicated that there was ample spacing between the CNT fibres in a single layer CNT sheet compared to a four-layer sheet. As already presented, when one to four layers were deposited, sheet transparency decreased from 85% to 59%. The relative change in resistance for two-, three-, and four-layer CNT sheets was -0.29%, -0.068%, and -0.025% respectively. The four-layer CNT sheet had the greatest number of electrically interconnected CNT fibres and, consequently, had the least change in resistance to an applied pressure, as shown in Figure 59(d).

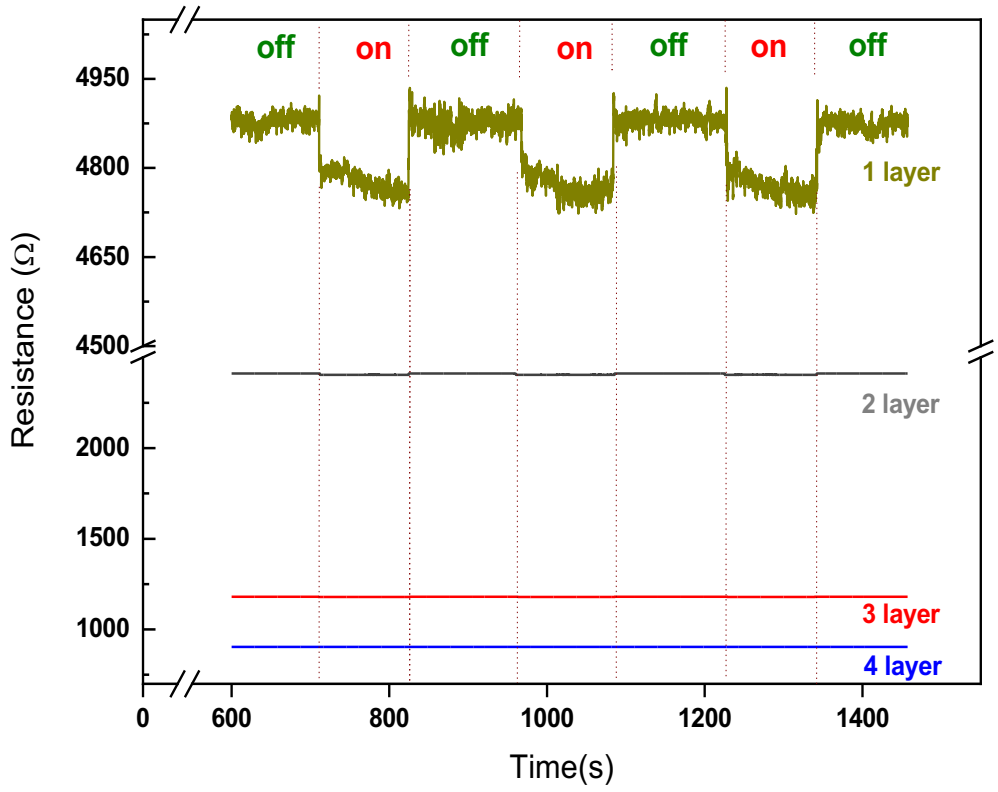

Figure 60: Pressure response of sensors with multiple layers of CNT sheets and a cell spacer of 150 µm thickness.

In comparison, in Figure 60, we found that, since the single layer CNT sheet has the lowest amount of electrically interconnected CNT fibres, the highest change in resistance to an applied pressure occurred there. Thus, a single layer of CNT sheet embedded in liquid crystal with a cell spacing of 150 μm was found to be the ideal configuration for our pressure sensor.

5.5.2.3 Spatial variation of pressure response

To examine the existence of any spatial variation in our sensor's pressure response, we investigated the changes in resistance when the position of pressure application was altered. We have already seen the pressure response when force was applied between the inner electrodes, on top of the MWCNT sheet, Figure 59 (a). We then, changed the location of application of force on top of MWCNT sheet to the right of the inner electrodes (Figure 61 (b)), and then on top of MWCNTs to the left of the inner electrodes (Figure 62 (b)) and, finally, onto an area where there is LC alone (Figure 63 (b)).

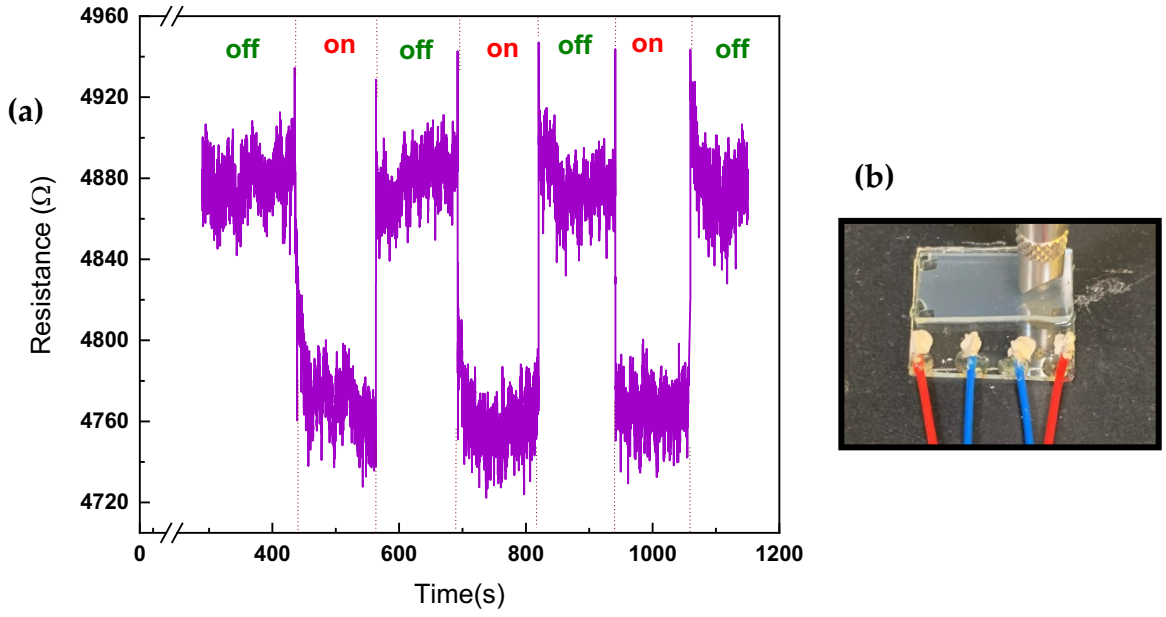

Figure 61: (a) Pressure response of sensor when pressure is applied on top of the MWCNT sheet to the right of the inner electrodes. (b) Photograph indicating the location of application of force.

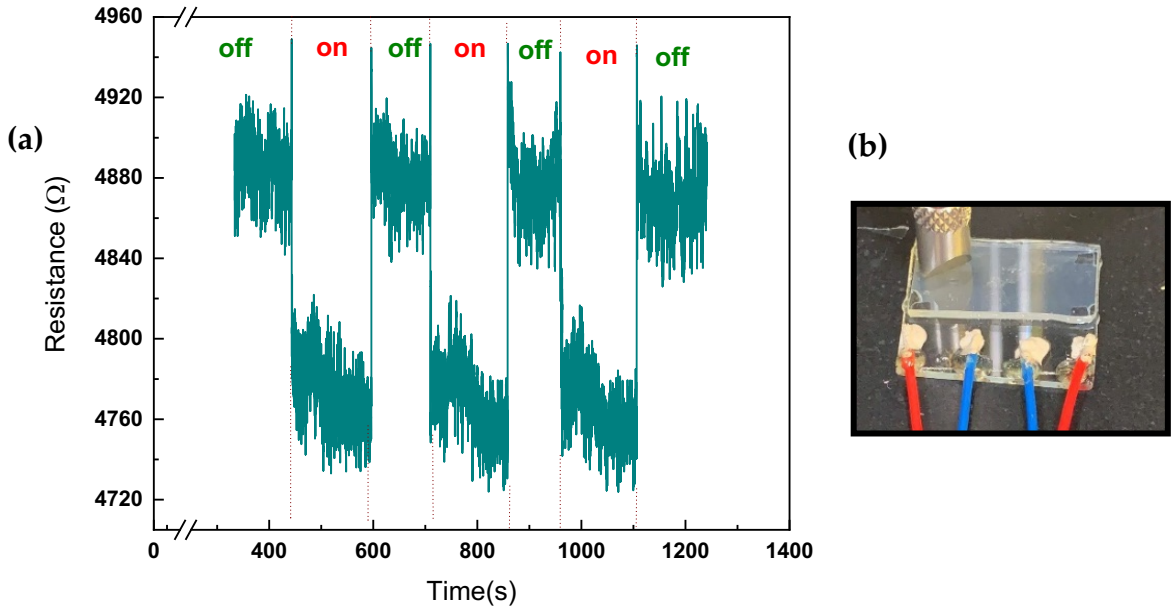

Figure 62: (a) Pressure response of sensor when pressure is applied on top of the MWCNT sheet to the left of the inner electrodes. (b) Photograph indicating the location of application of force.

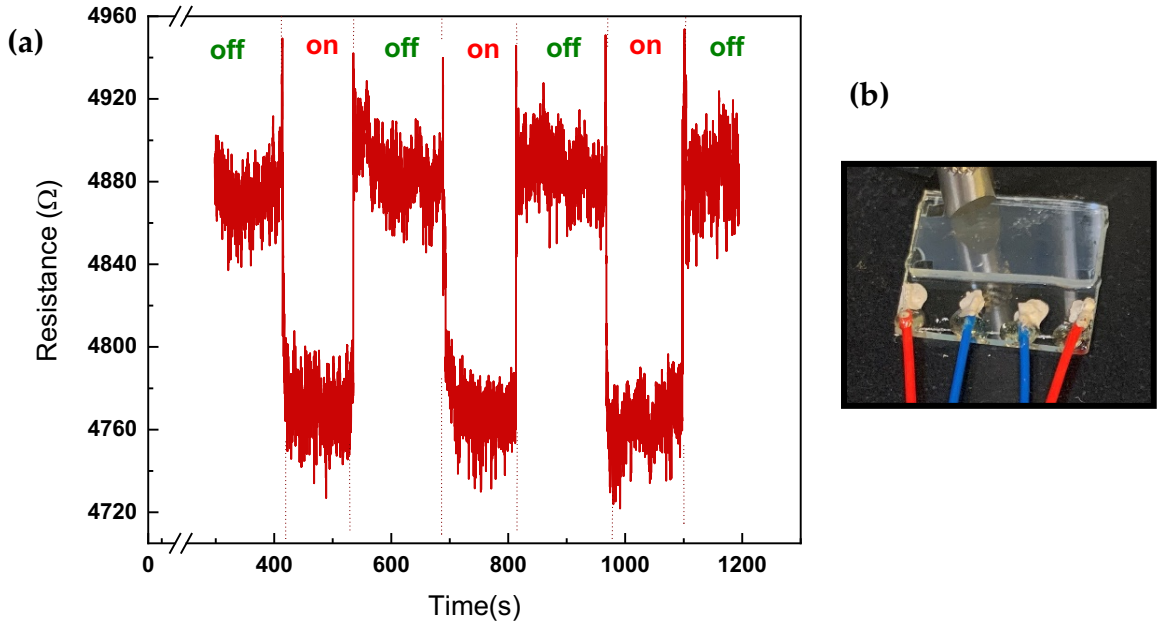

Figure 63: (a) Pressure response of sensor when pressure is applied an area where there is LC alone. (b) Photograph indicating the location of application of force.

We note that there is a slight difference between the values of the relative change in resistance when the force (10 N) was applied to various regions of the sensing device, as shown in Table 3. However, the maximum change in resistance is observed when the force was applied on top of the MWCNT sheets in between inner electrodes.

Table 3: Comparison of the relative change in resistance for different area of application of force (=10 N).

Position of the metal probe	On top of MWCNT sheet, between inner electrodes	On top of MWCNT sheet, to the right of inner electrodes	On top of MWCNT sheet, to the left of inner electrodes	On an area with LC alone
Relative change in resistance $\Delta R/R_0$	-2.48%	-2.38%	-2.40%	-2.28%

5.5.2.4 Pressure response and relaxation times

Figure 64 clearly demonstrates the pressure sensor response times when applying and releasing pressure. Before any pressure is applied, the resistance value is ~4880 Ω, but when a pressure of 46 kPa is applied on top of the sensor at 711.0312 s, the resistance immediately decreases to ~4810 Ω at 711.1139 s and, gradually, decreases and stabilizes to ~4760 Ω. Alternatively, the resistance returns to its initial value of ~4890 Ω at 824.3464 s while

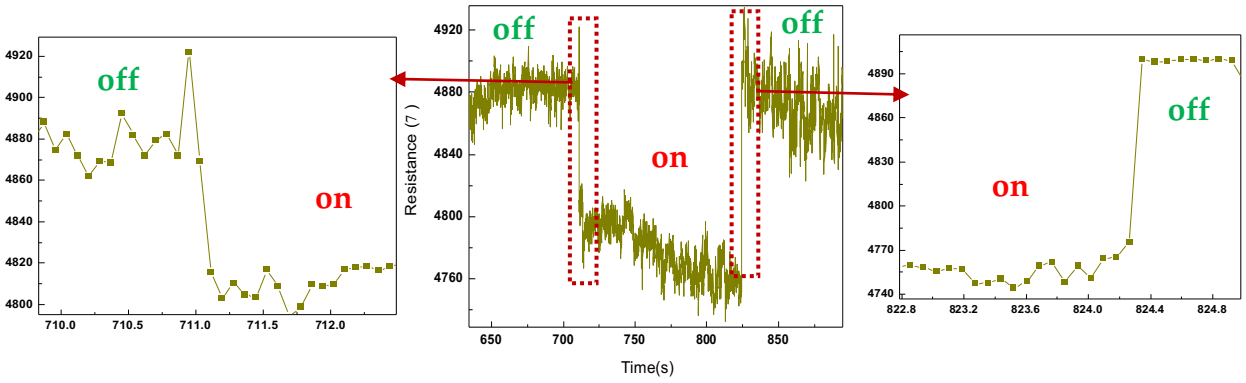

Figure 64: Pressure response and response time of the pressure sensor. Magnified sensor response taken from Figure 59(a).

removing the applied pressure at 824.2638 s. Consequently, this demonstrates that the response time is ~80 ms, irrespective of the pressure being applied or released.

Furthermore, a single CNT sheet+LC based pressure sensor consistently responded to changing pressures as demonstrated in Figure 65. We observed that the electrical resistance of the sensing device decreases linearly with applied pressure, making this system an ideal material for a resistive pressure sensor. It can be noted that, as the external uniaxial pressure increases from 0 kPa to 74 kPa, the DC resistance decreases from 5472 Ω to 5285 Ω, with the resistance per unit pressure decrease being ~2.42 $\Omega \cdot kPa^{-1}$. The observed decrease in resistance is caused by the densification of CNTs under the influence of pressure, thereby creating a more continuous electrical pathway through which current flows easily through the electrically interconnected CNTs.

Similarly, when the pressure is reduced from 74 kPa to 0 kPa, the resistance of the device increases to the initial state. Therefore, the experimental results revealed that the relative change of resistance decreases as the applied pressure was increased and increases as the

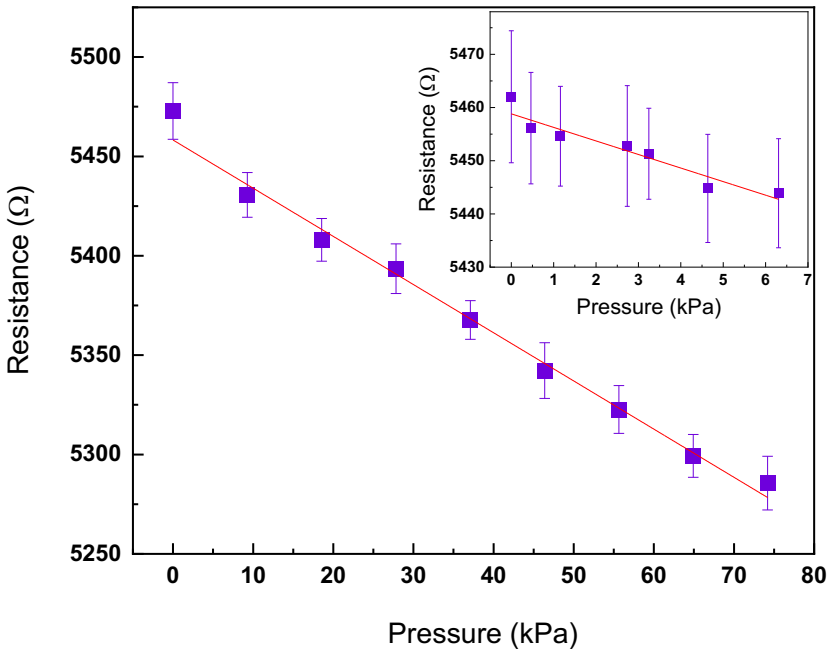

Figure 65: Response characteristic for the pressure sensor for different values of applied pressure. The inset shows the response characteristic for smaller pressure ranges (< 7 kPa).

applied pressure was decreased, as shown in Figure 66. Both curves are almost overlapping, signifying that the pressure sensor has negligible hysteresis. This ensures our pressure sensor can be completely restored after compression.

The sensitivity of the pressure sensor can be estimated as $(\Delta R/R_0)/\ \Delta P$, where R_0 is the initial resistance, ΔR is the change in resistance, and ΔP is the change in applied pressure. As clearly seen, the response of the sensor is fairly linear and the sensitivity (slope of the plot in Figure 66 at a particular pressure) is almost stable and has a value of ~-0.044%kPa^{-1}. However, in the low-pressure region (< 10 kPa), the response is highly nonlinear, with a sensitivity of ~-0.048%kPa^{-1}. Therefore, though the sensor displays a linear pressure response, the sensitivity needs further improvement.

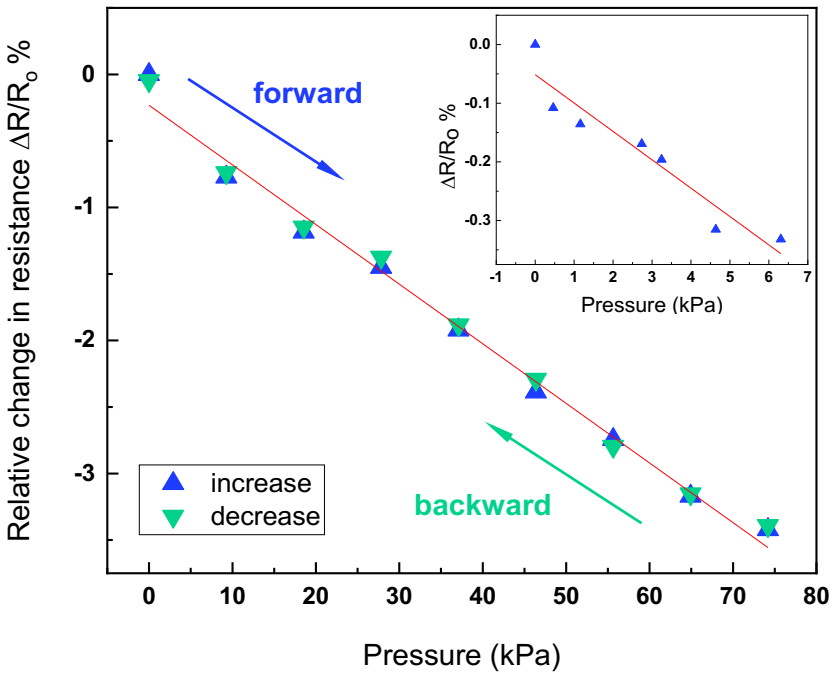

Figure 66: Relative resistance change with pressure for loading and unloading pressure on the sensor. Inset shows the relative resistance change for pressure < 7 kPa.

5.6 Conclusions

In summary, we have developed two kinds of resistive pressure sensors based on two configurations of carbon nanotubes in an LC. Sensor 1, with a vertical interconnect of multi-walled carbon nanotubes enveloped and kept in place by a liquid crystal layer via a simple fabrication strategy and Sensor 2, with horizontally aligned multi-walled carbon nanotube sheets embedded in a liquid crystal matrix.

In Sensor 1, multi-walled carbon nanotubes (MWCNTs) entrapped on a disclination line in a nematic LC is implemented as the resistive sensing element. The produced vertical interconnect is 150 μm in length and width in micrometre order. When pressure is applied, the defect line elongation causes changes in the measured resistance due to the reduction or interruption of the electrical conduction in the CNT network. On releasing the pressure, the LC defect line recovers from the elongation due to the surface treatment and the LC restores its initial alignment. This sensor displays good performance owing to the ease of deformation and recoverability of the vertical interconnect and can be easily reconfigured to create a sensor array of several such individual units that are able to detect the spatial distribution of the applied pressure.

In Sensor 2, we proposed a fabricating method for pressure sensors using highly aligned MWCNT sheets in a liquid crystal matrix as the sensing element. Such sheets can be easily pulled from the sidewall of a MWCNT forest, thus making the fabrication easy and cost-efficient. The spacing of the device is maintained using spacers made of polydimethylsiloxane of appropriate thickness. The spacer thickness also plays a role in the pressure response of the sensor. For an applied force of 10 N, sensor with a thickness of 150 μm showed the optimal pressure response. For thicker PDMS sensors, more amount of pressure has to be applied to achieve similar deformations in the PDMS, this would increase the sensing range, but the presence of more amount of liquid crystal can make the signal noisy. To examine the influence of MWCNT sheet layers on sensitivity, pressure sensors with different number of layers of MWCNT sheets were fabricated (one, two, three, and four). The resistance of the CNT sheets decreased with increasing layers of the CNT sheets. In addition, the sensor with one layer showed the highest sensitivity than the ones with multiple layers.

Consequently, single layer of MWCNT sheet embedded in LC with a spacing of 150 μm is chosen as the optimal configuration of the pressure sensor in our working range of pressures. The sensor demonstrated a sensitivity of 0.044%kPa^{-1}, over a pressure range of 0 to 74 kPa. When pressure is applied, LC flow on top of the CNTs along the CNT alignment direction and reduce the inter-tube resistance. On releasing the pressure, LC reorient to its initial orientation, thereby making the sensor recoverable. Although failing to inherit the ultra-sensitive resistive behaviour, the fabricated CNT sheet in LC based sensor still exhibits superior sensing performance in terms of good linearity, temperature stability, and reversible sensing.

Chapter 6

Conclusions and Outlook

The main objective of the work elaborated in this doctoral thesis was to develop a pressure sensor based on a combination of liquid crystals and carbon nanotubes. In doing so, we designed and developed two different configurations of LC-CNT based pressure sensors: a vertical configuration, where a vertical interconnect of MWCNT network trapped on a defect line acts as the sensing element, and a horizontal configuration, where MWCNT sheets embedded in LC are the sensing element. Through the different chapters of this thesis, we have systematically reported the fabrication techniques and the relevant optical and electrical characterizations of the components necessary for the successful development of these sensors.

The advances in surface patterning techniques to manipulate the self-assembly of LC molecules have been pivotal in the realization of liquid crystals for real-world applications. Such patterning techniques can also facilitate the creation of liquid crystal defect lines in predetermined locations. LC defect lines are attractive for analysing the LC distortions triggered by the presence of nanoparticles, as dispersed particles in LC are attracted to the defect line to reduce the overall energy of the system. We have investigated the interaction of two untreated cylindrical nanoparticles (rod-shaped $Mo_6S_2I_8$ nanowires and tube-shaped carbon nanotubes) that are not homotopically equivalent with a custom-made defect line in a nematic LC. We observe that the attractive forces are stronger on elongated bundles of nanowires than on similarly sized bundles of multi-walled carbon nanotubes, the reason being the difference in the attractive forces originating from the different LC distortions that are generated. The rod-shaped nanowires generate LC defects near their surface, as seen in colloidal dispersions of microrods. In contrast, MWCNTs, being hollow, do not form LC

defects near their ends; the MWCNTs are strongly bent, the strong planar anchoring of LC along these surfaces induces perturbations in the LC, resulting in their attraction to the defect line. SWCNTs, on the other hand, could not be trapped because they were much smaller and straighter, resulting in negligible deformations in the LC. Our findings, thus, advocate that the nematic interaction of liquid crystals can be profoundly different in nature depending upon their structural topology. The distortion fields produced by the nanoparticles couple with that of the defect line, eventually resulting in their trapping on the defect line. These findings are consistent with prior works on attracting treated inclusions to defect lines. Such materialization of defect lines introduces a novel perspective in fundamental liquid crystal physics and their applications.

The DC electrical characterisation of MWCNT sheets embedded in LC, discussed in Chapter 4, reveals that the strong interaction between the CNTs and LCs through π-π electron stacking can result in the high electrical resistance of the MWCNT sheets in the presence of LC. These measurements were compared to those from a randomly oriented MWCNT film, which highlight the importance of having aligned CNT networks for practical applications. In such a macroscopic CNT ensemble, the well-aligned MWCNT sheets can also act as an aligning layer, thereby aligning the LC molecules along the one-dimensional microgrooves between the CNT fibres. The optical studies also reveal that the LC disturbs the alignment of the MWCNT sheets, which can be attributed to the shifting of the tubes while LC is introduced through capillary filling.

Throughout this thesis, we have systematically analysed the different parameters and laid the foundation for the fabrication of LC-CNT based pressure sensors. In Sensor 1, we used LC defect lines as templates to generate the vertical interconnect of MWCNTs. The defect lines are tailor-made via surface patterning techniques. When an external pressure is applied, this defect line elongates, causing variations in measured resistance. Upon releasing the pressure, the defect line recovers, and LC is restored to the initial alignment. It is also possible to reconfigure this sensor to create an array of several such interconnects that are able to detect the spatial distribution of the applied pressure. In Sensor 2, MWCNT sheets embedded in LC acts as the sensing element. Upon application of an external pressure, LC

molecules flow on top of the MWCNT sheets along their alignment direction, causing a reduction in the inter-tube resistance. Upon releasing the pressure, the reorientation of the LC molecules causes the initial configuration of the pressure sensor to be recovered. In addition to reversible sensing, Sensor 2 also exhibits a linear response to pressure and good temperature stability.

Both sensors developed in this thesis offer an excellent proof of concept. However, several factors, such as sensitivity, still demand improvement. In Sensor 1, obtaining a well-connected MWCNT network was a challenge to begin with. This further hindered the electrical measurements. Through fine-tuning parameters such as the quality of the CNT dispersion and straightness of the defect line, we were able to successfully construct the present vertical interconnect of MWCNT. However, the trapping of CNTs into the defect line to form a well-connected network was time-consuming. This is probably a consequence of the defect line being too long. While we used a spacing of 150 μm for better visualisation and control under the microscope, if the cell spacing and, thus, the defect line is too small, the particles might sediment to the bottom before becoming trapped onto the defect line. Possible areas of further research would include probing optimum ways to improve the trapping efficiency by tuning the different geometrical aspects and parameters. To achieve this, numerical simulations would prove indispensable.

In the case of Sensor 2, we see that, though it exhibits good sensing characteristics, the sensitivity of the currently developed sensor is comparatively low. Further, the sensing range could also be varied by increasing the thickness of the cell spacing (PDMS spacers), but given the current dimensions of the sensor, this was not practical. Thus, minimizing the surface area of the sensor and increasing the cell spacing would be beneficial in terms of both requiring less resources and promoting a better response, as this allows the LC matrix to become sufficiently embedded within the MWCNT sheets. This would also benefit from numerical modelling to have a clear understanding of the influence of these dimensional parameters on the electrical transport mechanism. Unlike the current manually etched ITO electrodes, the electrodes in the optimized sensor could be deposited via lithographic techniques such as ink-jet printing. Therefore, controlling and understanding the influence of the dimensional parameters on the efficiency of the sensor is crucial for pressure sensing

applications, and further investigations should be carried out until they achieve the optimum properties for large-scale applications. An interesting avenue thus for further study would be the research into integrating these experimental results with numerical simulations in order to try to address the current gaps, in addition to being able for use in commercial applications especially as touch sensors in displays.

Bibliography

[1] A. Levi, M. Piovanelli, S. Furlan, B. Mazzolai, and L. Beccai, "Soft, Transparent, Electronic Skin for Distributed and Multiple Pressure Sensing," *Sensors*, vol. 13, pp. 6578–6604, 2013.

[2] P. Bai *et al.*, "Membrane-Based Self-Powered Triboelectric Sensors for Pressure Change Detection and Its Uses in Security Surveillance and Healthcare Monitoring," *Adv. Funct. Mater.*, vol. 24, no. 37, pp. 5807–5813, 2014.

[3] Y. Zang, F. Zhang, C. Di, and D. Zhu, "Advances of flexible pressure sensors toward artificial intelligence and health care applications," *Mater. Horizons*, no. 2, pp. 140–156, 2015.

[4] T. Someya, T. Sekitani, S. Iba, Y. Kato, H. Kawaguchi, and T. Sakurai, "A large-area, flexible pressure sensor matrix with organic field-effect transistors for artificial skin applications," *Proc. Natl. Acad. Sci. U. S. A.*, vol. 101, no. 27, pp. 9966–9970, 2004.

[5] J. Park *et al.*, "Giant tunneling piezoresistance of composite elastomers with interlocked microdome arrays for ultrasensitive and multimodal electronic skins," *ACS Nano*, vol. 8, no. 5, pp. 4689–4697, 2014.

[6] S. Park, M. Vosguerichian, and Z. Bao, "A review of fabrication and applications of carbon nanotube film-based flexible electronics," *Nanoscale*, no. 5, pp. 1727–1752, 2013.

[7] D. J. Lipomi *et al.*, "Skin-like pressure and strain sensors based on transparent elastic films of carbon nanotubes," *Nat. Nanotechnol.*, vol. 6, no. 12, pp. 788–792, 2011.

[8] T. W. Ebbesen, H. J. Lezec, H. Hiura, J. W. Bennett, H. F. Ghaemi, and T. Thio, "Electrical conductivity of individual carbon nanotubes," *Nature*, vol. 382, no. 6586, pp. 54–56, 1996.

[9] D. L. Carroll *et al.*, "Electronic Structure and Localized States at Carbon Nanotube Tips,"

Phys. Rev. Lett., vol. 78, no. 14, pp. 2811–2814, 1997.

[10] R. Saito, G. Dresselhaus, and M. S. Dresselhaus, *Physical Properties of Carbon Nanotubes*. Imperial College Press, UK, 1998.

[11] M. M. J. Treacy, T. W. Ebbesen, and J. M. Gibson, "Exceptionally high Young's modulus observed for individual carbon nanotubes," *Nature*, vol. 381, no. 6584, pp. 678–680, 1996.

[12] A. Maiti, A. Svizhenko, and M. P. Anantram, "Electronic Transport through Carbon Nanotubes: Effects of Structural Deformation and Tube Chirality," *Phys. Rev. Lett.*, vol. 88, no. 12, p. 4, 2002.

[13] K. Jiang, Q. Li, and S. Fan, "Spinning continuous carbon nanotube yarns," *Nature*, vol. 419, no. 6909, p. 801, 2002.

[14] M. Zhang, S. Fang, A. A. Zakhidov, S. B. Lee, and R. H. Baughman, "Strong, Transparent, Multifunctional, Carbon Nanotube Sheets," *Science*, vol. 309, no. August, pp. 1215–1220, 2005.

[15] H. S. Jang, S. K. Jeon, and S. H. Nahm, "The manufacture of a transparent film heater by spinning multi-walled carbon nanotubes," *Carbon*, vol. 49, no. 1, pp. 111–116, 2011.

[16] D. Jung, D. Kim, K. H. Lee, L. J. Overzet, and G. S. Lee, "Transparent film heaters using multi-walled carbon nanotube sheets," *Sens. Actuators, A*, vol. 199, pp. 176–180, 2013.

[17] N. Koratkar, A. Modi, E. Lass, and P. Ajayan, "Temperature effects on resistance of aligned multiwalled carbon nanotube films," *J. Nanosci. Nanotechnol.*, vol. 4, no. 7, pp. 744–748, 2004.

[18] D. Jung and G. S. Lee, "Strain-sensing characteristics of multi-walled carbon nanotube sheet," *J. Sens. Sci. Technol.*, vol. 22, no. 5, pp. 315–320, 2013.

[19] Z. Yang *et al.*, "An integrated device for both photoelectric conversion and energy storage based on free-standing and aligned carbon nanotube film," *J. Mater. Chem. A*, vol. 1, no. 3, pp. 954–958, 2013.

[20] J. Di *et al.*, "Dry-processable carbon nanotubes for functional devices and composites," *Small*, vol. 10, no. 22, pp. 4606–4625, 2014.

[21] R. Ruoff, D. Qian, and W. Liu, "Mechanical properties of carbon nanotubes: Theoretical predictions and experimental measurements," *Comptes Rendus Phys.*, vol. 4, no. 9, pp. 993–1008, 2003.

[22] C. T. White and T. N. Todorov, "Carbon nanotubes as long ballistic conductors," *Nature*, vol. 393, no. 6682, pp. 240–241, 1998.

[23] M. S. Purewal, B. H. Hong, A. Ravi, B. Chandra, J. Hone, and P. Kim, "Scaling of resistance and electron mean free path of single-walled carbon nanotubes," *Phys. Rev. Lett.*, vol. 98, no. 18, pp. 2–5, 2007.

[24] P. Kim, L. Shi, A. Majumdar, and P. L. McEuen, "Thermal Transport Measurements of Individual Multiwalled Nanotubes," *Phys. Rev. Lett.*, vol. 87, no. 21, p. 215502, Oct. 2001.

[25] B. Q. Wei, R. Vajtai, and P. M. Ajayan, "Reliability and current carrying capacity of carbon nanotubes," *Appl. Phys. Lett.*, vol. 79, no. 8, pp. 1172–1174, 2001.

[26] J. B. Fleury, D. Pires, and Y. Galerne, "Self-Connected 3D architecture of microwires," *Phys. Rev. Lett.*, vol. 103, no. 26, pp. 1–4, 2009.

[27] W. Fu, L. Liu, K. Jiang, Q. Li, and S. Fan, "Super-aligned carbon nanotube films as aligning layers and transparent electrodes for liquid crystal displays," *Carbon*, vol. 48, no. 7, pp. 1876–1879, 2010.

[28] A. Schindler, J. Brill, N. Fruehauf, J. P. Novak, and Z. Yaniv, "Solution-deposited carbon nanotube layers for flexible display applications," *Physica E Low Dimens. Syst. Nanostruct.*, vol. 37, pp. 119–123, 2007.

[29] T. K. Truong *et al.*, "Dynamic operation of liquid crystal cell with inherently nanogroove-featured aligned carbon nanotube sheets," *Curr. Appl. Phys.*, vol. 19, no. 2, pp. 162–167, 2019.

[30] A. Jákli and A. Saupe, *One- and Two-Dimensional Fluids: Properties of Smectic, Lamellar and Columnar Liquid Crystals*, 1st ed. CRC Press, Taylor & Francis Group, 2006.

[31] J. V Selinger, *Introduction to the Theory of Soft Matter: From Ideal Gases to Liquid Crystals*, 1st ed. Springer International Publishing Switzerland, 2016.

[32] F. Reinitzer, "Beiträge zur Kenntniss des Cholesterins," *Monatshefte für Chemie und verwandte Teile anderer Wissenschaften*, vol. 9, no. 1, pp. 421–441, 1888.

[33] P. Palffy-muhoray, "The diverse world of liquid crystals," *Phys. Today*, vol. 60, no. 9, pp. 54–60, 2007.

[34] M. Schadt, "Liquid crystal displays, LC-materials and LPP photo-alignment," *Mol. Cryst. Liq. Cryst.*, vol. 647, no. 1, pp. 253–268, 2017.

[35] J. L. Fergason, "LIQUID CRYSTALS," *Sci. Am.*, vol. 211, no. 2, pp. 76–85, Jul. 1964.

[36] A. D. Price and D. K. Schwartz, "DNA hybridization-induced reorientation of liquid crystal anchoring at the nematic liquid crystal/aqueous interface," *J. Am. Chem. Soc.*, vol. 130, no. 26, pp. 8188–8194, 2008.

[37] P. Taylor *et al.*, "Chemical and biological sensing using liquid crystals," *Liq. Cryst. Rev.*, pp. 29–51, 2013.

[38] D. J. Mulder, A. P. H. J. Schenning, and C. W. M. Bastiaansen, "Chiral-nematic liquid crystals as one dimensional photonic materials in optical sensors," *J. Mater. Chem. C*, vol. 2, no. 33, pp. 6695–6705, 2014.

[39] N. Popov *et al.*, "Thermotropic liquid crystal-assisted chemical and biological sensors," *Materials (Basel).*, vol. 11, no. 1, pp. 14–17, 2017.

[40] M. H. Peter J. Collings, *Introduction to Liquid Crystals: Chemistry and Physics*, 1st ed. CRC Press, Taylor & Francis Group, 1997.

[41] S. Chandrasekhar, B. K. Sadashiva, and K. A. Suresh, "Liquid crystals of disc-like molecules," *Pramana*, vol. 9, no. 5, pp. 471–480, 1977.

[42] D. Vorländer and A. Apel, "Die Richtung der Kohlenstoff-Valenzen in Benzolabkömmlingen (II.)," *Berichte der Dtsch. Chem. Gesellschaft (A B Ser.*, vol. 65, no. 7, pp. 1101–1109, 1932.

[43] Y. Matsunaga and S. Miyamoto, "Mesomorphic behavior of 2,4-Bis-(4-alkoxybenzylidene)cyclopentanones and related compounds," *Mol. Cryst. Liq. Cryst. Sci. Technol. Sect. A. Mol. Cryst. Liq. Cryst.*, vol. 237, no. 1, pp. 311–317, 1993.

[44] G. Friedel, "Les états mésomorphes de la matière," *Ann. Phys.*, vol. 9, no. 18, pp. 273–474, 1922.

[45] G. W. Gray, K. J. Harrison, and J. A. Nash, "New family of nematic liquid crystals for displays," *Electron. Lett.*, vol. 9, no. 6, pp. 130–131, 1973.

[46] P.G de Gennes and J. Prost, *The Physics of Liquid Crystals*. New York: Oxford University Press Inc., 1993.

[47] Iam-Choon Khoo, *Liquid Crystals*, 2nd ed. John Wiley & Sons, Inc., Hoboken, New Jersey, 2007.

[48] B. Jerome, "Surface effects and anchoring in liquid crystals," *Reports Prog. Phys.*, vol. 54, no. 3, pp. 391–451, 1991.

[49] J. P. F. Lagerwall and G. Scalia, "A new era for liquid crystal research: Applications of liquid crystals in soft matter nano-, bio- and microtechnology," *Curr. Appl. Phys.*, vol. 12, no. 6, pp. 1387–1412, 2012.

[50] F. C. Frank, "I. Liquid crystals. On the theory of liquid crystals," *Discuss. Faraday Soc.*, vol. 25, no. 0, pp. 19–28, 1958.

[51] C. W. Oseen, "The theory of liquid crystals," *Trans. Faraday Soc.*, vol. 29, no. 140, pp. 883–899, 1933.

[52] S. Chandrasekhar and G. S. Ranganath, "The structure and energetics of defects in liquid crystals," *Adv. Phys.*, vol. 35, no. 6, pp. 507–596, 1986.

[53] P. M. Chaikin and T. C. Lubensky, *Principles of Condensed Matter Physics*. Cambridge:

Cambridge University Press, 1995.

[54] H. Stark, "Physics of colloidal dispersions in nematic liquid crystals," *Phys. Rep.*, vol. 351, no. 6, pp. 387–474, 2001.

[55] F. C. Frank, "I. Liquid crystals. On the theory of liquid crystals," *Discuss. Faraday Soc.*, vol. 25, no. I, pp. 19–28, 1958.

[56] D. Andrienko, "Introduction to liquid crystals," *J. Mol. Liq.*, vol. 267, pp. 520–541, 2018.

[57] G. S. Ranganath, "Twist Disclinations in Elastically Anisotropic Nematic Liquid Crystals," *Mol. Cryst. Liq. Cryst.*, vol. 87, no. 3–4, pp. 187–195, 1982.

[58] M. Kleman and O. D. Lavrentovich, *Soft Matter Physics: An Introduction*, 1st ed. Springer-Verlag New York, 2004.

[59] L. M. Blinov, *Structure and Properties of Liquid Crystals*, 1st ed. Springer Netherlands, 2011.

[60] H. Agha, J. B. Fleury, and Y. Galerne, "Micro-wires self-assembled and 3D-connected with the help of a nematic liquid crystal," *Eur. Phys. J. E*, vol. 35, no. 9, pp. 1–12, 2012.

[61] M. Cavallaro *et al.*, "Exploiting imperfections in the bulk to direct assembly of surface colloids," *Proc. Natl. Acad. Sci.*, vol. 110, no. 47, pp. 18804–18808, 2013.

[62] D. Coursault *et al.*, "Linear self-assembly of nanoparticles within liquid crystal defect arrays," *Adv. Mater.*, vol. 24, no. 11, pp. 1461–1465, 2012.

[63] S. Iijima, "Helical microtubules of graphite carbon," *Nature*, vol. 354, pp. 56–58, 1991.

[64] S. Iijima, "Carbon nanotubes: past, present, and future," *Phys. B Condens. Matter*, vol. 323, no. 1–4, pp. 1–5, 2002.

[65] P. M. Ajayan and T. W. Ebbesen, "Nanometre-size tubes of carbon," *Reports Prog. Phys.*, vol. 60, no. 10, pp. 1025–1062, 1997.

[66] R. H. Baughman, A. A. Zakhidov, and W. A. De Heer, "Carbon nanotubes - The route toward applications," *Science*, vol. 297, no. 5582, pp. 787–792, 2002.

[67] T. Guo, P. Nikolaev, A. Thess, D. T. Colbert, and R. E. Smalley, "Catalytic growth of single-walled nanotubes by laser vaporization," *Chem. Phys. Lett.*, vol. 243, no. 1, pp. 49–54, 1995.

[68] M. José-Yacamán, M. Miki-Yoshida, L. Rendón, and J. G. Santiesteban, "Catalytic growth of carbon microtubules with fullerene structure," *Appl. Phys. Lett.*, vol. 62, no. 6, pp. 657–659, 1993.

[69] T. K. Truong, Y. Lee, and D. Suh, "Multifunctional characterization of carbon nanotube sheets, yarns, and their composites," *Curr. Appl. Phys.*, vol. 16, no. 9, pp. 1250–1258, 2016.

[70] P. Nikolaev *et al.*, "Gas-phase catalytic growth of single-walled carbon nanotubes from carbon monoxide," *Chem. Phys. Lett.*, vol. 313, no. 1, pp. 91–97, 1999.

[71] N. Hamada, S. Sawada, and A. Oshiyama, "New one-dimensional conductors: Graphitic microtubules," *Phys. Rev. Lett.*, vol. 68, no. 10, pp. 1579–1581, Mar. 1992.

[72] M. S. Dresselhaus, G. Dresselhaus, and P. C. Eklund, *Science of Fullerenes and Carbon Nanotubes*. Academic Press, 1996.

[73] P. J. F. Harris, *Carbon Nanotube Science: Synthesis, Properties and Applications*. Cambridge University Press, 2009.

[74] W. Obitayo and T. Liu, "A Review: Carbon Nanotube-Based Piezoresistive Strain Sensors," *J. Sensors*, vol. 2012, p. 652438, 2012.

[75] R. Saito, M. Fujita, G. Dresselhaus, and M. S. Dresselhaus, "Electronic structure of chiral graphene tubules," *Appl. Phys. Lett.*, vol. 60, no. 18, pp. 2204–2206, 1992.

[76] I. Stavarache *et al.*, "Electrical behavior of multi-walled carbon nanotube network embedded in amorphous silicon nitride," *Nanoscale Res. Lett.*, vol. 6, no. 1, p. 88, 2011.

[77] S. Frank, P. Poncharal, Z. L. Wang, and W. A. De Heer, "Carbon nanotube quantum resistors," *Science*, vol. 280, no. 5370, pp. 1744–1746, 1998.

[78] J.-P. Salvetat *et al.*, "Elastic and Shear Moduli of Single-Walled Carbon Nanotube

Ropes," *Phys. Rev. Lett.*, vol. 82, no. 5, pp. 944–947, 1999.

[79] B. Peng *et al.*, "Measurements of near-ultimate strength for multiwalled carbon nanotubes and irradiation-induced crosslinking improvements.," *Nat. Nanotechnol.*, vol. 3, no. 10, pp. 626–631, 2008.

[80] M. F. Yu, B. S. Files, S. Arepalli, and R. S. Ruoff, "Tensile loading of ropes of single wall carbon nanotubes and their mechanical properties," *Phys. Rev. Lett.*, vol. 84, no. 24, pp. 5552–5555, 2000.

[81] X. Wang *et al.*, "Fabrication of Ultralong and Electrically Uniform Single-Walled Carbon Nanotubes on Clean Substrates," *Nano Lett.*, vol. 9, no. 9, pp. 3137–3141, 2009.

[82] Y. Lan, Y. Wang, and Z. F. Ren, "Physics and applications of aligned carbon nanotubes," *Adv. Phys.*, vol. 60, no. 4, pp. 553–678, 2011.

[83] C. Berger, Y. Yi, Z. L. Wang, and W. A. de Heer, "Multiwalled carbon nanotubes are ballistic conductors at room temperature," *Appl. Phys. A*, vol. 74, no. 3, pp. 363–365, 2002.

[84] M. Zamkov, A. S. Alnaser, B. Shan, Z. Chang, and P. Richard, "Probing the intrinsic conductivity of multiwalled carbon nanotubes," *Appl. Phys. Lett.*, vol. 89, no. 9, p. 93111, Aug. 2006.

[85] T. W. Tombler *et al.*, "Reversible electromechanical characteristics of carbon nanotubes under local-probe manipulation," *Nature*, vol. 405, no. 6788, pp. 769–772, 2000.

[86] L. Yang, M. P. Anantram, J. Han, and J. P. Lu, "Bandgap Change of Carbon Nanotubes: Effect of Small Tensile and Torsional Strain," *Phys. Rev. B*, vol. 60, no. 19, pp. 13874–13878, 1999.

[87] R. Heyd, A. Charlier, and E. McRae, "Uniaxial-stress effects on the electronic properties of carbon nanotubes," *Phys. Rev. B - Condens. Matter Mater. Phys.*, vol. 55, no. 11, pp. 6820–6824, 1997.

[88] Liu Yang and Jie Han, "Electronic Structure of Deformed Carbon Nanotubes," *Phys. Rev. Lett.*, vol. 85, no. 1, pp. 154–157, 2000.

[89] E. D. Minot, Y. Yaish, V. Sazonova, J. Y. Park, M. Brink, and P. L. McEuen, "Tuning Carbon Nanotube Band Gaps with Strain," *Phys. Rev. Lett.*, vol. 90, no. 15, p. 4, 2003.

[90] C. Buia, A. Buldum, and J. P. Lu, "Quantum interference effects in electronic transport through nanotube contacts," *Phys. Rev. B - Condens. Matter Mater. Phys.*, vol. 67, no. 11, p. 4, 2003.

[91] A. Buldum and J. P. Lu, "Contact resistance between carbon nanotubes," *Phys. Rev. B - Condens. Matter Mater. Phys.*, vol. 63, no. 16, pp. 1–4, 2001.

[92] P. Sheng, E. K. Sichel, and J. I. Gittleman, "Fluctuation-induced tunneling conduction in carbon-polyvinylchloride composites," *Phys. Rev. Lett.*, vol. 40, no. 18, pp. 1197–1200, 1978.

[93] J. G. Simmons, "Generalized Formula for the Electric Tunnel Effect between Similar Electrodes Separated by a Thin Insulating Film," *J. Appl. Phys.*, vol. 34, no. 6, pp. 1793–1803, 1963.

[94] O. Kanoun *et al.*, "Flexible carbon nanotube films for high performance strain sensors," *Sensors*, vol. 14, no. 6, pp. 10042–10071, 2014.

[95] H. C. LI Yong, Wang Wanlu, LIAO Kejun and H. Z. & F. Qing, "Piezoresistive effect in carbon nanotube films," *Chinese Sci. Bull.*, vol. 48, no. 2, pp. 125–127, 2003.

[96] R. J. Grow, Q. Wang, J. Cao, D. Wang, and H. Dai, "Piezoresistance of carbon nanotubes on deformable thin-film membranes," *Appl. Phys. Lett.*, vol. 86, no. 9, pp. 1–3, 2005.

[97] R. C. Stampfer *et al.*, "Fabrication of single-walled carbon-nanotube-based pressure sensors," *Nano Lett.*, vol. 6, no. 2, pp. 233–237, 2006.

[98] A. Cao, P. L. Dickrell, W. G. Sawyer, M. N. Ghasemi-Nejhad, and P. M. Ajayan, "Super-compressible foamlike carbon nanotube films," *Science*, vol. 310, no. 5752, pp. 1307–1310, 2005.

[99] C. M. Lin, L. Y. Lin, and W. Fang, "Monolithic integration of carbon nanotubes based physical sensors," *Proc. IEEE Int. Conf. Micro Electro Mech. Syst.*, pp. 55–58, 2010.

[100] A. Bsoul, M. S. Mohamed Ali, and K. Takahata, "Piezoresistive pressure sensor using vertically aligned carbon-nanotube forests," *Electron. Lett.*, vol. 47, no. 14, pp. 807–808, 2011.

[101] M. Nihei, A. Kawabata, D. Kondo, M. Horibe, S. Sato, and Y. Awano, "Electrical properties of carbon nanotube bundles for future via interconnects," *Japanese J. Appl. Physics, Part 1 Regul. Pap. Short Notes Rev. Pap.*, vol. 44, no. 4R, pp. 1626–1628, 2005.

[102] A. P. Graham *et al.*, "Towards the integration of carbon nanotubes in microelectronics," *Diam. Relat. Mater.*, vol. 13, no. 4–8, pp. 1296–1300, 2004.

[103] K. A. Park, S. M. Lee, S. H. Lee, and Y. H. Lee, "Anchoring a liquid crystal molecule on a single-walled carbon nanotube," *J. Phys. Chem. C*, vol. 111, no. 4, pp. 1620–1624, 2007.

[104] M. D. Lynch and D. L. Patrick, "Organizing Carbon Nanotubes with Liquid Crystals," *Nano Lett.*, vol. 2, no. 11, pp. 1197–1201, 2002.

[105] I. Dierking, G. Scalia, P. Morales, and D. LeClere, "Aligning and reorienting carbon nanotubes with nematic liquid crystals," *Adv. Mater.*, vol. 16, no. 11, pp. 865–869, 2004.

[106] J. M. Russell, S. Oh, I. LaRue, O. Zhou, and E. T. Samulski, "Alignment of nematic liquid crystals using carbon nanotube films," *Thin Solid Films*, vol. 509, no. 1–2, pp. 53–57, 2006.

[107] H. Lee *et al.*, "Orientational and electro-optical properties of liquid crystal aligned with a directly spinnable carbon nanotube web," *Liq. Cryst.*, vol. 42, no. 3, pp. 322–327, 2015.

[108] J. P. F. Lagerwall and G. Scalia, "Carbon nanotubes in liquid crystals," in *Handbook of Liquid Crystals*, vol. 6, no. 2, 2014, pp. 1–40.

[109] A. Choudhary, G. Singh, and A. M. Biradar, "Advances in gold nanoparticle-liquid crystal

composites," *Nanoscale*, vol. 6, no. 14, pp. 7743–7756, 2014.

[110] Y. Garbovskiy and I. Glushchenko, "Nano-objects and ions in liquid crystals: Ion trapping effect and related phenomena," *Crystals*, vol. 5, no. 4, pp. 501–533, 2015.

[111] S. V. Burylov and Y. L. Raikher, "On the orientation of an anisometric particle suspended in a bulk uniform nematic," *Phys. Lett. A*, vol. 149, no. 5–6, pp. 279–283, 1990.

[112] Sergei V. Burylov and Yuri L. Raikher, "Orientation of a solid particle embedded in a monodomain nematic liquid crystal," *Phys. Rev. E*, vol. 50, no. 1, p. 358, 1994.

[113] P. Poulin and D. A. Weitz, "Inverted and multiple nematic emulsions," *Phys. Rev. E - Stat. Physics, Plasmas, Fluids, Relat. Interdiscip. Top.*, vol. 57, no. 1, pp. 626–637, 1998.

[114] M. Murali, H. Agha, A. Mrzel, and G. Scalia, "Difference in the interaction of nano-diameter rod and tubular particles with a disclination line in a nematic liquid crystal," *RSC Adv.*, vol. 10, no. 36, pp. 21473–21480, 2020.

[115] P. Poulin, H. Stark, T. C. Lubensky, and D. A. Weitz, "Novel colloidal interactions in anisotropic fluids," *Science*, vol. 275, no. 5307, pp. 1770–1773, 1997.

[116] E. M. Terentjev, "Disclination loops, standing alone and around solid particles, in nematic liquid crystals," *Phys. Rev. E*, vol. 51, no. 2, pp. 1330–1337, 1995.

[117] T. C. Lubensky, D. Pettey, N. Currier, and H. Stark, "Topological defects and interactions in nematic emulsions," *Phys. Rev. E - Stat. Physics, Plasmas, Fluids, Relat. Interdiscip. Top.*, vol. 57, no. 1, pp. 610–625, 1998.

[118] O. Mondain-Monval, J. C. Dedieu, T. Gulik-Krzywicki, and P. Poulin, "Weak surface energy in nematic dispersions: Saturn ring defects and quadrupolar interactions," *Eur. Phys. J. B*, vol. 12, no. 2, pp. 167–170, 1999.

[119] I. Muševič, M. Škarabot, U. Tkalec, M. Ravnik, and S. Žumer, "Two-dimensional nematic colloidal crystals self-assembled by topological defects," *Science*, vol. 313, no. 5789, pp. 954–958, 2006.

[120] U. Tkalec, M. Škarabot, and I. Muševic, "Interactions of micro-rods in a thin layer of a nematic liquid crystal," *Soft Matter*, vol. 4, no. 12, pp. 2402–2409, 2008.

[121] Y. Gu and N. L. Abbott, "Observation of Saturn-ring defects around solid microspheres in nematic liquid crystals," *Phys. Rev. Lett.*, vol. 85, no. 22, pp. 4719–4722, 2000.

[122] M. Kleman and O. D. Lavrentovich, "Topological point defects in nematic liquid crystals," *Philos. Mag. Taylor*, vol. 86, p. .4117-4137, 2006.

[123] I. Haller, "Alignment and wetting properties of nematic liquids," *Appl. Phys. Lett.*, vol. 24, no. 8, pp. 349–351, 1974.

[124] J. C. Wittmann and P. Smith, "Highly oriented thin films of poly(tetrafluoroethylene) as a substrate for oriented growth of materials," *Nature*, vol. 352, no. 6334, pp. 414–417, 1991.

[125] D. G. and Y. G. Pascal Hubert, Hanna Dreyfus, "Anchoring Orientation of Nematic and Smectic A Liquid Crystals on PTFE Treated Plates Treated Liquid Crystals," *J. Phys. II*, vol. 5, no. September, pp. 1371–1383, 1995.

[126] A. Hassanien, M. Tokumoto, A. Mrzel, D. Mihailovic, and H. Kataura, "Structural and mechanical properties of MoS2-Ix nanotubes and Mo6SxIy nanowires," *Physica E Low Dimens. Syst. Nanostruct.*, vol. 29, no. 3–4, pp. 684–688, 2005.

[127] D. Vrbani *et al.*, "Air-stable monodispersed Mo6S2I6 nanowires," *Nanotechnology*, vol. 15, pp. 635–638, 2004.

[128] J. H. Park *et al.*, "Investigation of composites of polymers and Mo6S2I8 nanowires," *Phys. Status Solidi Appl. Mater. Sci.*, vol. 211, no. 5, pp. 1122–1127, 2014.

[129] I. Dierking, G. Scalia, and P. Morales, "Liquid crystal-carbon nanotube dispersions," *J. Appl. Phys.*, vol. 97, no. 4, 2005.

[130] J. Liu *et al.*, "Fullerene pipes," *Science*, vol. 280, no. 5367, pp. 1253–1256, 1998.

[131] P. J. Boul *et al.*, "Reversible sidewall functionalization of buckytubes," *Chem. Phys. Lett.*, vol. 310, no. 3–4, pp. 367–372, 1999.

[132] D. Rajh *et al.*, "Effect of inorganic 1D nanoparticles on electrooptic properties of 5CB liquid crystal," *Phys. Status Solidi Appl. Mater. Sci.*, vol. 210, no. 11, pp. 2328–2334, 2013.

[133] C. Lapointe, A. Hultgren, D. M. Silevitch, E. J. Felton, D. H. Reich, and R. L. Leheny, "Elastic torque and the levitation of metal wires by a nematic liquid crystal," *Science*, vol. 303, no. 5658, pp. 652–655, 2004.

[134] P. V. Dolganov and V. K. Dolganov, "Director configuration and self-organization of inclusions in two-dimensional smectic membranes," *Phys. Rev. E - Stat. Nonlinear, Soft Matter Phys.*, vol. 73, no. 4, pp. 1–10, 2006.

[135] Y. Galerne, "Interactions of carbon nanotubes in a nematic liquid crystal. I," *Phys. Rev. E*, vol. 93, no. 4, p. 042702, 2016.

[136] H. Stark and D. Ventzki, "Stokes drag of spherical particles in a nematic environment at low Ericksen numbers," *Phys. Rev. E - Stat. Physics, Plasmas, Fluids, Relat. Interdiscip. Top.*, vol. 64, no. 3, p. 9, 2001.

[137] G. A. Oweimreen, A. K. Shihab, K. Halhouli, and S. F. Sikander, "Density measurements in the nematic and isotropic phases of 5CB and dilute solutions of tetraethylmethane in 5CB," *Mol. Cryst. Liq. Cryst.*, vol. 138, no. 1, pp. 327–338, 1986.

[138] Igor Muševič, *Liquid Crystal Colloids*, 1st ed. Springer International Publishing, 2017.

[139] G. K. Batchelor, "Slender-body theory for particles of arbitrary cross-section in Stokes flow," *J. Fluid Mech.*, vol. 44, no. 3, pp. 419–440, 1970.

[140] A. Peigney *et al.*, "Specific surface area of carbon nanotubes and bundles of carbon nanotubes," *Carbon*, vol. 39, pp. 507–514, 2001.

[141] J. P. F. Lagerwall, G. Scalia, M. Haluska, U. Dettlaff-Weglikowska, F. Giesselmann, and S. Roth, "Simultaneous alignment and dispersion of carbon nanotubes with lyotropic liquid crystals," *Phys. Status Solidi Basic Res.*, vol. 243, no. 13, pp. 3046–3049, 2006.

[142] P. R. Bandaru, "Electrical properties and applications of carbon nanotube structures,"

J. Nanosci. Nanotechnol., vol. 7, no. 4–5, pp. 1239–1267, 2007.

[143] L. M. Castano and A. B. Flatau, "Smart fabric sensors and e-textile technologies : a review," *Smart Mater. Struct.*, vol. 23, no. 5, 2014.

[144] K. Jiang, J. Wang, Q. Li, L. Liu, C. Liu, and S. Fan, "Superaligned carbon nanotube arrays, films, and yarns: A road to applications," *Adv. Mater.*, vol. 23, no. 9, pp. 1154–1161, 2011.

[145] M. B. Jakubinek *et al.*, "Thermal and electrical conductivity of array-spun multi-walled carbon nanotube yarns," *Carbon*, vol. 50, no. 1, pp. 244–248, 2012.

[146] J. H. Pöhls *et al.*, "Physical properties of carbon nanotube sheets drawn from nanotube arrays," *Carbon*, vol. 50, no. 11, pp. 4175–4183, 2012.

[147] J. A. Lee *et al.*, "All-solid-state carbon nanotube torsional and tensile artificial muscles," *Nano Lett.*, vol. 14, no. 5, pp. 2664–2669, 2014.

[148] W. A. De Heer, W. S. Bacsa, A. Chatelain, T. Gerfin, L. Forro, and D. Ugarte, "Aligned Carbon Nanotube Films : Production and Optical and Electronic Properties," *Science*, vol. 268, no. 5212, pp. 845–847, 1995.

[149] M. S. D. M Endo, H Muramatsu, T Hayashi, Y A Kim, M Terrones, "Nanotechnology: 'Buckypaper' From Coaxial Nanotubes," *Nature*, vol. 433, no. 7025, p. E10, 2005.

[150] S. G. Rao, L. Huang, W. Setyawan, and S. Hong, "Nanotube electronics: large-scale assembly of carbon nanotubes.," *Nature*, vol. 425, no. 6953, pp. 36–37, Sep. 2003.

[151] Y. Kim, N. Minami, W. Zhu, S. Kazaoui, R. Azumi, and M. Matsumoto, "Langmuir-Blodgett Films of Single-Wall Carbon Nanotubes: Layer-by-Layer Deposition and In-plane Orientation of Tubes," *Japanese J. Appl. Physics, Part 1 Regul. Pap. Short Notes Rev. Pap.*, vol. 42, no. 12, pp. 7629–7634, 2003.

[152] N. Saran, K. Parikh, D. S. Suh, E. Muñoz, H. Kolla, and S. K. Manohar, "Fabrication and Characterization of Thin Films of Single-Walled Carbon Nanotube Bundles on Flexible Plastic Substrates," *J. Am. Chem. Soc.*, vol. 126, no. 14, pp. 4462–4463, 2004.

[153] L. Hu, D. S. Hecht, and G. Grüner, "Carbon nanotube thin films: Fabrication, properties, and applications," *Chem. Rev.*, vol. 110, no. 10, pp. 5790–5844, 2010.

[154] W. Z. Li *et al.*, "Large-scale synthesis of aligned carbon nanotubes," *Science*, vol. 274, no. 5293, pp. 1701–1703, 1996.

[155] D. K. Schroder, *Semiconductor Material and Device Characterization*, 3rd ed. John Wiley & Sons, Inc., 1990.

[156] F.M. Smits, "Measurement of sheet resistivities with the four-point probe," *Bell Syst. Tech. J.*, vol. 37, pp. 711–718, 1958.

[157] M. Y. Li, M. Yang, E. Vargas, K. Neff, A. Vanli, and R. Liang, "Analysis of variance on thickness and electrical conductivity measurements of carbon nanotube thin films," *Meas. Sci. Technol.*, vol. 27, no. 9, 2016.

[158] C. Zamora-Ledezma *et al.*, "Conductivity anisotropy of assembled and oriented carbon nanotubes," *Phys. Rev. E - Stat. Nonlinear, Soft Matter Phys.*, vol. 84, no. 6, pp. 1–5, 2011.

[159] C. Li, E. T. Thostenson, and T. W. Chou, "Effect of nanotube waviness on the electrical conductivity of carbon nanotube-based composites," *Compos. Sci. Technol.*, vol. 68, no. 6, pp. 1445–1452, 2008.

[160] S. C. and C. J. S. Gerdes, T. Ondarcuhu, "Combing a carbon nanotube on a flat metal-insulator-metal nanojunction," *Europhys. Lett.*, vol. 48, no. 3, pp. 292–298, 1999.

[161] M. A. Rahman, H. Agha, T. K. Truong, J. H. Park, D. Suh, and G. Scalia, "Incorporation and orientational order of aligned carbon nanotube sheets on polymer films for liquid crystal-aligning transparent electrodes," *J. Mol. Liq.*, vol. 267, pp. 363–366, 2018.

[162] W. Gao and J. Kono, "Science and applications of wafer-scale crystalline carbon nanotube films prepared through controlled vacuum filtration," *R. Soc. open Sci.*, vol. 6, no. 3, p. 181605, Mar. 2019.

[163] C. Zamora-Ledezma, C. Blanc, M. Maugey, C. Zakri, P. Poulin, and E. Anglaret,

"Anisotropic thin films of single-wall carbon nanotubes from aligned lyotropic nematic suspensions," *Nano Lett.*, vol. 8, no. 12, pp. 4103–4107, 2008.

[164] D. L. White and G. N. Taylor, "New absorptive mode reflective liquid-crystal display device," *J. Appl. Phys.*, vol. 45, no. 11, pp. 4718–4723, 1974.

[165] M. A. Rahman, "Aligned multi-wall carbon nanotube sheets for liquid crystal displays," University of Luxembourg, 2019.

[166] L. Langer, V. Bayot, E. Grivei, and J. Issi, "Quantum transport in a multiwalled carbon nanotube," *Phys. Rev. Lett.*, vol. 76, pp. 479–482, 1996.

[167] C. Te Lin *et al.*, "Anisotropic electrical conduction of vertically-aligned single-walled carbon nanotube films," *Carbon*, vol. 49, no. 4, pp. 1446–1452, 2011.

[168] L. Sheng, W. Gao, X. Ma, X. Zhao, S. Cao, and J. Zhang, "Electrical properties in magnetic field of macroscopic carbon nanotube objects," *J. Nanosci. Nanotechnol.*, vol. 10, no. 6, pp. 4049–4053, 2010.

[169] P. G. Collins, K. Bradley, M. Ishigami, and A. Zettl, "Extreme Oxygen Sensitivity of Electronic Properties of Carbon Nanotubes," *Science*, vol. 287, no. 5459, pp. 1801–1805, 2000.

[170] S. Y. Jeon *et al.*, "Dynamic Response of Carbon Nanotubes Dispersed in Nematic Liquid Crystal," *Nano*, vol. 02, no. 01, pp. 41–49, 2007.

[171] A. E. Aliev *et al.*, "Thermal transport in MWCNT sheets and yarns," vol. 45, pp. 2880–2888, 2007.

[172] C. Schönenberger, A. Bachtold, C. Strunk, J. Salvetat, and L. Forró, "Interference and Interaction in multi-wall carbon nanotubes," *Appl. Phys. A*, vol. 69, pp. 283–295, 1999.

[173] A. Rochefort, D. R. Salahub, and P. Avouris, "The effect of structural distortions on the electronic structure of carbon nanotubes," *Chem. Phys. Lett.*, no. November, pp. 45–50, 1998.

[174] G. Scalia, M. Haluska, U. Dettlaff-Weglikowska, F. Giesselmann, and S. Roth, "Polarized

Raman spectroscopy study of SWCNT orientational order in an aligning liquid crystalline matrix," *AIP Conf. Proc.*, vol. 786, no. 1, pp. 114–117, 2005.

[175] N. Phanthuna and C. Jassadajin, "Shielding Effect and Guarding in High Resistance Measurement," *Appl. Mech. Mater.*, vol. 879, pp. 196–200, 2018.

[176] Keithley Instruments Inc., *Low Level Measurements Handbook- Precision DC current, voltage and resistance measurements.*, 6th ed. 2004.

[177] Y. Huang *et al.*, "A multilayered flexible piezoresistive sensor for wide-ranged pressure measurement based on CNTs/CB/SR composite," *J. Mater. Res.*, vol. 30, no. 2, pp. 1869–1875, 2015.

[178] V. Skákalová, A. B. Kaiser, Y. S. Woo, and S. Roth, "Electronic transport in carbon nanotubes: From individual nanotubes to thin and thick networks," *Phys. Rev. B - Condens. Matter Mater. Phys.*, vol. 74, no. 8, pp. 1–10, 2006.

[179] "Liquid Crystals: a simple view on a complex matter." http://www.personal.kent.edu/~bisenyuk/liquidcrystals/textures1.html.

[180] "Polarized light |Trondheim Science Center." https://www.vitensenteret.com/en/mod377e.

[181] "Polarized Light Microscopy: Nikon's MicroscopyU." https://www.microscopyu.com/techniques/polarized-light/polarized-light-microscopy.

[182] J. Prasek *et al.*, "Methods for carbon nanotubes synthesis - Review," *J. Mater. Chem.*, vol. 21, no. 40, pp. 15872–15884, 2011.

[183] A. J. G. Zarbin, "Química de (nano)materiais," *Quim. Nova*, vol. 30, pp. 1469–1479, 2007.

[184] T. J. Sisto, L. N. Zakharov, B. M. White, and R. Jasti, "Towards pi-extended cycloparaphenylenes as seeds for CNT growth: Investigating strain relieving ring-openings and rearrangements," *Chem. Sci.*, vol. 7, no. 6, pp. 3681–3688, 2016.

Acknowledgements

This thesis would not have been possible without the encouragement and support of some wonderful people around me. My deepest gratitude and appreciation go to all of them for being a part of this journey and helping me achieve my dream!

Foremost, I am extremely grateful to my supervisor, Dr. Giusy Scalia, for giving me this opportunity to be a doctoral researcher at the University of Luxembourg. I sincerely thank her for the valuable time, patience, and advice offered during my Ph.D. study. Her guidance and continued support was a valuable factor in staying productive during the COVID-19 lockdown and successfully completing this thesis within the timeline set prior to the COVID-19 crisis. I also would like to express my sincere gratitude to my thesis supervision committee (CET) members: Dr. Susanne Siebentritt, Dr. Tanja Schilling, and Dr. Emmanuel Defay for their insightful remarks and suggestions for the improvement of my research work. Susanne was always very supportive and offered many fruitful discussions, continuous encouragement, and constant motivation that immensely helped me to get back on track whenever I was derailed during this journey. Tanja, with her careful attention to detail, has often steered my thoughts to multiple perspectives that I would never have paid attention to otherwise. Emmanuel's comments always encouraged me to think beyond the academic boundaries and, thus, we were able to file a patent for one configuration of the pressure sensor that was developed. I once again thank Giusy for having picked the best supervisory committee I could have ever asked for. The mentorship I received from all four of them has been influential throughout this research. I would also like to thank Dr. Philippe Poulin, for accepting to be on the defence committee.

I would like to acknowledge the Luxembourg National Research Fund for financially supporting this research within the doctoral programme MASSENA, in the frame of PRIDE scheme of the *Fonds National de la Recherche* (FNR), MASSENA - Pride/15/ 10935404. Thanks also to the Doctoral Program in Physics and Materials Science (DPPM), University of Luxembourg for providing financial aid for some of the travel expenditures incurred during this project.

I owe my warmest gratitude to my good friend, Hakam Agha, without whom this thesis would hardly have been completed. I am forever grateful for the countless number of times he has been there for me, both professionally and personally, for providing guidance and being a sounding board whenever required. Hakam was always very helpful and spent a considerable amount of time assisting me at different stages of this research, including moulding my experimental techniques, critiquing the results, reviewing this thesis and improving my presentation skills. It is a pleasure to thank my friends Asiqur Rahman and Shameek Vats for being the best officemates and for the wonderful times we shared. I believe we had the perfect balance of a cordial workspace that was both productive and enthusiastic. Shameek, you were such a calming influence in the most stressful situations of my Ph.D. life. Thanks for being not only a wonderful colleague but a great friend as well. You will be cherished forever! A big thanks to my friend Larry Honaker for always being a saviour with his timely responses to all my queries and concerns about anything and everything, be they administrative issues or scientific doubts, and also for proofreading this thesis. My heartfelt gratitude to Anshul Sharma and her little family for making Luxembourg a home far away from home!

I gratefully acknowledge Prof. Jan Lagerwall for permitting access to his laboratory and some of the equipment. Many thanks also to Zornitza Tosheva for teaching me the basics of Scanning Electron Microscopy and to Rijeesh Kizhakidathazhath for his help with the different chemicals. I am also thankful to Astrid Tobias for taking care of all the administrative tasks including the purchase of equipment, registrations, and bookings for every conference. She has always been supportive, kind, and compassionate. In the absence of Astrid, Vanessa Schmidt, Adamantia Galani, and Patricia Ramoa were very helpful. My sincere thanks to them as well. I would also like to extend my heartfelt thanks to all the friendly faces at the University of Luxembourg, especially Camila Honorato, Manos Anyfantakis, Claudius Lehr, Christina Schütz, Anupam Sengupta, Sharif Shahini, Ulrich Siegel, and Robert Wagener, who have all made my stay in Luxembourg a pleasant experience.

I would also like to express my sincere gratitude to all my teachers at the International Indian School, Riyadh, and at the Amrita University, Kerala, who taught me the fundamentals of academic life and ignited the passion for science in me. I very much appreciate my dear friends, Shilpa, Rachel, Pradeep, Akhil, Sidhu, Aravind, Arjun, Radhika, and Lekshmi, for their never-ending emotional support.

Last but not least, my deepest and warmest appreciation to all my dear family members for their unflinching support and love. My special thanks to my husband, Praveen, who even despite being 600 miles away was my constant motivation and support especially during times when I felt I would never make it! I am also thankful to my in-laws, Valsala, Prakash and Priyanka, for their understanding and endless encouragement. I will be ever grateful to my late aunt, Renuka, for sparking in me an interest to pursue a Ph.D. in Physics and am sorry that she was not able to see me graduate. Many thanks to my aunt Krishna and uncle Rajesh for always having my back and encouraging me to follow my dreams. My heartfelt thanks go out to my mother, Usha, father, Murali, and sister, Neethu, for their unwavering support and belief in me. I am forever indebted to my parents for providing me the experiences and opportunities that moulded me into who I am today. If it was not for their persistent backing, this dream would not have been possible, and I dedicate this achievement to my beloved parents!

Luxembourg, December 2020 Meenu Murali

List of publications, presentations and other activities

Patent:

G. Scalia, *M. Murali*, and H. Agha, "Carbon nanotube pressure sensor", Luxembourg Patent Office, LU102155, filed on 21 October 2020.

Peer-Reviewed Journal Articles:

- *M. Murali*, H. Agha, A. Mrzel and G. Scalia, "Difference in the interaction of nano-diameter rod and tubular particles with a disclination line in a nematic liquid crystal", *RSC Advances* (2020), 10, 21473-21480.
- *M. Murali*, MD A. Rahman and G. Scalia, "Reorientation and flow of liquid crystal for a pressure sensor using carbon nanotube sheets", Manuscript submitted.
- *M. Murali*, MD A. Rahman and G. Scalia, "Investigation of electrical properties of aligned carbon nanotube sheets in liquid crystals", Manuscript in preparation.

Oral Presentations:

- *M. Murali*, H. Agha, and G. Scalia, "Vertical interconnects of networks of carbon nanotubes in liquid crystals", presented at the 46th German Liquid Crystal Conference, March 2019, Paderborn, Germany.
- Oral presentations at Massena cluster 1 (Strain sensors and Energy harvesters) meeting, January 2018, May 2019 and May 2020, University of Luxembourg.

Poster Presentations:

- Two poster presentations at the 2019 TechConnect World Innovation Conference & Expo, June 2019, Boston, U.S.A.
- Presented at the 33rd International Winter School on Electronic Properties of Novel Materials, March 2019, Tirol, Austria.
- Presented at the MASSENA Day, December 2018, Luxembourg.
- Presented at the 27th International Liquid Crystal Conference, July 2018, Kyoto, Japan.

- Presented at the 45th German Liquid Crystal Conference, March 2018, Luxembourg.

Teaching Activities:

- Liquid crystals and Colloids course (Masters, semester 1: Winter semester 2019-2020); TD
- Soft Matter Physics course (Bachelors, semester 6: Summer semester 2019-2020); attended classes and TD
- Liquid crystal course (Masters, semester 1: Winter semester 2018-2019); TD

Other Activities:

- Completed the Liquid crystal course (Masters, semester 1: Winter semester 2017-2018).
- Participated in the Bandol Summer School on Liquid crystals 2018, September 2018, Bandol.
- MASSENA seminar: Introduction to electronic structure calculations, January 2019.
- MASSENA seminar: Fabrication technologies and electrical response of sensors, May 2018.
- MASSENA seminar: Materials for sensing, April 2018.
- MASSENA seminar: Energy Harvesters, February 2018.
- Transferable skills: "Hands-on python for beginners", University of Luxembourg, February 2020.
- Transferable skills: "Intellectual Property Rights", Luxembourg Institute of Science and Technology, June 2019.
- Transferable skills: "Good Scientific Practice", University of Luxembourg, February 2019.
- Transferable skills: "PhD done. What next?", University of Luxembourg, December 2018.
- Participated in the workshop "Chemistry of Atomic Layer Deposition", Luxembourg Institute of Science and Technology, March 2018.
- Participated in the workshop "Project Management for Research", University of Luxembourg, September 2017.